Compound Helicopter Flight Dynamics Modelling

MSc Thesis

George Tzanetos Alevras

TUDelft

Compound Helicopter Flight Dynamics Modelling

MSc Thesis

by

George Tzanetos Alevras

Student Number   4667638

TUDelft

Preface

This thesis not only marks the end of my MSc Control Operations degree in the faculty of Aerospace Engineering, but a six years journey in TU Delft, since I started my BSc in the same faculty, in 2017. Coming here directly from high-school years in Athens, I developed a different way of thinking, and for this I am grateful

I also would really like to thank my supervisor Marilena Pavel, for our collaboration the past year. It is known that there is little knowledge offered in the faculty in the field of rotorcraft, and so my gaps when starting this thesis had been more than usual. However, it was her amazing work in the field and her guidance that steered me in the right direction. Furthermore, it is the same lack of helicopter-related courses that led me to feel the drive toward such a topic. So, as I have said in multiple meetings, I have enjoyed and cherished every aspect of this thesis.

I am thankful too for my family Kostas, Zizih, and Nico, for the unlimited support they have given me for 24 years, in the form of advice, caution, stories, and experiences. Lastly, I am paying tribute to the circle of friends I have developed here, who made these challenging degrees as enjoyable as they have been.

George Tzanetos Alevras
Delft, June 2023

Contents

List of Figures

List of Tables

Nomenclature

Abbreviations

Abbreviation	Definition
VTOL	Vertical Take-off and Landing
RPM	Revolutions Per Minute
AoA	Angle of attack
CP	Control Plane
DP	Disc Plane
NED	North-East-Down
EOM	Equation Of Motion
SA	Shaft Axis
SP	Shaft Plane
DoF	Degrees of Freedom
CA	Control Allocation (section 3)
CA	Control Axis (section 2)
CG	Centre of Gravity

Symbols

Symbol	Definition	Unit
T/HP	Power Loading	lbf/HP
T/A	Disc Loading	lbf/ft^2
ρ	Density	kg/m^3
X,Z	Force components in the X- and Z-axis	N
M	Moment component about the Y-axis	Nm
ϑ_0	Rotor collective pitch	deg
ϑ_{1s}	Rotor longitudinal cyclic pitch	deg
$\bar{\vartheta}_p$	Mean propeller pitch	deg
δ_e	Elevator deflection	deg
σ	Solidity ratio	-
a_0	Rotor coning angle	deg
a_1	Rotor longitudinal flapping angle	deg
b_1	Rotor lateral flapping angle	deg
ϑ_f	Body pitch angle	deg
ψ	Blade azimuth angle	deg
μ	Tip-speed ratio	-
λ	Non-dimensional induced velocity	-
D_{tot}	Total drag	N
D	Drag	N
L	Lift	N
T	Thrust	N
Ω	Rotational velocity	rad/s
A	Area	m^2
S	Surface area	m^2
A_{eq}	Equivalent area	m^2
$C_{T,L,D}$	Thrust, Lift, Drag coefficient	-

Symbol	Definition	Unit
$\mathbf{u}$	Control vector	-
$\mathbf{v}$	Virtual control vector	-
$\mathbf{u_p}$	Reference control vector	-
$\mathbf{W}$	Weight matrix	-
γ	Weighted Least Squares factor	-
α	Angle of attack	rad
α_{dp}	Angle of attack of disc plane	rad
α_{cp}	Angle of attack of control plane	rad
α_{sp}	Angle of attack of shaft plane	rad
Ψ	Blade azimuth position	rad
γ	Lock number $\frac{\rho C_{L_\alpha} c_e R^4}{I_\beta}$	-
μ_x	Advance ratio	-
λ	Permeability	-
u	X-axis velocity component	m/s
v	Y-axis velocity component	m/s
w	Z-axis velocity component	m/s
p	Body roll rate	rad/s
q	Body pitch rate	rad/s
r	Body yaw rate	rad/s
ε_0	Average downwash angle	rad
ε_0	Wing incidence angle	rad
ε_β	Flapping hinge offset ratio	-
φ	Euler rotation around x-axis	rad
ϑ	Euler rotation around y-axis	rad
ψ	Euler rotation around z-axis	rad
ϑ_0	Collective pitch	rad
ϑ_{1s}	Longitudinal cyclic pitch	rad
ϑ_{1c}	Lateral cyclic pitch	rad
ϑ_{0pp}	Port-side propeller pitch	rad
ϑ_{0ps}	Starboard-side propeller pitch	rad
δ_e	Elevator deflection	rad
δ_r	Rudder deflection	rad

Introduction

The compound helicopter, once overshadowed by more favorable configurations in the latter half of the 20th century, has recently experienced a resurgence of interest due to its potential to overcome contemporary challenges and offer previously unattainable possibilities. However, the maximum speed of compound helicopters is currently limited to around 150 knots, primarily constrained by the aerodynamic capabilities of the main rotor, engine power, and airframe drag. While careful design considerations can address the latter two limitations, the aerodynamic characteristics of the rotor pose significant challenges. The presence of retreating blade stall and advancing blade compressibility effects further exacerbates these obstacles. In 1960, R.B. Lightfoot conducted a seminal case study titled "The Helicopter as a Transport Vehicle," comparing various hypothetical aerial vehicles, including the compound helicopter, tilt-fan, lift-fan, and conventional helicopter [1]. The study focused on a 300-mile range and a 4-ton payload, demonstrating that the compound helicopter exhibited superior economic performance across both longer and shorter ranges. This finding highlighted the potential for increasing the speed of the compound helicopter while preserving its efficient hover capability, thereby making it suitable for a wide range of military and civil applications.

Lightfoot's study triggered a sequence of events, with flight testing of developed compound rotorcraft taking place within a few years. However, subsequent declining interest was revitalized by the recent surge in the vertical take-off and landing market. These developments and advancements in hybrid compound rotorcraft have culminated in newer generations of aircraft, exemplified by Airbus Helicopters' RACER, which is the successor to the X3 demonstrator [2]. Despite the advancements in compound rotorcraft, challenges in controllability have impeded further research in the 1980s and 1990s. To address this, novel methods of trim optimization and control allocation have emerged from meticulous calculations and an extensive review of existing literature. Hybrid compound helicopters represent a promising advancement in rotorcraft technology, offering improved performance, versatility, and efficiency by combining features of both rotary-wing and fixed-wing configurations. However, understanding the complex flight dynamics of these aircraft and developing effective control systems present significant challenges. This research addresses these challenges by presenting a comprehensive modeling approach for the flight dynamics of a hybrid compound helicopter using classical mechanics methods.

The research focuses on developing a non-linear mathematical model that encompasses the various components of the aircraft, including the rotor, propellers, wings, fuselage, and empennage. By integrating these components into a unified dynamics framework, a set of Equations of Motion is derived, providing a precise representation of the hybrid compound helicopter's behavior. A notable feature of the model is the incorporation of conventional first-order steady flapping motion and quasi-dynamic inflow modeling for the rotor and propellers, allowing for realistic modeling of their aerodynamic interactions. The resulting mathematical model represents a complete 9 Degree-of-Freedom system, augmented with additional mechanical and inflow degrees of freedom. As an over-actuated coupled system, it offers multiple control inputs, including rotor collective pitch, rotor longitudinal and lateral cyclic pitch, port-side and starboard-side propeller pitch, elevator deflection, and rudder deflection. These controls enable precise manipulation of the hybrid compound helicopter's flight parameters and facilitate the attainment of trim conditions during forward flight.

The primary objective of this study is to identify operating trim points across the hybrid compound helicopter's forward flight envelope. Numerical optimization techniques are employed to achieve optimal control allocation, with a particular focus on prioritizing the auxiliary propulsion system. A mapping function is utilized in the control allocation process to identify trim points that ensure stability, maneuverability, and efficient performance across various airspeeds, ranging from hover to the observed maximum airspeed of 255 knots. The research findings demonstrate the successful implementation of a slowed-rotor strategy at high speeds, effectively mitigating the adverse effects of compressibility and ensuring safe and stable flight. Additionally, a linearized mathematical model is derived from the

comprehensive non-linear model, providing crucial insights for future stability analysis and control system design. These outcomes contribute valuable knowledge to the advancement of hybrid compound helicopter technology, facilitating the development of more efficient and reliable aircraft in the field of rotorcraft engineering. In the subsequent sections, we will delve into the methodology, mathematical modeling process, optimization techniques, and the obtained results in detail. This research significantly contributes to the understanding and advancement of hybrid compound helicopter technology, offering valuable insights for future studies, stability analysis, and control system design in this exciting and innovative aircraft configuration.

Research Paper

Flight Dynamics Modelling and Trim Optimization for a Hybrid Compound Helicopter in Forward Flight

G. Tzanetos Alevras

MSc student
TU Delft Aerospace Engineering
g.tzanetosalevras@student.tudelft.nl

Abstract

This research presents a comprehensive modeling approach for the flight dynamics of a hybrid compound helicopter, employing classical mechanics methods. The derived non-linear mathematical model encompasses the individual components of the aircraft, including the rotor, propellers, wings, fuselage, and empennage. These components are integrated into a unified dynamics framework through the final Equations of Motion. Notably, the model incorporates a conventional first-order flapping motion and quasi-dynamic inflow modeling for both the rotor and propellers. The resulting model represents a complete 9 Degree-of-Freedom system, augmented with 6 mechanical ones and an additional 3 for the inflows of the rotor and the two propellers. As an over-actuated coupled system, it offers 7 available controls; rotor collective pitch, rotor longitudinal and lateral cyclic pitch, port-side and starboard-side propeller pitch, elevator deflection, and rudder deflection. The primary objective of this study is to identify operating trim points during forward flight, ranging from hover to the recorded maximum airspeed of 255 knots. Achieving trim through numerical optimization involves a control allocation process utilizing a mapping function that prioritizes the auxiliary propulsion. The research findings demonstrate the successful implementation of a slowed-rotor strategy at high speeds, effectively mitigating compressibility effects. Additionally, a linearized mathematical system is derived, providing essential insights for future stability analysis and control system design. These outcomes contribute valuable information toward the advancement of hybrid compound helicopter technology.

Nomenclature

Symbols

α	Angle of attack [rad]
α_{cp}	Angle of attack of control plane [rad]
α_{dp}	Angle of attack of disc plane [rad]
α_{sp}	Angle of attack of shaft plane [rad]
δ_e	Elevator deflection [rad]
δ_r	Rudder deflection [rad]
ε_0	Average downwash angle [rad]
ε_0	Wing incidence angle [rad]
ε_β	Flapping hinge offset ratio [-]
γ	Lock number $\frac{\rho C_{L_\alpha} c_e R^4}{I_\beta}$
λ	Permeability [-]
μ_x	Advance ratio [-]
φ	Euler rotation around x-axis [rad]
Ψ	Blade azimuth position [rad]
ψ	Euler rotation around z-axis [rad]
ϑ	Euler rotation around y-axis [rad]
ϑ_0	Collective pitch [rad]
ϑ_{0pp}	Port-side propeller pitch [rad]
ϑ_{0ps}	Starboard-side propeller pitch [rad]
ϑ_{1c}	Lateral cyclic pitch [rad]
ϑ_{1s}	Longitudinal cyclic pitch [rad]
p	Body roll rate [rad/s]
q	Body pitch rate [rad/s]
r	Body yaw rate [rad/s]
u	X-axis velocity component [m/s]
v	Y-axis velocity component [m/s]
w	Z-axis velocity component [m/s]

Subscripts

mp	Moore-Penrose pseudo-inverse

p	Propellers
pp	Port-side propeller
ps	Starboard-side propeller
t	Horizontal tail
v	Vertical tail
w	Wings

Superscripts

b	Body-fixed reference frame
BEM	Blade Element Method
Gl	Glauert theory
n	NED reference frame

Abbreviations

AoA	Angle of attack
CA	Control axis
CG	Centre of gravity
CP	Control plane
DA	Disc axis
DP	Disc plane
EOM	Equation of Motion
NED	North-East-Down
RPM	Revolutions per minute
SA	Shaft axis
SP	Shaft plane
VTOL	Vertical Take-Off and Landing

1   Introduction

The compound helicopter is a special case of innovation that was set aside in the second half of the 20th century in light of more desirable configurations at the time and has been most recently been looked at again, after evaluation that some of its key features, might be able to overcome some modern hurdles that its predecessors could not. The maximum speed of them is limited by the aerodynamic capabilities of the main rotor, installed engine power, and airframe drag. While the two last ones can be resolved through careful design, the limitations of the rotor aerodynamic characteristics cannot. The restrictions of retreating blade stall and advancing blade compressibility effects are undoubtedly hindering. In 1960 R.B. Lightfoot created a case study in which new hypothetical aerial vehicles were compared in "The Helicopter as a Transport Vehicle"[1]. The compound helicopter was featured next to a tilt-fan, a

lift-fan, and a conventional helicopter. The study was based on a 300-mile range and a 4 ton payload but the charts show the helicopter and the compound are distinctly more economical at both longer and shorter ranges. Therefore, an increase in speed, provided that efficient hover capability is maintained, would make the compound helicopter suitable for various roles and missions in both military and civil markets.

What followed Lighfoot's study was followed by a chain of events in a short timespan with developed compound rotorcraft being flight-tested within the next few years. After a decline in interest, it has been again risen with the simultaneous rise of the VTOL market. More recently, there have been alterations based on the performance of the above, which has led to newer generations of aircraft of this identity. Specifically here, an attractive version of hybrid compound rotorcraft configurations was seen, with the X3 demonstrator, the predecessor of one of the newest designs of Airbus Helicopters, the RACER. Although vehicles like this showed clear improvements in certain areas, they pose challenges in controllability, which was partly the reason of the drop in related research in the 80s and 90s. Like many recent studies, this research faces this with trim optimization and control allocation, obtained from thorough calculations and literature study. In this paper, a concise path of the modelling process is given, which will then lead to a non-linear mathematical model in need of trim. Consequently, the trim problem will be addressed and solved in forward flight. Lastly, a linearized system will be created and tested in open loop, to supply further research with as defined a tool needed, for the achievement of the ultimate goal, which will be the fully functional simulation of maneuvering flight.

2   Flight Mechanics Modelling

In rotorcraft simulation, the dynamics to be under manipulation are high-order, highly-coupled and non-linear, not to mention severely unstable in uncontrolled flight. Their modeling is a crucial matter to be taken seriously, and that their modeling methods are consistent. For this research, the 9-DoF over-actuated system entails 3 inflow degrees of freedom on top of the 3 translational and the 3 rotational ones, it is required to tend to the vehicle's mechanics, and the effects of states and inputs on them, with clear steps and reference systems definition. Although literature has shown a multitude of computational methods, that lead to high-level modeling, for the purpose of test data validation, this paper approaches the problem with derived methods of classical mechanics explained later on. In the end of the section, a set of Equations of Motion are derived, representing a system of non-linear unified dynamics, to be trimmed subsequently. A set of assumptions is essential at this point, that help put the model fidelity in perspective;

- Flapping dynamics are assumed first-order, and thus steady-state disc-tilt angles are shown only. Higher order dynamics are neglected, as well as fast transient blade flapping modes. Lag dynamics are also assumed to supersede the research scope.

- The airflow is assumed incompressible, and with no reverse flow regions in the rotor disc. As said before, this assumption will be challenged later on, and certain modifications will be suggested to achieve the research objectives.

- Engine dynamics are chosen to be obtained as non-existent, and with having a constant rotor and propellers angular velocity, the differential equations that describe their rotation speed, are not considered.

- Atmospheric conditions are deemed constant, and at sea level. This is a valid assumption for forward flight simulation, but when climbing and maneuvering flight is considered, an atmospheric model should be in place, to provide the appropriate external conditions.

Figure 1: Eurocopter X3 (obtained from ainonline.com)

This research follows in part the blade element method as in (Pavel, 2001) and (Pavel, 1996), and attempts to mathematically describe a complete 6-DoF compound helicopter model, with additional inflow DoFs. The components modeled separately, to result in the overall dynamics description, are the rotor, the empennage consisting of horizontal and vertical tails, the propellers, the wing and the fuselage. Figures 14, 15 and 16 display the initial Free-Body diagram analysis of the aerodynamic forces and moments these components cause. Note that, outside the rotor and propeller forces, the aerodynamic forces are shown in the velocity reference frame. In this section, the work towards the finalized model is presented, with the subsections focusing on each component individually, and a final subsection with the entire body dynamics.

2.1 Rotor

This model features a five-blade equivalent flapping hinge rotor modelled using the Blade Element Method, where the discretization of the blade in two-dimensional airfoil sections and the calculation of local aerodynamics and inertial forces, are then integrated over the length of the blade for the total forces and torques. Note that it is only a valid method for high-aspect ratio blades, like in this study. The rotor blades were modeled as undergoing rigid-body flap rotations and the equilibrium is calculated about an offset flap hinge. Furthermore, the blade is twisted at an angle ϑ_{tw}, which is considered in the thrust calculation but not in the flapping motion itself. A total of three control inputs influence the orientation of he rotor and its dynamic

output, namely the collective pitch ϑ_0, longitudinal cyclic ϑ_{1s}, and lateral cyclic pitch ϑ_{1c}. No lagging dynamics have been made of interest in this research and overall, the model is derived primarily using the work of Pavel (1996) and Bramwell (2001). The following subsections outline the modelling of the flapping and inflow dynamics, the derivation of the forces and moments, and their expression transitioning between rotor reference frames.

2.1.1 Flapping dynamics

In the absence of lead-lag dynamics, and under the rigid blade assumption, the flapping dynamics in steady-state modes are modelled here up to and including the first harmonics of the Fourier series of the periodic motion $\beta(\Psi)$;

$$\beta(\Psi) = a_0 - a_1 \cos \Psi - b_1 \sin \Psi \tag{1}$$

where a_0 is the coning angle, a_1 is the longitudinal disc-tilt angle, and b_1 is the lateral disc-tilt angle. Truncation of the Fourier series sources from the fact that free motion of the blades like fast eigenmodes is not of interest but only the effect on the airframe, and that the response to control inputs is instantaneous leading to asymptotic approximation of the flapping behaviour. As proposed by Bramwell the coefficients of Equation 1 are expressed as follows [2];

$$a_0 = \frac{\gamma}{8} \left[\vartheta_0(1 + \mu_x^2) + \frac{4\lambda}{3} + \frac{2}{3}\mu_x\bar{p} \right] \tag{2}$$

$$a_1 = \frac{\frac{8}{3}\mu_x\vartheta_0 + 2\mu_x\lambda + \bar{p} - \frac{16}{\gamma}\bar{q}}{1 - \frac{1}{2}\mu_x^2} \tag{3}$$

$$b_1 = \frac{\frac{4}{3}\mu_x a_0 + \bar{q} - \frac{16}{\gamma}\bar{p}}{1 + \frac{1}{2}\mu_x^2} \tag{4}$$

where $\bar{q} = q/\Omega$ and $\bar{p} = p/\Omega$ are the non-dimensional pitch and roll rate respectively. It is important to list assumptions made for these simplified versions for the level of modelling fidelity of this research. For them, the flapping hinge offset is neglected ($\varepsilon = 0$), and only a first-order relationship with rates p and q is considered. Also, induced velocity is assumed uniform along the rotor disc here. To compensate for that, the model follows Pavel (2001) in the usual inclusion of a correction factor, expressed as in Equation 5;

$$K_{corr} = \frac{1.33\mu_x/|\lambda|}{1.2 + \mu_x/|\lambda|} \tag{5}$$

in order to obtain the new lateral disc tilt angle of Equation 6 [3].

$$b_1 = \frac{4\mu_x a_0/3 + \bar{q} - \frac{16}{\gamma}\bar{p}}{1 + \mu_x^2/2} + \frac{K\lambda_0}{1 + \mu_x^2/2} \tag{6}$$

As mentioned, the above takes place in the control plane, so it will be shown shortly, how these help the transition to the disc plane, and how they end up affecting the total movement of the body.

2.1.2 Inflow model

Vital in rotorcraft dynamics is the modelling of the rotor inflow. A plethora of research is present in the matter and its understanding is essential for simulation fidelity. Among the existing approaches for induced velocity, this research focuses on a quasi-dynamic inflow modelling, treating the variable as an additional state in the model, which dynamically varies by equating the thrust coefficient obtained from the Blade Elementh Method, and that resulting from Glauert's theory. In the longitudinal model during the preliminary phase of this research, and in the early stages of the complete 6-DoF modelling of this vehicle, a uniform inflow method was implemented. However the assumption of uniform inflow in forward and maneuvering flight, leads to misinterpretation of the induced velocity in the aft of the rotor disc, bringing the issue of overestimated blade lift in that region. Therefore, this more advanced model was adopted for application to piloted simulation or control related research.

$$C_T^{Gl} = 2\lambda_0 \sqrt{\left(\mu \cos \alpha_{dp}\right)^2 + \left(\mu \sin \alpha_{dp} + \lambda_0\right)^2} \tag{7}$$

Regarding the Blade Element method, it will be used later in this section to derive the overall forces. Although, its drawback is that it assumes uniform velocity over the rotor disc, which at high speeds proves valid, but but at low speeds, measurement error diverges as inflow velocity approaches the other velocity vector components acting on the blade. Using the momentum theory, Glauert analyzed the rotor as an actuator disc, of zero thickness, which assumes a steady loading, but variable across the circular surface [4]. This ideal approximation, is equivalent to an infinite-blade rotor, though gives a decent first estimate of the wake-induced flow. Using non-dimensional values μ and λ_0, for the airspeed and the induced velocity at the rotor disc respectively, the thrust coefficient according to Glauert's theory is given by Equation 7. Equating it with the one from the Blade Element Method, and dividing by the time-constant τ_{λ_0}, provides the rate of change of inflow as shown below.

$$\dot{\lambda}_0 = \frac{1}{\tau_{\lambda_0}}(C_T^{BEM} - C_T^{Gl}) \tag{8}$$

In the end, the idea is that the inflow becomes dynamic, and that in steady-state condition, $\dot{\lambda}_0 \to 0$, which in turn means that, as such, the variable inflow takes place in the state vector, and in trim the zero-valued derivative is targeted like all other states. Simplicio et al. (2013) follows the same strategy in modelling, and uses a time-constant value of 0.1, as seen in Appendix A.4.

2.1.3 Forces & Moments

It is now the point to collect the aforementioned approaches in order to express the subsequent effect of the rotor on the entire body. Likewise with the flapping angles, the pitch dynamics follow a Fourier series representative motion in steady-state operation. Once again, the factors that concern the modelling, are the mean, also known as the collective cyclic, the twist factor, and the first harmonics;

$$\vartheta(\Psi) = \vartheta_0 + \vartheta_{tw}\bar{r} - \vartheta_{1c} \cos \Psi - \vartheta_{1s} \sin \Psi \tag{9}$$

where $\bar{r} = r/R_r$ is the radial position of the blade element section along the complete rotor radius. Using this above, and looking back at Figures **??** and **??**, one can move on to utilize the two cyclic pitch angles of the first harmonics and express the flapping angles about the SP as $a_{1R} = a_1 - \vartheta_{1s}$ and $b_{1R} = b_1 + theta_{1c}$. The transformation then from the DP directly to the body-fixed axis is finalized after considering γ_s too, to get $\mathcal{T}_{dp}^b$ as seen from Appendix A.3. Thus, for airspeed influence to the aerodynamic forces & moments, the AoA with respect to the SP as $\alpha_{SP} = \gamma_s + \alpha_{fus}$, where $\alpha_{fus} = \alpha$. The ones with respect to the CP and DP are respectively defined as $\alpha_{CP} = \alpha_{SP} + \vartheta_{1s}$ and $\alpha_{DP} = \alpha_{CP} + a_1$. Recalling the Blade Element theory, the velocity of an elementary blade section is assumed to experience a tangential component u_T and a radial component u_R, based only on forward speed and rotor rotation.

$$\vec{F}_{r_{cp}} = \begin{bmatrix} -H_{cp} & S_{cp} & -T_{cp} \end{bmatrix}^T \tag{10}$$

After aerodynamic derivation of the lift and drag on the airfoil, and double integration over both the radius and full revolution, force coefficients C_T, C_H and C_S are obtained, corresponding to the z-, x-, and y-axis. Additionally a torque coefficient C_Q around the z-axis is derived only, as the other two are neglected as insignificant. Note that these are expressed in the CP, and in dimensional form the forces affect the body-axes as displayed in Equation 10. Using the assumption that $C_T \gg C_H, C_S$ and the small angle approximation, the transition to the disc plane yields the following.

$$\begin{aligned} C_{T_{dp}} &\approx C_T, & C_{H_{dp}} &\approx C_H - C_T a_1 \\ C_{Q_{dp}} &\approx C_Q, & C_{S_{dp}} &\approx C_S - C_T b_1 \end{aligned} \tag{11}$$

The final coefficients, as derived in Pavel's doctoral thesis in 2001 are obtained to be as indicated below;

$$C_{T_{dp}} = \frac{\sigma C_{L_\alpha}}{2}\left[\left(\frac{1}{3} + \frac{\mu_x^2}{2}\right)\vartheta_0 + \frac{1 + \mu_x^2}{8}\vartheta_{tw} + \frac{\mu_x \bar{p}}{4} + \frac{\lambda}{2}\right] \tag{12}$$

$$C_{H_{dp}} = \sigma C_D \frac{\mu_x}{4} + \frac{\sigma C_{L_\alpha}}{4}\left[\left(a_1 \frac{\mu_x^2}{2} + \mu_x \lambda\right)\vartheta_0 + \frac{\mu_x \lambda}{2}\vartheta_{tw} + \bar{q}\left(\frac{b_1 \mu_x}{4} - \frac{a_0}{3}\right) - \frac{a_0 b_1}{3} + \left(a_0^2 + a_1^2\right)\frac{\mu_x}{2} + \frac{\bar{p}\lambda}{2}\right] \tag{13}$$

$$C_{S_{dp}} = \frac{\sigma C_{L_\alpha}}{4}\left[-\frac{1}{2}\mu_x a_0 \vartheta_0 + \left(-a_0 \frac{\mu_x}{3} + b_1 \frac{\mu_x^2}{4} - \frac{\bar{q}}{4}\right)\vartheta_{tw} - 3a_0\mu_x\left(\mu_x a_1 - \lambda\right) + b_1 \frac{\mu_x a_1 - \lambda}{2} + a_0 a_1 \frac{\mu_x^2 + 1}{3}\right] \tag{14}$$

$$C_{Q_{dp}} = \sigma \left[\frac{C_D}{8} \left(1 + 4.7\mu_x^2 \right) - C_{T_{dp}} \lambda_{dp} - C_{H_{dp}} \mu_x \right] \tag{15}$$

Regarding the moments of the subsystem, next to the Q-torque, there exist two more contributions considered in this model, which are the pitch and roll moments due to flapping eccentricity, namely M_e, and L_e defined by Equations 16 and 17 [5].

$$M_e = \rho \left(\pi R^2 \right) (\Omega R)^2 R \sin \left(a_1 + \vartheta_{1s} \right) C_{me} \tag{16}$$

$$L_e = \rho \left(\pi R^2 \right) (\Omega R)^2 R \sin \left(b_1 + \vartheta_{1c} \right) C_{me} \tag{17}$$

where the moment coefficient C_{me} is given to be;

$$C_{me} = \frac{\varepsilon_\beta m_{bl}}{\rho \left(\pi R^2 \right) R} \tag{18}$$

Finally, one is left with a highly representative model version of a hingeless rotor. Conventionally, rotorcraft are primarily powered by this source, and are not compounded by wings or auxiliary propulsion, meaning a decent time needs to be spent around the considerations in the flapping, lagging, pitching motion, and in the induced velocity dynamics of the subsystem. Transformations between reference frames also needs to be done with care, and assumptions like the small angle approximation have to be made consistently throughout, otherwise, modeling errors diverge very quickly. Here, one final transformation is made, to the body axes, after having brought all force expressions to the disc plane. The overall moments that affect the airframe take three forms. One is the force induced moments, seen in Equation 19 after cross product. The second form is the ones of flapping eccentricity aroung the hinge, from Equations 16 and 17, and the third is the torque produced by the rotor, and presented with the three forces. Note that s_{off} is a perpendicular offset distance from the body's longitudinal symmetry axis.

$$\begin{cases} \vec{\mathbf{F}}_\mathbf{r} = \mathcal{T}_{dp}^b \cdot \begin{bmatrix} -H_{dp} & S_{dp} & -T_{dp} \end{bmatrix}^T \\ \vec{\mathbf{M}}_\mathbf{r} = \begin{bmatrix} L_e & M_e & Q_{dp} \end{bmatrix}^T + \begin{bmatrix} d_r & s_{off} & -h_r \end{bmatrix}^T \times \vec{\mathbf{F}}_\mathbf{r} \end{cases} \tag{19}$$

2.2   Propellers

The propeller model follows the BEM calculation path like the rotor. In this vehicle, the pair of wing-mounted propellers is not just responsible for forward thrust, like in most aircraft, but also yaw control in the absence of the conventional tail rotor, a result achieved with differential thrust. As mentioned in the assumptions of this section, the engine dynamics are not modelled. Should that have been the case, a time-delay consideration between command and output would have been applicable here. Like with the rotor, the rotational velocity of the propellers is constant, and their thrust is manipulated solely through pitch command. It must be noted here, that they are modelled such that their line of thrust does not coincide, but is parallel to the

x_b-axis. As a result, the thrust sum contributes directly to the x-component of the total force. For overall modelling integrity, the inflow ratio for the propellers is also modelled under the quasi-dynamic inflow method of the rotor. The pair of the last two entries of the state vector is given by Equations 20 and 21.

$$\dot{\lambda}_{0pp} = \frac{1}{\tau_{\lambda_{0p}}} (C_{Tpp}^{BEM} - C_{Tpp}^{Gl}) \tag{20}$$

$$\dot{\lambda}_{0ps} = \frac{1}{\tau_{\lambda_{0p}}} (C_{Tps}^{BEM} - C_{Tps}^{Gl}) \tag{21}$$

In a configuration like the one under focus here, it is important to realise that all components operate inside the rotor's wake region. This is also true for the empennage, but for high speeds only. The effect of this observation, is an unconventional airflow near these components, and thus a strong rotr-component aerodynamic interaction. In this research, and for the level of fidelity targeted here, this is addressed in the form of interference factors. It will also be specified in the subsequent chapters but for the propellers specifically, it takes place in the equation of their advance ratio. Looking at Equation 22, one can notice this the $K_p \Omega R \lambda_0$ factor, which negatively affects the vertical component of the velocity experienced tangentially at the propeller disc. Also, the permeability of each propeller is given by Equations 23 and 24.

$$\mu_{x_p} = \frac{\sqrt{v^2 - \left(w + K_p \Omega R \lambda_0 - qd_p \right)^2}}{\Omega_p R_p} \tag{22}$$

To further represent the adjusted airflow, both advance ratio and permeability in each propeller are affected by induced local velocities cause by attitude rates. Factors qd_p, qh_p, rs_{pp} and rs_{ps} are exactly for this, and in each instance, it is shown that a positive corresponding rate will affect the flow either positively or negatively.

$$\lambda_{pp} = \frac{u - qh_p + rs_{pp}}{\Omega_p R_p} - \lambda_{0pp} \tag{23}$$

$$\lambda_{ps} = \frac{u - qh_p - rs_{ps}}{\Omega_p R_p} - \lambda_{0ps} \tag{24}$$

Notice the opposite signs in front of the yaw rate factor in the last two equations. It is intuitive to picture the vehicle performing a non-zero yaw rate turn, and that this will cause enhanced inflow at the port side propeller, and a negative one at the starboard side propeller. This detail, together with the variable pitch inputs, are the reason the two propellers end up having the desirable differential thrust. Lastly, the induced by the forces are added with a torque cause around the y-axis, of the form, $Q_p = \rho \pi R_p^2 (\Omega_p R_p)^2 R_p C_{Q_p}$, the coefficient of which is approximated from literature. Overall, forces and moments regarding the auxiliary propellers are expressed in the body frame, and are summarized by Equation 25.

$$
\begin{cases}
\vec{\mathbf{F}}_{\mathbf{p}} = \begin{bmatrix} T_{pp} + T_{ps} & 0 & 0 \end{bmatrix}^T = \vec{\mathbf{F}}_{\mathbf{pp}} + \vec{\mathbf{F}}_{\mathbf{ps}} \\[2mm]
\vec{\mathbf{M}}_{\mathbf{p}} = \begin{bmatrix} 0 & Q_p & 0 \end{bmatrix}^T + \vec{r}_{\mathbf{pp}} \times \vec{\mathbf{F}}_{\mathbf{pp}} + \vec{r}_{\mathbf{ps}} \times \vec{\mathbf{F}}_{\mathbf{ps}}
\end{cases}
\tag{25}
$$

where the last two factor are appear split because of the CG offset, and means that the moment induced around the z-axis comes after multiplying with slightly different arms $s_{pp} = s_p - s_{off}$ and $s_{ps} = s_p + s_{off}$. The sum of the two cross products in vector form equals $\begin{bmatrix} 0 & -(T_{pp} + T_{ps})h_p & T_{pp}s_{pp} - T_{ps}s_{ps} \end{bmatrix}^T$.

2.3 Wings

As mentioned, in addition to thrust compounding, this compound helicopter configurations features lift compounding by including wings in the design. These are a set of short-span wings in high positioning and at an anhedral angle. Contrary to the real Eurocopter X^3, the model does not include aileron surfaces. Therefore, their representation in the mathematical modelling is through their aerodynamic forces and induced moment about the pitch axis. Equation 26 outlines the lift force as follows;

$$
L_w = \frac{1}{2}\rho V_w^2 S_w C_{L_w} \cos(\Gamma)
\tag{26}
$$

where Γ is the anhedral angle and the angle of attack experienced at the wing position is affected by the induced velocity factor qd_w caused in a pitch rate motion.

$$
\alpha_w = \arctan\left(\frac{w + qd_w}{u}\right) + i_w - K_w\varepsilon_0
\tag{27}
$$

As with most components in the model, for improved fidelity, the aerodynamic interaction effect between the rotor and the wing is included using an interference factor K_w that alters the total angle of attack. Lastly, the design uses a conventional lift curve slope where $C_{L_w} = C_{L_{\alpha,w}}\alpha_w + C_{L_{\alpha=0}}$. Additionally, the drag coefficient of the wing follows a parabolic drag polar equation, as expressed in Equation 28, where AR is the aspect ratio of the wing and e is the Oswald efficiency factor.

$$
C_{D_w} = C_{D_0} + \frac{C_{L_w}^2}{\pi \cdot AR \cdot e_0}
\tag{28}
$$

The forces and moments expressed in the body axis of the system can be grouped as shown below.

$$
\begin{cases}
\vec{\mathbf{F}}_{\mathbf{w}} = \begin{bmatrix} -D_w & 0 & -L_w \end{bmatrix}^T \\[2mm]
\vec{\mathbf{M}}_{\mathbf{w}} = \vec{r}_{\mathbf{w}} \times \vec{\mathbf{F}}_{\mathbf{w}} = \begin{bmatrix} 0 & h_w D_w + d_w L_w & 0 \end{bmatrix}^T
\end{cases}
\tag{29}
$$

2.4 Fuselage

The fuselage of the vehicle is represented in this model by its parasite drag force R_{fus}, defined by Equation 30, and its aerodynamic moment contributions $C_{M_{fus}}$ and $C_{N_{fus}}$, around the y-

and z-axis respectively. The drag of the body is approximated by its equivalent flat-plate area F_0.

$$
R_{fus} = \frac{1}{2}\rho V^2 F_0
\tag{30}
$$

Furthermore, due to the geometry of the fuselage, there exist induced aerodynamic moments around the pitch and yaw axes, the coefficients of which are shown in Equations 31 and 32 respectively. The fuselage is assumed symmetrical around the roll axis, thus no moment coefficient $C_{L_{fus}}$ is considered. It is necessary to take into account the effect of the aerodynamic interaction between the rotor and fuselage, which will impact the resulting angle of attack and sideslip angle, and which are represented by interference factor K_f. In (Pavel, 1996), citing (Marinescu & Anghel 1992), a value of 0.83 is suggested for the first one [6] [7].

$$
C_{M_{fus}} = \left(\frac{V}{\Omega R}\right)^2 \frac{1}{AR} K_f V_{f_M} \alpha_f
\tag{31}
$$

$$
C_{N_{fus}} = \left(\frac{V}{\Omega R}\right)^2 \frac{1}{AR} K_f V_{f_N} \beta_f
\tag{32}
$$

V_{f_M} and V_{f_N} represent the volume of a body observed from their respective view, but having circular sections. Considerable to mention, is the assumption of the direct relationship between $C_{M,fus}$ and α_f. The angle of attack at which $M_{fus} = 0$ and the average downwash angle, are both considered to be zero, and would both be subtracted from α_f otherwise, to result in an effective AoA $\alpha_{eff} \neq \alpha_f$. The above are gathered in the body frame as expressed in Equation 33. R_{fus} was previously defined as such in the velocity frame, and so the vector is transformed using $\mathcal{T}_i^v$ from Appendix A.3.

$$
\begin{cases}
\vec{\mathbf{F}}_{\mathbf{fus}} = \mathcal{T}_i^v \cdot \begin{bmatrix} -R_{fus} & 0 & 0 \end{bmatrix}^T \\[2mm]
\vec{\mathbf{M}}_{\mathbf{fus}} = \begin{bmatrix} 0 & M_{fus} & N_{fus} \end{bmatrix}^T
\end{cases}
\tag{33}
$$

2.5 Empennage

The empennage of this vehicle is an H-tail configuration featuring a central horizontal tail and one vertical fin on each side of it. The horizontal tail incorporates an elevator surface, the deflection of which assists primarily in pitch moment control. The the vertical tails entail a rudder surface each, that control yaw movement upon deflection. Initially, the velocity at which the airflow meets the horizontal and vertical tail are visible in Equation 34 and Equation 35 respectively.

$$
V_t = \sqrt{u^2 + (w + ql_t)^2}
\tag{34}
$$

$$
V_v = \sqrt{u^2 + (v + ph_v - rd_v)^2}
\tag{35}
$$

As seen, both airspeeds above are affected by the vehicle's attitude rates, via the induced velocity factors ql_{ht}, ph_{vt} and rl_{vt}. More specifically, a positive pitch rate increases the horizontal tail airspeed, and a positive roll rate does the same to the

vertical tails, while a positive yaw rate negatively affects the latter. These affect the angle of attack and sideslip angle in an identical manner as they do V_t and V_v. The resulting force definitions of the empennage elements are expressed below.

$$L_t = \frac{1}{2}\rho V_t^2 S_t C_{L_{\alpha,t}}\alpha_t \tag{36}$$

$$Y_v = \frac{1}{2}\rho V_v^2 S_v C_{Y_{\beta,v}}\beta_v \tag{37}$$

The effect of the control surfaces are embedded in the coefficients $C_{L_{\alpha,t}}$ and $C_{Y_{\beta,v}}$ by way of vertical translation of the slope curves. That is, a positive elevator deflection δ_e raises the L_t/α_t slope by a factor of $dC_{L_{\alpha,t}}/d\delta_e$. In the same manner a positive rudder deflection δ_r raises the Y_v/β_v slope by $dC_{Y_{\beta,v}}/d\delta_r$. The contribution of the tail in the body dynamics is primarily through the negative pitch moment created by the positive lift. The lift force itself has little effect. A drag force is also present for model integrity, but negligible both in terms of force and moment contribution. Overall, the resulting vectors for the empennage are gathered. Equation 38 outlines those for the horizontal tail, and Equation 39 those for the vertical tails.

$$\begin{cases} \vec{F_t} = \begin{bmatrix} -D_t & 0 & -L_t \end{bmatrix}^T \\ \vec{M_t} = \vec{r_t} \times \vec{F_t} = \begin{bmatrix} 0 & h_tD_t - d_tL_t & 0 \end{bmatrix}^T \end{cases} \tag{38}$$

$$\begin{cases} \vec{F_v} = \begin{bmatrix} 0 & -Y_v & 0 \end{bmatrix}^T \\ \vec{M_v} = \vec{r_v} \times \vec{F_v} = \begin{bmatrix} h_vY_v & 0 & -d_vY_v \end{bmatrix}^T \end{cases} \tag{39}$$

2.6 Body dynamics

This section unifies the total dynamics of the modelled vehicle, analyzed over this section. Equation 40 gathers all forces an moments in two corresponding vectors, both acting on the center O^b of the body-fixed reference frame $O^bx^by^bz^b$. Note that due to offset distance s_{off} of the CG, these two do not coincide.

$$\begin{cases} \vec{F_{tot}} = \vec{F_R} + \vec{F_p} + \vec{F_w} + \vec{F_{fus}} + \vec{F_t} + \vec{F_v} \\ \vec{M_{tot}} = \vec{M_R} + \vec{M_p} + \vec{M_w} + \vec{M_f} + \vec{M_t} + \vec{M_v} \end{cases} \tag{40}$$

A total of 12 states are part of this model's system of equations and they are listed below;

- The body velocities: $\vec{u} = \begin{bmatrix} u & v & w \end{bmatrix}^T$

- The Euler angles that express the vehicle's attitude with respect to the $O^nx^ny^nz^n$ frame: $\vec{\theta} = \begin{bmatrix} \varphi & \vartheta & \psi \end{bmatrix}^T$

- The body angular velocities: $\vec{\omega} = \begin{bmatrix} p & q & r \end{bmatrix}^T$, and

- The quasi-dynamic inflows of the rotor and the two propellers described earlier: $\vec{\lambda_0} = \begin{bmatrix} \lambda_0 & \lambda_{0pp} & \lambda_{0ps} \end{bmatrix}^T$

Note the positional vector $\begin{bmatrix} x & y & z \end{bmatrix}^T$ is not of interest in this study as the purpose is the finding of steady-state operating points in forward flight, and these states are necessary in control-system design, and simulation of maneuvering flight. This article assumes a rigid body with constant mass M and inertia $\mathbf{J}$ moving along a flat, non-rotating Earth with a uniform gravity field of acceleration $\vec{g}$. The final EOMs is a final set of differential equations, to be solved, and fed back to the system dynamically as states next to the inputs. In the computational aspect of this thesis, their solution was obtained using Runge-Kutta numerical integration, by way of the MATLAB® function *ode45*. They are firstly comprised of the translational dynamics of Equation 41, where the second factoy of the right-hand side entails the gravitational force transformation to the body frame, which in some expression in literature, is embedded in the $\mathbf{F_{tot}}$ vector.

$$\dot{\mathbf{u}} = \frac{1}{M}\mathbf{F_{tot}} + \mathcal{T}_n^b\begin{bmatrix} 0 & 0 & g \end{bmatrix}^T - \omega \times \mathbf{u} \tag{41}$$

In the absence of the positional vector, that was just mentioned, the kinematics of the translational motion are not included in the EOMs, but for expansion of this model, they are represented by the differential equation $\dot{\mathbf{x}} = \mathcal{T}_b^n\mathbf{u}$, where $\dot{\mathbf{x}}$ is the derivative of $\begin{bmatrix} x & y & z \end{bmatrix}^T$ and $\mathcal{T}_b^n = \{\mathcal{T}_n^b\}^{-1}$ is the transformation back to the NED frame. Additionally, the definitions of the dynamics and kinematics of the rotational motion are respectively displayed in Equations 42 and 43.

$$\dot{\omega} = \mathbf{J}^{-1}[\mathbf{M_{tot}} - \omega \times \mathbf{J}\omega] \tag{42}$$

$$\dot{\theta} = \mathcal{O}_b^n\omega \tag{43}$$

Although, translational kinematics are not included, the rotational description is necessary to this research, as the orientation of the vehicle relative to the NED frame in steady-state operation is vital. Lastly, the three quasi-dnamic inflows are part of the EOMs, all three of which follow the same expression as that of Equations 8, 20 and 21. Now that the mathematical model is finalized, and ready to be manipulated dynamically, the following steps towards a linearized compound helicopter will be investigated.

3 Trim

Having modelled the 9-DoF compound helicopter thoroughly under valid assumptions and approximations, the research proceeds to the trim phase of said model. In this section, steady-state operating points are discovered throughout the vehicle's airspeed range in forward flight, under which it will function in mechanical equilibrium. Over the years, a wide range of Control Allocation (CA) methods has been developed, catering to both linear and non-linear aerodynamic models. Extensive research on CA methods has been conducted, and a comprehensive survey can be found in [8]. These methods typically involve solving an optimization problem to determine the most effective control forces. In some CA formulations, the primary

objective is to minimize the disparity between the desired control forces and the achieved forces, as depicted in Equation 44. However, other methods go beyond this and aim to optimize additional parameters, such as the displacement of total effectors, trim drag ([9],[10]), or structural loads [11]. By considering these secondary parameters, these advanced CA approaches offer the potential for further performance enhancements and operational efficiency.

$$\min_{\delta} \mathcal{G} = \|\Delta\mathbf{C_F} - \mathbf{B}\delta\| \tag{44}$$

The challenge that is presented now, is the redundant number of available control inputs on the aircraft. That is, in order to achieve higher cruise speeds, as is the goal of compound helicopters, the total control effort has to be allocated among the actuators, which then should lead to the slowing of the main rotor, avoiding therefore compressibility effects on the advancing side and dynamic stalling on the retreating side. The second of the fundamental problems of flight dynamics concerns trim and states there exists a set of state and input vectors $\mathbf{X}^*$ and $\mathbf{U}^*$ such that:

$$f(\mathbf{X}^*, \mathbf{U}^*) = 0 \tag{45}$$

and in this particular case:

$$f(\mathbf{X}^*, \mathbf{U}^*) = \dot{\mathbf{X}} = \begin{bmatrix} \dot{\mathbf{u}} & \dot{\theta} & \dot{\omega} & \dot{\lambda}_0 \end{bmatrix}^\mathrm{T} \tag{46}$$

For clarity, the function f here is the derived nonlinear model. In literature, the section focusing on the trim is a relatively small one, as it is usually a straightforward process. Most aircraft models are critically actuated, leading to an analytical trim that will provide a unique solution $(\mathbf{X}^*, \mathbf{U}^*)$ for each operating condition in the flight envelope. This is not the case in discussion here. More specifically, the control inputs vector $\mathbf{U}$ is displayed in Equation 47. In literature, the control of the propellers have been represented by inputs $\bar{\theta}_{0p}$ and θ_{diff}, meaning mean and differential propeller pitch instead of directly having available ϑ_{0pp} and ϑ_{0ps} [12]. However, the only difference the first version makes, is two additional equations, a sum and a subtraction of the two within the model.

$$\mathbf{U} = \begin{bmatrix} \vartheta_0 & \vartheta_{1s} & \vartheta_{1c} & \vartheta_{0pp} & \vartheta_{0ps} & \delta_e & \delta_r \end{bmatrix}^\mathrm{T} \tag{47}$$

Between this, and the 12-entry state vector, the objective leads to a trim vector showed below.

$$\mathbf{u_{trim}} = \begin{bmatrix} \varphi & \vartheta & \lambda_0 & \lambda_{0pp} & \lambda_{0ps} & \mathbf{U}^\mathrm{T} \end{bmatrix}^\mathrm{T} \tag{48}$$

Thus, this is evidence of an over-actuated system, for which analytical trim is not possible, as the system is highly coupled, meaning there is multiple instances where more than one controls affect a single motion of the helicopter, either translational or rotational. Mathematically, this case serves as an under-determined system of equations, with more unknowns than equations in place. The solution is searched therefore, by means of numerical trim optimization.

3.1   Trim Optimization

Gaining a deeper physical comprehension and insight into the behavior of a compound helicopter system can potentially expedite the identification of optimal control parameters. This could entail determining which redundant controls have greater efficacy and which ones exhibit less sensitivity towards specific objectives, or identifying the optimal sequence for executing redundant controls and their corresponding effects. This knowledge base could significantly reduce the search space for both numerical optimization algorithms and fly-to-optimal approaches, thereby enabling a faster in-flight determination of the optimal state [13]. In the context of model-based optimization, a common approach to compute a steady-state operating point involves imposing constraints on the system variables, inputs, or outputs. These constraints may take the form of fixed values or bounds, which guide the optimization search towards a suitable solution. Nevertheless, in certain scenarios, the optimization search may benefit from increased flexibility in the definition of its parameters to accommodate specific system requirements or application constraints. The main element in need of definition during numerical optimization are an objective function given by;

$$\text{cost} = \min_{\mathbf{u_{trim}}} \mathbf{J} = \arg\min_{\mathbf{u_{trim}}} \left\| \dot{\mathbf{X}} \right\|,$$
$$\text{subject to} : \mathbf{c(U)} : \delta_{\mathbf{lb}} \leq \mathbf{U} \leq \delta_{\mathbf{ub}} \tag{49}$$

where Table 1 outlines the constraint function set $\mathbf{c(U)}$, sourcing from the physical upper- and lower-bound limits of the actuators. Computational optimization algorithms interpret equalities and inequalities separately, but given their decimal points size, essentially the constraints follow the "less than or equal to" constraint. Furthermore, these can only be coded as one-sided, meaning the table translates to 14 constraints applied to the algorithm.

Table 1: Controls limits

Constraints	Limits
Rotor Collective	$0.4° \leq \vartheta_0 \leq 16.4°$
Longitudinal cyclic	$-16° \leq \vartheta_{1s} \leq 16°$
Lateral cyclic	$-8° \leq \vartheta_{1c} \leq 8°$
Port-side propeller pitch	$0.4° \leq \vartheta_{0pp} \leq 16.4°$
Starboard-side propeller pitch	$0.4° \leq \vartheta_{0ps} \leq 16.4°$
Elevator	$-25° \leq \delta_e \leq 15°$
Rudder	$-15° \leq \delta_r \leq 15°$

The point of this subsection has been to overcome the hurdle of not being able to obtain an operating point analytically. However, remaining in this stage is still not a desirable result. Let the aforementioned formulation of Equation 49 and Table 1. Given the physical capabilities there exist multiple operating points $\text{OP}_k = \{\mathbf{X}^*, \mathbf{U}^*\}$ that follow the relation;

$$\text{OP}_k \in \mathbb{S}^7 \quad \forall k \in \{1, 2, 3, ...n\} \tag{50}$$

where $\mathbb{S}^7$ is the seven-dimensional space of solutions that satisfy Equation 49 at a single forward airspeed under the applied optimization tolerance. Lowering this tolerance will potentially reduce the size of this set but still to a non-singular amount of solutions. The next approach at this point can take many directions depending on the goal of the study, such as a secondary objective function making this solution a multi-objective optimization. This research however, utilizes the methods of control allocation to obtain the required operating points.

3.2   Control Allocation

In this field, various processes are devised in order to either tackle the over-actuation problem, or eliminate part of a control effort in certain scenarios. Suppose a system with a control effectiveness matrix $\mathbf{B_e}$ as defined below. The highlighted problem exists when the matrix is non-square, and more columns are present than rows. As it is known in classical control theory and linear algebra, the inverse of such matrix cannot be computed, and so, no direct solution can be found.

$$\mathbf{B_e} = \begin{bmatrix} \frac{\partial L}{\partial \delta_1} & \frac{\partial L}{\partial \delta_2} & \cdots & \frac{\partial L}{\partial \delta_n} \\ \frac{\partial M}{\partial \delta_1} & \frac{\partial M}{\partial \delta_2} & \cdots & \frac{\partial M}{\partial \delta_n} \\ \frac{\partial N}{\partial \delta_1} & \frac{\partial N}{\partial \delta_2} & \cdots & \frac{\partial N}{\partial \delta_n} \end{bmatrix} \qquad (51)$$

In the field of control allocation, strategies are searched for in order to bring this matrix to invertible form, and obtain a set of inputs as a result to the trim problem, most of which have been attempted, and a particular one proved the best. Explicit ganging, firstly, is an a priori method for combining or ganging effectors in order to produce a single effective control from multiple devices. Additionally, the weighted Moore-Penrose pseudo-inverse matrix has been calculated according to [14]:

$$\mathbf{B_{mp}} = \mathbf{W}^{-1}\mathbf{B_e}^T \left(\mathbf{B_e}\mathbf{W}^{-1}\mathbf{B_e}^T\right)^{-1} \qquad (52)$$

It should be noted as a reminder, that this system is non-linear, which implies that the control-effectiveness matrix $\mathbf{B_e}$ is not readily available, in order for this method to be given a try. It has therefore, been manually constructed, after initially trimming the model numerically, obtaining one of the operating points in the solution subspace $\mathbb{S}^7$, and then perturbing the inputs from their trimmed state to come up with the required matrix. This virtual "re-allocation" method, requires a solution subspace that is not null, and non-singular. In literature, control allocation is applied primarily in control systems desing, in which stage, an linear system is potentially already available, where as here, it is the final goal. Furthermore, it is inefficient for the weighted methods to be used as such, because multiple instances of trial and error have to happen to get a unique useful $\mathbf{W}$ matrix for each airspeed in trim. The resulting method that has been followed overall, is a Direct Allocation, by means of a mapping function f_{CA} in the optimization, which also uses weighted penalization of certain undesirable controls.

$$f_{CA}(\mathbf{U}) = \delta_{\mathbf{lb}} \leq \mathbf{WU} \leq \delta_{\mathbf{ub}}$$

$$\text{with} : \mathbf{W} = \begin{bmatrix} w_1 & 0 & \cdots & 0 \\ 0 & w_2 & \cdots & 0 \\ \vdots & \vdots & \ddots & \vdots \\ 0 & 0 & \cdots & w_7 \end{bmatrix} \qquad (53)$$

Along the forward flight speed range, the penalty of the longitudinal cyclic increases at higher speeds, in order for the propellers to be used primarily for forward thrust. The empennage surfaces are constantly weighed by a small factor, in order. The collective left unallocated as it only adds vertical thrust on top of the wing lift, when necessary. Similarly, the lateral cyclic is unallocated since it is the only input that controls the rolling motion. The product of this methodology is outlined in the Results section.

4   Results

This section presents findings of this research, and helps visualize methods explained earlier. It is important to show that the trim and linearization methodologies have worked on the derived model, and that the high cruise speeds that are targeted are theoretically reached while at the same time avoiding there undesirable aerodynamic consequences on the main rotor.

4.1   Compressibility assumption

Firstly, one should account for the ultimate goal, which is achieving a cruise speed range up to 255 knots, with a slowed rotor rotational velocity. Specific effect to be bypassed here, is drag divergence at the tip of the advancing blade, the fastest moving segment of the helicopter. The occurrence is the abrupt increase in drag, at certain Mach numbers. Experimentally, it has been shown that this happens between $M = 0.85$ and $M = 0.92$ [15]. Following the modelling of Ferguson, the Mach bound to stay under, is chosen to be $M = 0.89$ [16]. Figure 3 shows the rise of the advancing blade tip Mach number, across the forward speed range of the flight envelope, but also the aforementioned Mach bound.
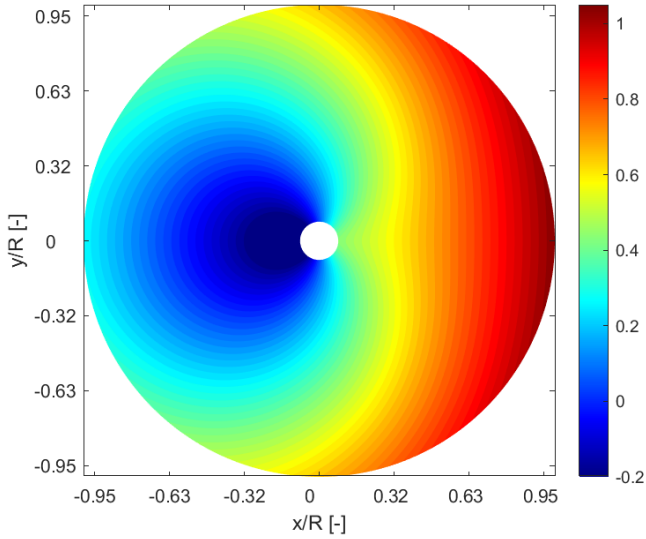
Figure 2: Rotor disc M at u = 255kts before RPM reduction
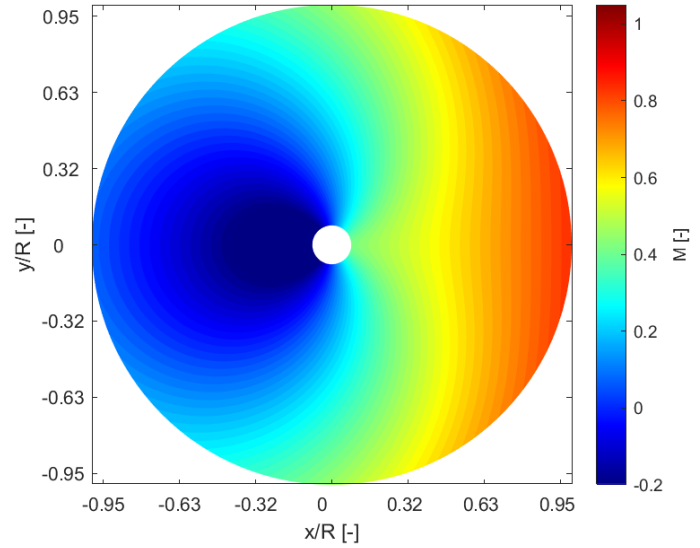
Figure 4: Rotor disc M at u = 255kts after RPM reduction

Ferguson's approach is a logarithmic-like reduction of the rotational velocity of the rotor with larger drops at larger airspeeds. The solution here is chosen is to linearly reduce the rotational velocity of the rotor after 125 knots, in order to have the tip M value remain at around 0.85.
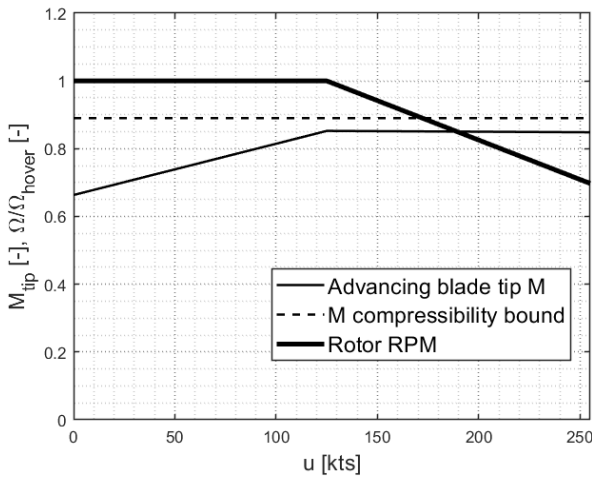
By linearly reducing the rotational velocity from the hover Ω at u = 125kts, the contour significantly improved overall, but especially at the advancing blade region, as Figure 4 shows.

4.2   Allocation strategy

For the procedure of control allocation, it has been stated that a mapping function narrows the range of selection of control input combinations. This is done by amplifying the value of inputs by means of weights, which leads to the larger values being filtered out by the constraint function, so that the smaller ones are only available for the optimization function. As it can be imagined, an entire field of avenues is available to be taken from here, and various different weight combinations would be valid. The approach taken in this project, was a sensitivity analysis of individually weighing the inputs, and documenting all trim results. In each cycle, each of the inputs that would be manipulated, were weighed solely, at 3 different factors, and left unweighted too. This occured for the longitudinal cyclic, for the two propeller pitches combined, and for the empennage surfaces combined.

Figure 3: Advancing blade tip Mach number with rotor speed reduction

The scale of the factor is in need of explanation too. As clarified, the role of the mapping function weights is the isolation of smaller input absolute values. The scale, therefore, of the weights is directly depended on how small a region one wants to isolate in a control actuator range. It has been chosen in this case, that power scales of 10 fulfill this purpose, and the more undesirable the input will be, the higher the power of 10 on the weight of the function. Due to the highly coupled character of the model, a weight on a single input will undoubtedly affect many of the other ones too. For this reason, the weighing is focused on the share of forward thrust between the longitudinal cyclic and the two propeller pitch controls. In the transition range from hover to around 60 knots, the cyclic is favored to the other two, whereas from 60 knots onward, the opposite holds. In both cases, after the trial of multiple weights, the exponent

The figure shows the first step of this research's strategy, in which the compound vehicle breaks the aerodynamic "ceiling" of conventional helicopter performance. It is possible because it has still reach larger speeds, thanks to the auxiliary thrust mechanisms.

operating point is chosen as initial guess for the optimization of the nexto one. Such a method is needed, in similar problems, where there is a large number of available solutions, which is hard to navigate through. In combination with the inherent instabilities of helicopters, a smooth change in controls needs to be present, so that no large jump of input is needed suddenly. The following spider plots give a visual representation of how the controls of the aircraft are distributed following the trim process. Note that, outside of the three collectives, the axes are in absolute value, because the amount of deflection from zero is important to see, rather than the actual sign of the controls.

Initially, in Figure 6 a single line can be seen. The reason for this is that it has been the only stage in which control allocation has not been necessary. For hover, there is not airflow for the empennage surfaces to manipulate, so then, they are simply not deployed, which stops making the system over-actuated. In the adjacent two plots, the distribution of the control effort is shown for a low speed of 50 knots, and a high one of 200 knots. In them, the unallocated controls are seen in the dashed-blue contour, and the final distribution after control allocation in the shaded red region.
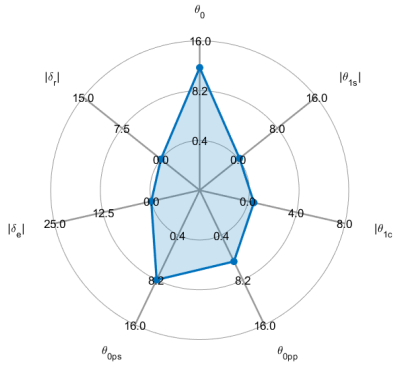
Figure 6: Control effort in hover
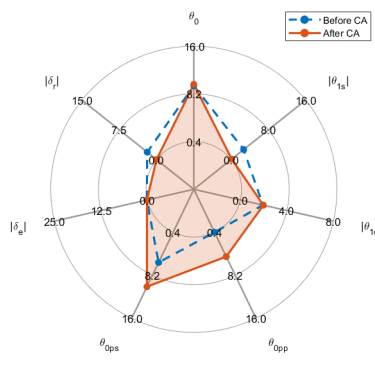
Figure 7: Control effort at u = 50kts
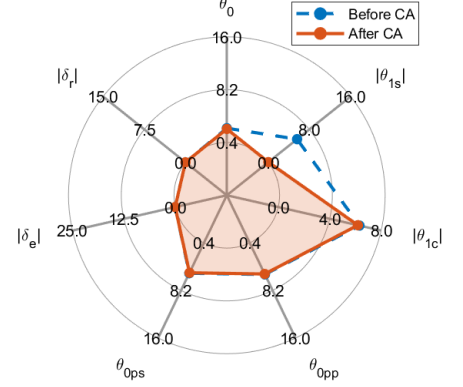
Figure 8: Control effort at u = 200kts
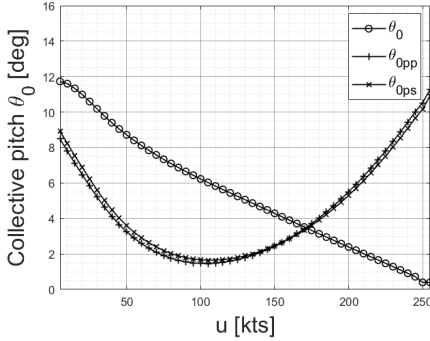
Figure 9: Collective pitch trim
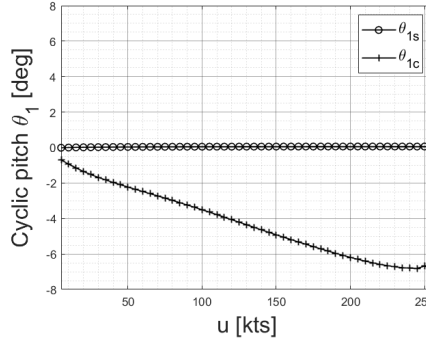
Figure 10: Cyclic trim
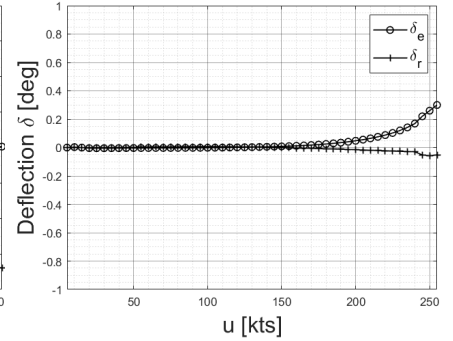
Figure 11: Empennage deflections trim

In hover, the inputs δ_e and δ_r are at zero, as said before. The rotor collective is at its maximum value, since no lift-compounding takes place in the absence of airflow around the wing. Actually, the collective is even larger than it would be for the same helicopter without a wing, meaning not only does the wing not help with a lift force it hover, but it is a drawback, since its position in the middle of the rotor wake creates an induced download on the vehicle, to be compensated by the main rotor. The yaw control by the propellers can be visible by the slightly higher starboard propeller pitch value, which result in a higher thrust value, which in turn leads to a compensatory yaw moment. Regarding the two plots for forward flight, there

is clear reduction of the rotor collective as speed increases, and the differential thrust remains present. Furthermore, the mean propeller pitch increases with speed, so that the required thrust is provided. Lastly, the very clear drop between the two contours is the one of the longitudinal cyclic of the rotor, an effect of the applied weights from subsection 4.2. In the end, the overall trim results of all controls at all airspeeds are viewed in Figures 9, 10 and 11.

4.4   Attainable Moment Set

The collection of moments that can be generated by the actuators at any operating point in this study is known in the field as
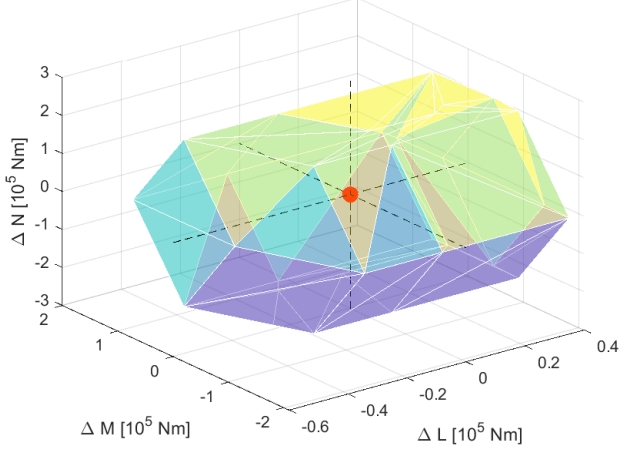
Figure 12: AMS from OP at u = 50kts
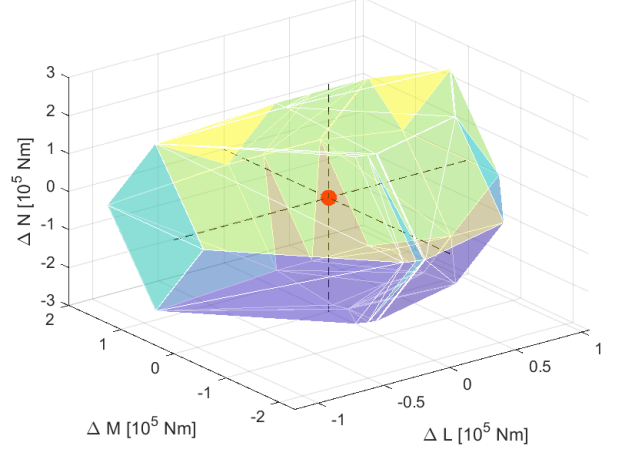
Figure 13: AMS from OP at u = 200kts

the Attainable Moment Set (AMS) or sometimes as Effective Moment Set. It results from a hyper-rectangle in the seven-dimensional Control Space $\mathbb{R}^7$, the Admissible Controls Set (ACS), containing all possible combinations of inputs, and not to be confused with the set $\mathbb{S}^7$ from earlier, which has only the ones that satisfy the objective function. The characterization of the AMS in the presence of non-linearities and couplings within the control effectors' aerodynamic model poses a significant challenge. Linearizing the aerodynamic model with respect to control positions enables the definition of a linear function utilizing the control effectiveness matrix $\mathbf{B_e}$, serving as an approximation of the mapping between the ACS and the AMS. It has been proven that the resulting AMS exists as a bounded convex polytope in three-dimensional space $\mathbb{R}^3$ [17]. The construction of the AMS entails employing a geometric algorithm detailed in [18] for scenarios where the number of control effectors is either 2 or 3. Additionally, an extension of this algorithm has been proposed in [19] to encompass systems with arbitrary dimensions in Moment Space. Here, the AMS then, is a convex hull in the Cartesian axis system in $\mathbb{R}^3$ with the change in moments Δ_L, Δ_M and Δ_N placed on each axis. It encloses all possible moment perturbation vector, attainable at a specific dynamic point, hence the name. Figures 12 and 13 display it for the operating points OP at low and high speed.

An additional feature is that when the non-linear model is linearized with respect to the operating points, the control effectiveness matrix $\mathbf{B_e}$ of Equation 51 defines a linear function which maps the ACS to the AMS. The attribute of interest, though, is the trim point, indicate by the red marker at the origin of all surface plots. In a research of equilibrium search, it is necessary to show the dimension size of this problem that has been mentioned. Similarly to how $\mathbf{B_e}$ maps any point of the ACS to the surface, the pseudo-inverse fulfills the opposite route, and the function created in this study f_{CA} maps the trim point back to the solution space $\mathbb{S}^7$. This result is vital as it not only shows the order of the complex derived model, but also is a blueprint for coordination within it. these results, are crucial for the design of a control allocator, to follow a controller in a feed-forward loop, that will get fed a control effort vector

necessary, which will lead to a smaller region within the AMS, called the Rerquired Moment Space (RMS), and will output a mapped solution to command the actuators. The projections from front, side and top are available in appendix A.5.

5   Conclusions

The findings of this research have been in multi-layer form, and highlight the novel methods utilized in the field of flight dynamics and numerical trim optimization. Primarily, the study has concluded with a complete, linear 9 DoF mathematical model, to be analyzed in terms of its stability and response, as well as manipulated in simulation of desirable manoeuvres and trajectories. With an operating point sought for every 5 knots of forward flight airspeed from hover to 255 knots, the system's behaviour is transparent along the froward flight envelope when under stability analysis and it assists for an efficiently designed control subsystem.

Secondly, it has been proven that the presence of auxiliary lift and propulsion in this compound helicopter configuration play a crucial role in its significant flight envelope expansion. The idea around which the concept was initially thought of, meaning the achievement of greater cruise speeds than the attainable ones by the conventional helicopter, is deemed valid here. From 125 knots onward, the the rotor has been linearly slowed in rotational velocity, resulting in 75% of its hover value, bypassing thus the compressibility effects such as drag divergence at the advancing blade and dynamic stall at the retreating blade. Following the control allocation process, the rotorcraft has still been able to have its effort redistributed among the available controls, and still reach said airspeed. In terms of a conversion corridor in the transition phase of the flight envelope, no such pattern has been found to exist, as there is a multitude of input combinations that can take place to gradually increase forward flight speed, depending on the corresponding weight selection.

Additionally, the over-actuation problem has been thoroughly

addressed, with a greater set of unknowns than equations, which leads to an under-determined system. This means analytical trim is not possible here, so numerical optimization takes place. With the ordinary objective function which is the minimization of the state derivative vector, and the constraint function, a custom mapping function has been created, which applies weights to penalize unwanted inputs, by leaving the smaller indices only available. The result is not only the 52 available operating points for the forward flight speeds, but also the collection of attainable moment sets. These are the product of the control allocation process, and give information on the maneuverability of the vehicle at each of these points. The adapted control mapping method, is applicable to any similar over-actuated dynamical system with the same objective function, and particularly in the domain of hybrid compound rotorcraft.

6   Recommendations

For research completeness, certain points are to be put forward in which further development would be beneficial for the field.

- It has been mentioned that the lateral cyclic is the sole control input available for roll manipulation. It is in the best interest of the model in terms of fidelity that a set of aileron surfaces are modelled at the wing. As it can be seen from the AMS surface, rolling maneuverability is around half of the other two axes. Incorporation of ailerons will improve that significantly, but will also prevent lateral cyclic saturation, which is imminent.

- In order to fulfill the flight envelope expansion capabilities it is essential that the scope be broadened towards climbing flight. It is suggested that the climb angle γ be varied in steps for a constant airspeed vector $\mathbf{V}$ initially, and that then the latter is varied for constant climb angles, while remaining within rate of climb limits, in order to have the entire flight envelope graphed and compared to that of the Eurocopter EC155.

- Regarding the inflow of the rotating components, a more sophisticated model can be implemented, most of which have been documented in the literature study of this research. Specifically, a quasi-dynamic inflow model can be advanced to a Peters-He or Pitt-Peters dynamic inflow one. Rotor and propeller performance are key to the dynamic response of this research, and could therefore be explored further in terms of fidelity.

- Vital is also the modelling of the aerodynamic interaction between components around this vehicle. In this study, this has been modelled by means of interference factors in the aerodynamic equations. However, a more complex method such as wind-tunnel data in the form of lookup tables would favor the progress. Recently, Laurianne Lefevre has conducted significant work with experimentation in rotor-propeller interaction, so research in the topic is advised ([20],[21]).

It is not effective for a study not to provide insight on how it can be used for further research, and while controlling and analyzing the model in its stability is the obvious route from here, the aforementioned discussion items are crucial in the improvement of said model.

A   Appendices

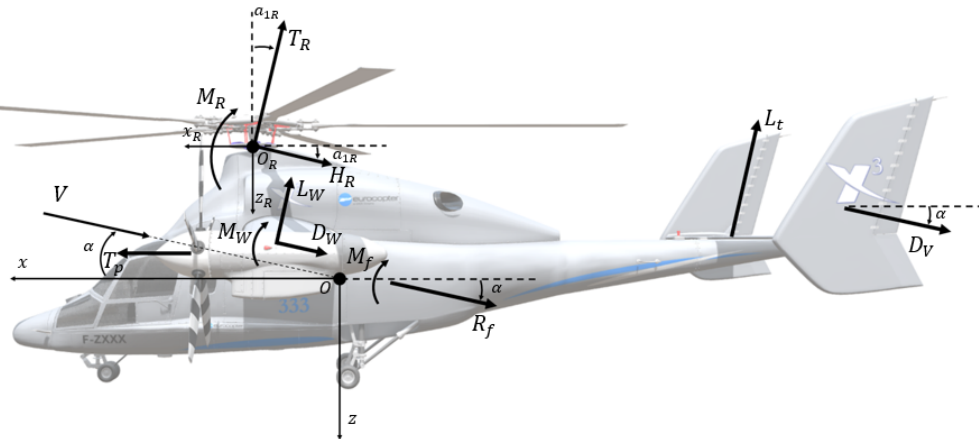## A.1   Free-body diagrams

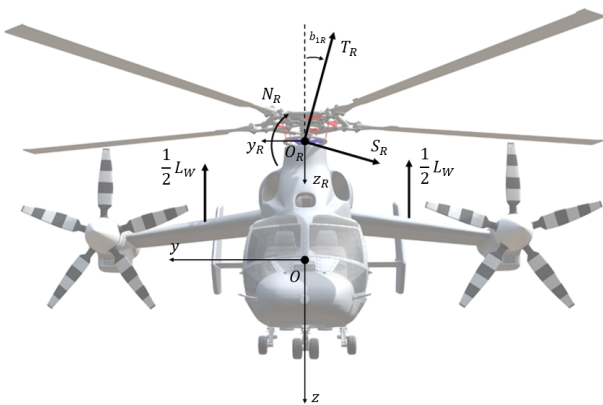Figure 14: Free-body diagram port side view

Figure 15: Free-body diagram front view
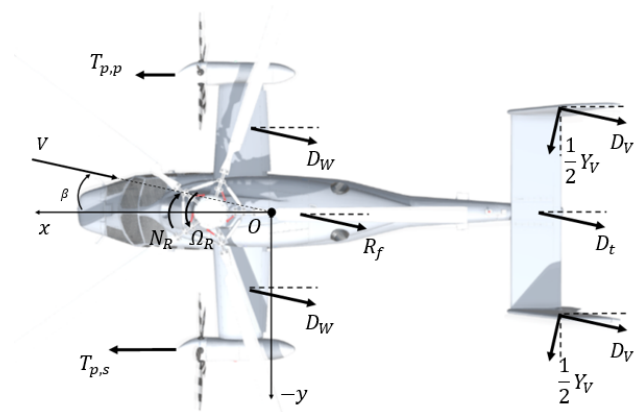

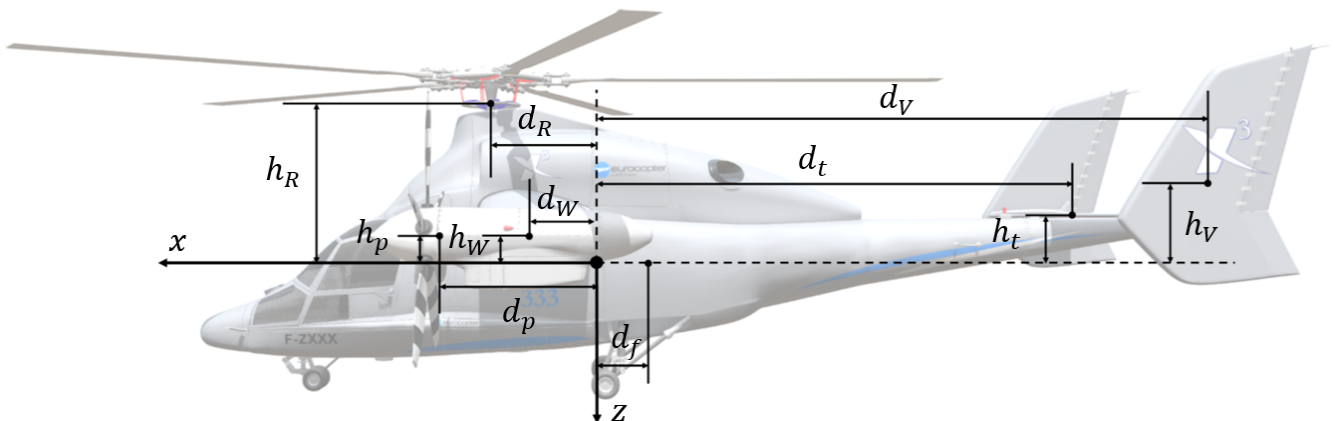Figure 16: Free-body diagram top view

A.2   Moment arms schemes
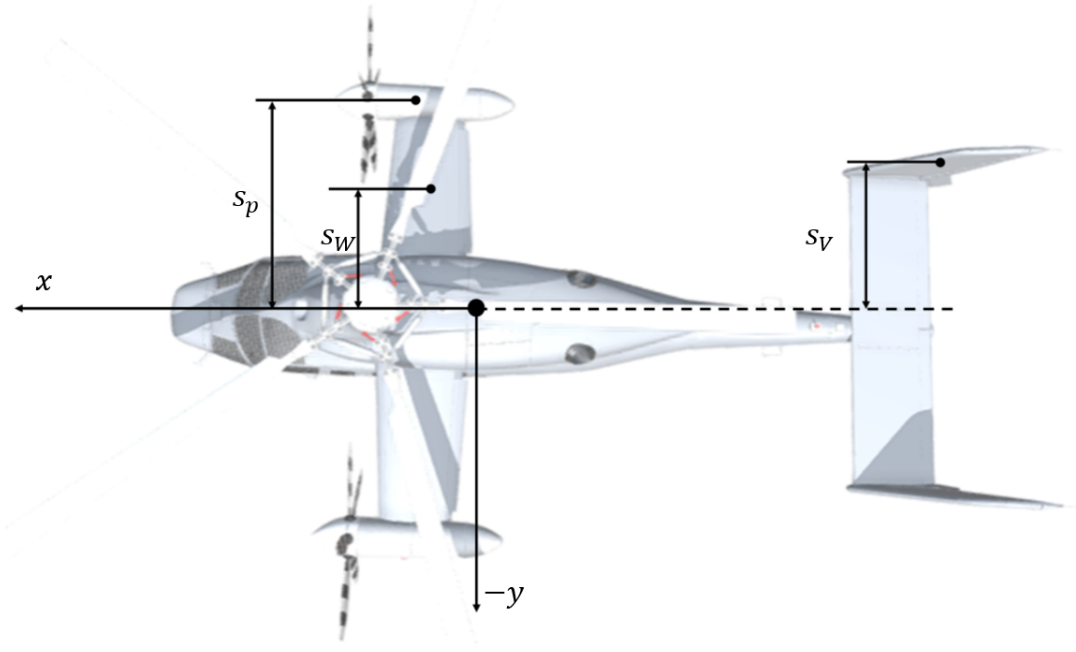

Figure 17: Moment arms from port-side view

14

Figure 18: Moment arms from top view

A.3   Transformations

Rotation definitions:

$$\mathcal{R}_x(t) \triangleq \begin{bmatrix} 1 & 0 & 0 \\ 0 & \cos t & \sin t \\ 0 & -\sin t & \cos t \end{bmatrix} \qquad \mathcal{R}_y(t) \triangleq \begin{bmatrix} \cos t & 0 & -\sin t \\ 0 & 1 & 0 \\ \sin t & 0 & \cos t \end{bmatrix} \qquad \mathcal{R}_z(t) \triangleq \begin{bmatrix} \cos t & \sin t & 0 \\ -\sin t & \cos t & 0 \\ 0 & 0 & 1 \end{bmatrix}$$

NED frame to body-fixed transformation:

$$\mathcal{T}_n^b(\varphi, \vartheta, \psi) = \mathcal{R}_x(\varphi)\mathcal{R}_y(\vartheta)\mathcal{R}_z(\psi) = \begin{bmatrix} \cos\psi\cos\vartheta & \sin\psi\cos\vartheta & -\sin\vartheta \\ \cos\psi\sin\vartheta\sin\varphi - \sin\psi\cos\varphi & \sin\psi\sin\vartheta\sin\varphi + \cos\psi\cos\varphi & \cos\vartheta\sin\varphi \\ \cos\psi\sin\vartheta\cos\varphi + \sin\psi\sin\varphi & \sin\psi\sin\vartheta\cos\varphi - \cos\psi\sin\varphi & \cos\vartheta\cos\varphi \end{bmatrix}$$

NED frame to velocity frame transformation:

$$\mathcal{T}_n^v(\gamma, \chi) = \begin{bmatrix} \cos\chi\cos\gamma & \sin\chi\cos\gamma & -\sin\gamma \\ -\sin\chi & \cos\chi & 0 \\ \cos\chi\sin\gamma & \sin\chi\sin\gamma & \cos\gamma \end{bmatrix}$$

NED frame to body-fixed frame angular velocity transformation:

$$\mathcal{O}_n^b(\varphi, \vartheta) = \begin{bmatrix} 1 & 0 & -\sin\vartheta \\ 0 & \cos\varphi & \sin\varphi\cos\vartheta \\ 0 & -\sin\varphi & \cos\varphi\cos\vartheta \end{bmatrix}$$

Body-fixed frame to NED frame angular velocity transformation:

$$\mathcal{O}_b^n(\varphi, \vartheta) = \{\mathcal{O}_n^b(\varphi, \vartheta)\}^{-1} = \begin{bmatrix} 1 & \sin\varphi\tan\vartheta & \cos\varphi\tan\vartheta \\ 0 & \cos\varphi & -\sin\varphi \\ 0 & \sin\varphi/\cos\vartheta & \cos\varphi/\cos\vartheta \end{bmatrix}$$

Control plane to disc plane transformation:

$$\mathcal{T}_{cp}^{dp}(a_1, b_1) = \mathcal{R}_y(a_1)\mathcal{R}_x(b_1) = \begin{bmatrix} \cos a_1 & \sin a_1 \sin b_1 & -\sin a_1 \cos b_1 \\ 0 & \cos b_1 & \sin b_1 \\ \sin a_1 & -\cos a_1 \sin b_1 & \cos a_1 \cos b_1 \end{bmatrix}$$

Disc plane to body-fixed frame transformation:

$$\mathcal{T}_{dp}^{b}(a_{1R}, b_{1R}) = \mathcal{R}_y(-a_{1R} - \gamma_s)\mathcal{R}_x(-b_{1R}) = \begin{bmatrix} \cos(a_{1R} + \gamma_s) & \sin(a_{1R} + \gamma_s)\sin b_{1R} & \sin(a_{1R} + \gamma_s)\cos b_{1R} \\ 0 & \cos b_{1R} & -\sin b_{1R} \\ -\sin(a_{1R} + \gamma_s) & \cos(a_{1R} + \gamma_s)\sin b_{1R} & \cos(a_{1R} + \gamma_s)\cos b_{1R} \end{bmatrix}$$

A.4   Model Design Parameters

Table 2: Rotor parameters

Parameter	Symbol	Value	Unit
Radius	R	6.3	m
Rotational velocity in hover	Ω_h	38.5	rad/s
Number of blades	N	5	-
Blade lift curve slope	C_{L_α}	5	rad^{-1}
Tilt angle	γ_s	0.06	rad
Blade mass	m_{bl}	30	kg
Blade moment of inertia about the flapping hinge	I_β	396.9	kg/m^2
Equivalent blade chord	c_e	0.3	m
Angle of twist	ϑ_{tw}	-0.14	rad
Induced flow time constant	τ_{λ_0}	0.1	s

Table 3: Propeller parameters

Parameter	Symbol	Value	Unit
Radius	R_p	1.2	m
Number of blades	N_p	5	-
Rotational velocity	Ω_p	305	rad/s
Blade lift curve slope	$C_{L_{\alpha p}}$	5	rad^{-1}
Equivalent blade chord	c_{ep}	0.15	m
Angle of twist	ϑ_{twp}	-9	deg
Induced flow time constant	$\tau_{\lambda_{0p}}$	0.1	s
Aerodynamic interference factor	K_p	2	s

Table 4: Wing parameters

Parameter	Symbol	Value	Unit
Surface area	S_w	10	m^2
Lift curve slope	$C_{L_{\alpha w}}$	5	rad^{-1}
Zero-AoA Lift coefficient	C_{L_0}	0.3	-
Drag polar offset	C_{D_0}	0.02	-
Aspect ratio	AR	5	-
Oswald efficiency factor	e_0	0.89	-
Aerodynamic interference factor	K_w	2	-
Anhedral angle	Γ	5	deg

Table 5: Empennage parameters

Parameter	Symbol	Value	Unit
Lift curve slope	$C_{L_{\alpha t}}$	3.5	-
Lift-elevator slope	$dC_{L_{\alpha t}}/d\delta_e$	0.859	rad^{-1}
Drag-elevator slope	$dC_{D_{\alpha t}}/d\delta_e$	0.03	rad^{-1}
Horizontal tail Incidence angle	α_{0t}	0.07	rad
Horizontal tail surface area	S_t	2.5	m^2
Aerodynamic interference factor	K_t	1.5	-
Y-force curve slope	$C_{Y_{\beta v}}$	4	-
Drag-rudder slope	$dC_{D_{\beta v}}/d\delta_r$	0.03	rad^{-1}
Y-rudder slope	$dC_{Y_{\beta v}}/d\delta_r$	0.859	rad^{-1}
Vertical tail Incidence angle	β_{0v}	-0.08	rad
Vertical tail surface area	S_v	2	m^2

Table 6: Moment arms

Parameter	Symbol	Value	Unit
Rotor x-arm	d_R	1.12	m
Rotor z-arm	h_R	1.7	m
CG y-offset	s_{off}	0.03	m
Propeller x-arm	d_p	1.66	m
Propeller z-arm	h_p	0.28	m
Mean propeller y-arm	s_p	2.38	m
Wing x-arm	d_w	0.73	m
Wing z-arm	h_w	0.3	m
Horizontal tail x-arm	d_t	5.10	m
Vertical tail x-arm	d_v	6.58	m
Vertical tail z-arm	h_v	0.88	m

Table 7: Fuselage parameters

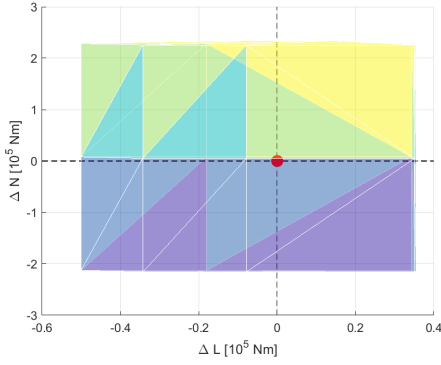| Parameter	Symbol	Value	Unit
Equivalent flat plate area	F_0	18	m^2
Side view body volume having circular sections	V_{fusM}	25.53	m^3
Top view body volume having circular sections	V_{fusN}	6.13	m^3
Aerodynamic interference factor	K_f	0.83	-

A.5 AMS Projections

Figure 19: Front view
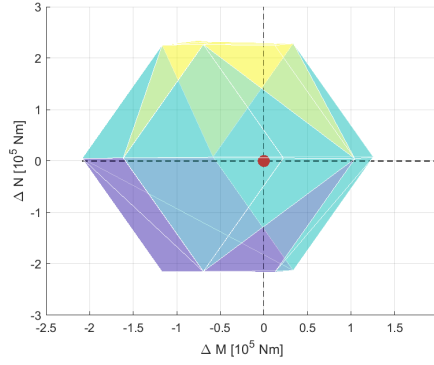
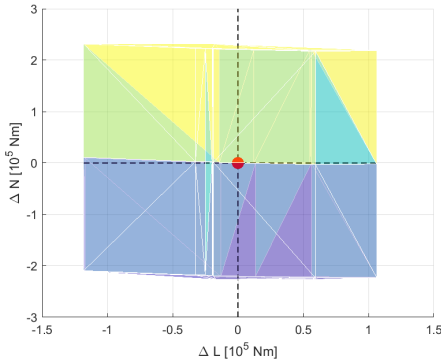

Figure 20: Side view
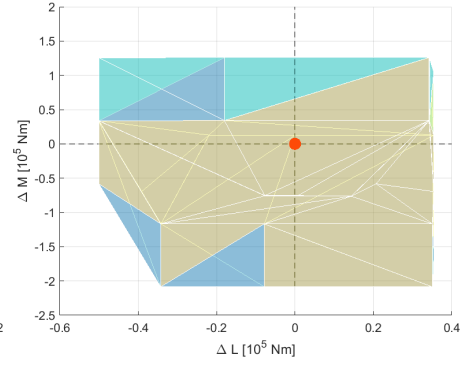
Figure 21: Top view

Low speed: u = 50kts

Figure 22: Front view
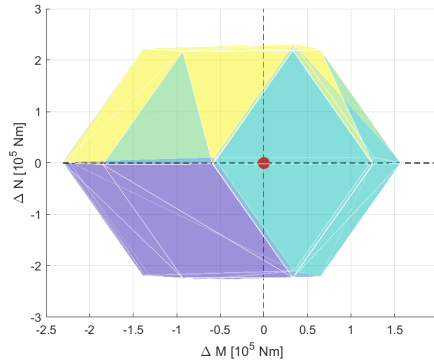
Figure 23: Side view
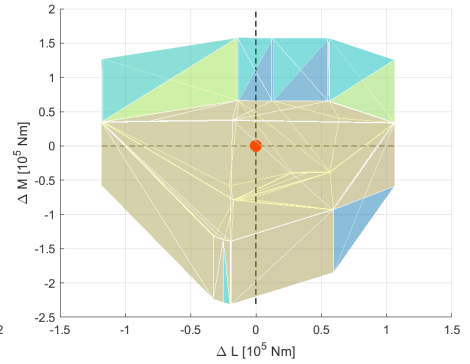
Figure 24: Top view

High speed: u = 200kts

A.6 System & Conrtol Matrices

Hover

$$\mathbf{A} = \begin{bmatrix}
0.000 & 0.000 & 0.000 & 0.000 & 0.000 & 0.000 & 1.000 & 0.001 & 0.136 & 0.000 \\
0.000 & 0.000 & 0.000 & 0.000 & 0.000 & 0.000 & 0.000 & 1.000 & -0.008 & 0.000 \\
0.000 & 0.000 & 0.000 & 0.000 & 0.000 & 0.000 & 0.000 & 0.008 & 1.009 & 0.000 \\
0.000 & -9.720 & 0.000 & 0.128 & 0.000 & 0.003 & -0.577 & 0.990 & 0.000 & 11.463 \\
9.720 & -0.011 & 0.000 & 0.007 & -0.000 & 0.000 & 0.017 & 0.105 & 0.000 & 1.634 \\
-0.081 & -1.325 & 0.000 & 0.004 & 0.000 & -0.000 & 0.031 & -0.062 & 0.000 & 196.180 \\
0.000 & 0.000 & 0.000 & 0.089 & 0.000 & -0.000 & -2.019 & 1.717 & 0.038 & -13.664 \\
0.000 & 0.000 & 0.000 & -0.035 & 0.000 & -0.001 & 0.266 & -0.017 & -0.000 & 3.773 \\
0.000 & 0.000 & 0.000 & 0.014 & 0.000 & -0.000 & -0.334 & 0.294 & 0.083 & -5.477 \\
0.000 & 0.000 & 0.000 & -0.000 & 0.000 & 0.000 & 0.000 & 0.000 & 0.000 & -3.260
\end{bmatrix}$$

$$
B = \begin{bmatrix}
0.000 & 0.000 & 0.000 & 0.000 & 0.000 & 0.000 & 0.000 \\
0.000 & 0.000 & 0.000 & 0.000 & 0.000 & 0.000 & 0.000 \\
0.000 & 0.000 & 0.000 & 0.000 & 0.000 & 0.000 & 0.000 \\
-7.015 & 9.720 & -0.004 & 11.870 & 11.870 & 0.000 & 0.000 \\
-1.089 & 0.000 & 9.734 & 0.000 & 0.000 & 0.000 & 0.000 \\
-130.787 & -0.521 & -0.081 & 0.000 & 0.000 & 0.000 & 0.000 \\
9.896 & 0.102 & 57.173 & 3.169 & -3.169 & 0.000 & 0.000 \\
-2.793 & -15.232 & -0.002 & -5.251 & -5.251 & 0.000 & 0.000 \\
5.359 & 0.170 & 9.206 & 6.881 & -6.881 & 0.000 & 0.000 \\
0.758 & 0.000 & 0.000 & 0.000 & 0.000 & 0.000 & 0.000
\end{bmatrix}
$$

Low speed: u = 50kts

$$
A = \begin{bmatrix}
0.000 & 0.000 & 0.000 & 0.000 & 0.000 & 0.000 & 1.000 & -0.002 & 0.116 & 0.000 \\
0.000 & 0.000 & 0.000 & 0.000 & 0.000 & 0.000 & 0.000 & 1.000 & 0.015 & 0.000 \\
0.000 & 0.000 & 0.000 & 0.000 & 0.000 & 0.000 & 0.000 & -0.015 & 1.007 & 0.000 \\
0.000 & -9.744 & 0.000 & 0.148 & 0.000 & -0.553 & -0.594 & 1.048 & 0.000 & -171.760 \\
9.743 & 0.017 & 0.000 & 0.011 & -0.006 & 0.066 & 0.122 & 0.069 & -25.669 & -16.102 \\
0.150 & -1.135 & 0.000 & -0.026 & 0.000 & -0.864 & -0.220 & 25.626 & 0.000 & 198.847 \\
0.000 & 0.000 & 0.000 & 0.082 & 53.933 & 0.041 & -1.561 & 1.691 & 0.890 & -10.079 \\
0.000 & 0.000 & 0.000 & -0.038 & 0.000 & 21.691 & 0.261 & -0.287 & -0.000 & 98.204 \\
0.000 & 0.000 & 0.000 & 0.010 & 117.272 & 0.011 & -0.424 & 0.315 & 0.983 & -2.629 \\
0.000 & 0.000 & 0.000 & -0.002 & 0.000 & 0.004 & 0.001 & 0.000 & 0.000 & -3.467
\end{bmatrix}
$$

$$
B = \begin{bmatrix}
0.000 & 0.000 & 0.000 & 0.000 & 0.000 & 0.000 & 0.000 \\
0.000 & 0.000 & 0.000 & 0.000 & 0.000 & 0.000 & 0.000 \\
0.000 & 0.000 & 0.000 & 0.000 & 0.000 & 0.000 & 0.000 \\
-15.273 & 5.962 & 0.001 & 64.907 & 64.907 & 0.000 & 0.000 \\
3.213 & 1.708 & 8.421 & 0.000 & 0.000 & 0.000 & 0.004 \\
-132.345 & -21.539 & 0.016 & 0.000 & 0.000 & 0.015 & 0.000 \\
20.988 & 1.173 & 59.126 & 41.592 & -41.592 & 0.000 & 0.033 \\
-0.662 & -16.252 & 0.001 & -28.715 & -28.715 & 0.031 & 0.000 \\
5.523 & 0.427 & 9.521 & 90.303 & -90.303 & 0.000 & -0.007 \\
0.767 & 0.108 & 0.000 & 0.000 & 0.000 & 0.000 & 0.000
\end{bmatrix}
$$

High speed: u = 50kts

$$
\mathbf{A} = \begin{bmatrix}
0.000 & 0.000 & 0.000 & 0.000 & 0.000 & 0.000 & 1.000 & -0.087 & 0.491 & 0.000 \\
0.000 & 0.000 & 0.000 & 0.000 & 0.000 & 0.000 & 0.000 & 0.985 & 0.174 & 0.000 \\
0.000 & 0.000 & 0.000 & 0.000 & 0.000 & 0.000 & 0.000 & -0.195 & 1.100 & 0.000 \\
0.000 & -8.779 & 0.000 & -0.295 & 0.000 & -1.934 & -0.318 & 1.467 & 0.000 & -171.345 \\
8.644 & 0.763 & 0.000 & -0.004 & -0.023 & -0.012 & 0.109 & 0.190 & -102.678 & 2.976 \\
1.530 & -4.311 & 0.000 & -0.045 & 0.000 & -1.041 & -1.041 & 102.801 & 0.000 & 209.257 \\
0.000 & 0.000 & 0.000 & 0.098 & 215.731 & 0.389 & 0.581 & 1.271 & 2.079 & -94.295 \\
0.000 & 0.000 & 0.000 & 0.176 & 0.000 & 86.884 & 0.417 & -1.499 & 0.000 & 106.022 \\
0.000 & 0.000 & 0.000 & 0.005 & 469.086 & 0.037 & -0.579 & 0.245 & 0.716 & -8.994 \\
0.000 & 0.000 & 0.000 & -0.000 & 0.000 & 0.005 & 0.006 & 0.000 & 0.000 & -9.631
\end{bmatrix}
$$

$$
\mathbf{B} = \begin{bmatrix}
0.000 & 0.000 & 0.000 & 0.000 & 0.000 & 0.000 & 0.000 \\
0.000 & 0.000 & 0.000 & 0.000 & 0.000 & 0.000 & 0.000 \\
0.000 & 0.000 & 0.000 & 0.000 & 0.000 & 0.000 & 0.000 \\
-23.484 & -11.795 & 0.008 & 64.885 & 64.885 & 0.000 & 0.000 \\
-21.351 & -1.259 & -1.899 & 0.000 & 0.000 & 0.000 & 0.069 \\
-163.369 & -82.936 & 0.077 & 0.000 & 0.000 & -0.046 & 0.000 \\
110.593 & 39.984 & 74.353 & 41.578 & -41.578 & 0.000 & 0.524 \\
14.316 & -16.207 & 0.003 & -28.705 & -28.705 & -0.093 & 0.000 \\
11.669 & 3.782 & 11.973 & 90.273 & -90.273 & 0.000 & -0.118 \\
0.962 & 0.482 & 0.000 & 0.000 & 0.000 & 0.000 & 0.000
\end{bmatrix}
$$

References

[1] R. B. Lightfoot. The helicopter as a competitive transport vehicle. 5(3):3–11.

[2] Anthony Robert Southey Bramwell, David Balmford, and George Done. *Bramwell's helicopter dynamics*. Elsevier, 2001.

[3] Richard van Aalst and Marilena D Pavel. On the question of adequate modelling of steady-state rotor disc-tilt for helicopter manoeuvring flight. *European Journal of Operational Research*, pages 1–8, 2002.

[4] W Johnson. Helicopter theory, 1980.

[5] Marilena Domnica Pavel. On the necessary degrees of freedom for helicopter and windturbine low-frequency mode modeling. 2001.

[6] Marilena Pavel. Memorandum m-756: Six degrees of freedom linear model for helicopter trim and stability calculation.

[7] Alexe Marinescu and V Anghel. *Aerodinamica și dinamica elicopterului*. Editura Academiei Române, 1992.

[8] Tor A Johansen and Thor I Fossen. Control allocation—a survey. *Automatica*, 49(5):1087–1103, 2013.

[9] Wayne C Durham, John G Bolling, and Kenneth A Bordignon. Minimum drag control allocation. *Journal of Guidance, Control, and Dynamics*, 20(1):190–193, 1997.

[10] A Stolk and Coen de Visser. *Minimum drag control allocation for the Innovative Control Effector aircraft*. PhD thesis, Delft University of Technology Delft, The Netherlands, 2017.

[11] Susan A Frost, Marc Bodson, John J Burken, Christine V Jutte, Brian R Taylor, and Khanh V Trinh. Flight control with optimal control allocation incorporating structural load feedback. *Journal of Aerospace Information Systems*, 12(12):825–834, 2015.

[12] Kevin Ferguson and Douglas Thomson. Flight dynamics investigation of compound helicopter configurations. 52(1):156–167.

[13] Jean-Paul Reddinger and Farhan Gandhi. Physics-based trim optimization of an articulated slowed-rotor compound helicopter in high-speed flight. 52(6):1756–1766.

[14] Michael W. Oppenheimer, David B. Doman, and Michael A. Bolender. Control allocation for over-actuated systems. In *2006 14th Mediterranean Conference on Control and Automation*, pages 1–6. IEEE.

[15] Oscar E Sipe Jr and Norman B Gorenberg. Effect of mach number, reynolds number, and thickness ratio on the aerodynamic characteristics of naca 63a-series airfoil sections. Technical report, LOCKHEED-CALIFORNIA CO BURBANK, 1965.

[16] K. Ferguson and D. Thomson. Examining the stability derivatives of a compound helicopter. 121(1235).

[17] Kenneth Anthony Bordignon. *Constrained control allocation for systems with redundant control effectors*. Virginia Polytechnic Institute and State University, 1996.

[18] Wayne Durham, Kenneth A Bordignon, and Roger Beck. *Aircraft control allocation*. John Wiley & Sons, 2017.

[19] Carmine Varriale and Mark Voskuijl. A trim problem formulation for maximum control authority using the attainable moment set geometry. 13(1):251–266.

[20] Lauriane Lefevre, Jérôme Delva, and Vianney Nowinski. Experimental evaluation of the aerodynamic rotor/propeller interactions in hybrid compound helicopters. page 10.

[21] Lauriane Lefevre, Vianney Nowinski, Jerome Delva, and Antoine Dazin. Experimental velocity fields evaluation under the rotor/propeller interactions for high speed helicopters for different propeller positions.

II
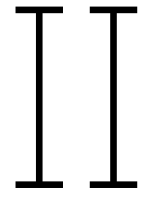
Literature Study

expanded version of AE4020 submission

1. The compound helicopter

The rotorcraft industry has been in a creative phase for decades, regarding the requirement for an increase in directional velocity. The occasional birth of design concepts sources from the need to create a faster version than its conventional counterpart. In 1960 R.B. Lightfoot created a case study in which new hypothetical aerial vehicles were compared in "The Helicopter as a Transport Vehicle" [1]. The compound helicopter was featured next to a tilt-fan, a lift-fan, and a conventional helicopter. The study was based on a 300 mile range and a 4 ton payload but the charts show the helicopter and the compound are distinctly more economical at both longer and shorter ranges. Therefore, an increase in speed, provided that efficient hover capability is maintained, would make the compound helicopter suitable for various roles and missions in both military and civil markets.

1.1. History of the compound helicopter

Lightfoot's case study sparked interest in the rotorcraft world, as multiple concepts started surfacing inside the following decade. Generally, he gave a very complete overview of how the hypothetical designs would perform with respect payload and direct operating cost (Figure 2.1), both over range in nautical miles. At greater ranges, the helicopter was either competitive with the compound, or the tilt-wing. What was realised, though, is that the compound helicopter offers a normal ferry range approximately 15% greater than any other design the considered design can perform take-off and forward flight without use of the rotor. The relationships were approximations and intended to show certain characteristic trends, but this study was interesting enough to inspire the birth of the first compound pioneers.

In 1962, one of the very first versions of a complete compound aircraft, the Piasecki 16H-1A Pathfinder II, was flight tested. It was compounded with a low wing, and a ring tail. The ring tail entailed a propeller, shroud, elevator, and rudder control surfaces. As is the general objective for compound helicopters, the design aimed towards unloading the main rotor at high speeds, to postpone retreating blade stall. The lower bound for lift share, meaning the smallest lift burden achieved for the main rotor was 46% of the gross weight. Observations like these were made in handling qualities and performance tests, conducted at the full spectrum of speeds, so from hover to 167 and 195 knots, in level flight and in dives, respectively. The aircraft, seen in Figure 1.2 had sufficient flying quality results, as the

Figure 1.1: Direct operating cost over range in nautical miles comparison [1]

controls were still very close to the conventional helicopter. The pilot was still in control primarily through the cyclic, collective sticks and pedals, and secondarily through switches for the flaperons and the tail elevator. Controllability-related challenges were more obvious, however. Although the flaperons were in place to enhance lateral motion through the cyclic, the motion seemed to have an overcompensating manner. Similarly, the ring tail assisted significantly in transition flight, among other areas, and so a forward input in the longitudinal cyclic, gave a much more abrupt response than a regular helicopter with main and tail rotor only [3].
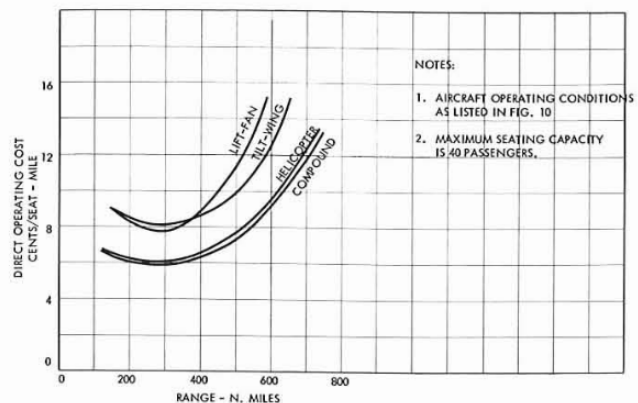
Figure 1.2: Piasecki 16H-A Pathfinder II (https://www.theaviationhistorian.com/)

Three years later, in 1965, the XH-51A Compound by Lockheed appeared in the scene, incorporating a rigid rotor system as is visible in Figure 1.3. It was also the first one to have auxiliary thrust, a design feature that has proven valuable in recent concepts, and this occurred in the form of wing-mounted turbojet engines. The objective here was to offload the main rotor entirely by 230 knots. Furthermore, the large turbojets provided additional help, relieving the rotor from any propulsive duty by 200 knots. Vibrations and blade stresses were contained by inputting a constant collective pitch setting after 150 knots[4]. Lockheed continued to remain in the forefront of the field, by later developing one of the most referenced designs in compound helicopter literature. The AH-56A Cheyenne is the vehicle present in Figure 1.4, and took maiden flight in September of 1967. It included a variable RPM hingeless rotor, stub wing, and a rear-mounted propeller[5].

Figure 1.3: XH-51A Compound

Figure 1.4: AH-56A Cheyenne

Figure 1.5: The two pioneer compound concepts by Lockheed
(https://shorturl.at/wQ139)

The attack helicopter was capable of high-level manoeuvres, as it was designed to, but showed drawbacks in handling, since the pilots experienced heavy workloads operating it within the Flight Envelope. According to Johnson's report of 1972 in the American Defence Technical Information Center, the aircraft underwent 49 test flights, and a total of 42.2 flight hours of performance and handing qualities testing, in order for this to be the verdict [5]. During flight dynamics testing, it showed good short- and long-period damping and stability in both longitudinal and lateral axes, after being disturbed. However, after 170 knots, there was observed large response times in longitudinal controllability. The excessive workload, combine with the loss of control during some maneuvering flight conditions, eventually led to the termination of the program, and the cancellation of the production contract in May of 1969. Nevertheless, some qualities the novel design proved intriguing enough that engineers revisited it in the seventies, with further testing and the completion of Johnson's report, that consequently led to significant advances in helicopter compounding research from 2003 to 2019 ([6–13]). Lastly, the US Army launched an Advanced Attach Helicopter program, three years after the discontinuation

of the Cheyenne. This was also due to potential seen in the aforementioned tests and the room for improvement, which proved to be a reality, especially when these gave path to the development of the Hughes AH-64 Apache soon after.

Single Main Rotor Helicopter (BO-105)   **Tandem Helicopter (CH-47D)**

Compound Helicopter (EC-X3)   **Coaxial Helicopter (Ka-32)**

Tilt-Rotor (XV-15)   **Tilt-Rotor (V-22)**

Figure 1.6: An overview of helicopter types [14]

More recently, there have been alterations based on the performance of the above, which has led to newer generations of aircraft of this identity. A few notable ones have been the X-49A hawk and the X^2 demonstrator. More importantly for this paper however, the rise of hybrid compound propeller configurations was seen, with the X^3 demonstrator, the predecessor of one of the newest designs of Airbus Helicopters, the RACER [2]. These are visible in Figure 1.7, and Figure 1.8 respectively, as well as the clear resemblance. The features that characterize the general design best, would be the anhedral, high aspect ratio wings, the absence of a tail-rotor, conventional tail and rear pusher propeller, and primarily the wing-mounted propellers. The overactuation problem, however, is also the most obvious with this design too. While a regular helicopter has the three controls of collective, longitudinal and lateral cyclic, here they become seven. On top of the classic three, there exists mean and differential propeller pitch, rudder and elevator deflection. It, lastly goes without saying, that they feature both lift and thrust compounding to enhance performance. The following two sections, make these engineering methods coherent.

Figure 1.7: X³ demonstrator

Figure 1.8: RACER

Figure 1.9: The two Airbus Helicopters generations of wing-mounted propellers.

1.2. Thrust compounding

There are two typical types of compounding known as lift and thrust compounding. Thrust compounding is the provision of auxiliary propulsive force, in order to unburden the main rotor from its propulsion duties at high speeds. It is a trait that not only improves the dynamic performance of the vehicles and allows it to expand its envelope borders, but also a trait the pilots themselves can exploit when performing maneuvers. Specifically, it is intuitive that with auxiliary propulsion, faster and more effective deceleration is possible too with reverse thrust on the propeller. An undesirable quality of the conventional helicopter is the large pitch excursions required to accelerate or decelerate the aircraft.
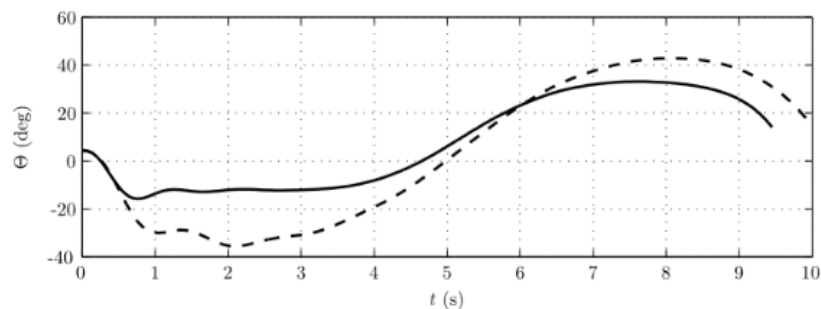
Figure 1.10: Pitch attitude in accel-decel maneuver
(Conventional helicopter: dashed, Compound helicopter: solid)[15]

Thrust compounding offers considerable maneuverability enhancement on the vehicle. Figure 1.10 demonstrates a simple accel-decel simulation by K. Ferguson. It is obvious, that the conventional helicopter (represented by the dashed line) swings more aggressively between nose-down and nose-up angles, to achieve the required maneuver. On the other hand, the coaxial-compound helicopter that features auxiliary propulsion and is represented by the solid line, not only shows smaller pitch attitude excursions required, but also completes the maneuver faster [15].

1.3. Lift compounding

The second type of common compounding methods is lift compounding, during which the objective is to relieve the main rotor from its lifting load, at high speeds. The common occurrences at large forward flight velocity of regular rotorcraft are compressibility effects on the advancing blade side and the effect of decreasing lift potential or stall at the retreating blade side.
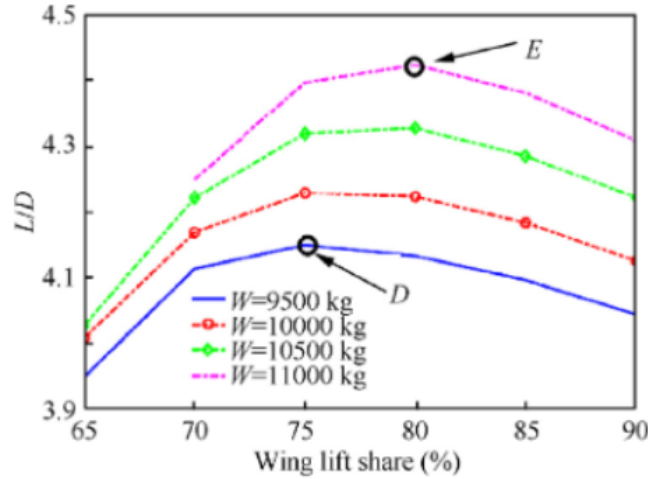
Figure 1.11: Variation of L/D for different take-off weights, V_∞ = 400km/h[16]

In 2020, Yang et al. tested the lift share by a wing on a compound helicopter and how this improves flight performance. The study began with the model of a helicopter together with a wing model and a propeller model. From that moment on, trim points were obtained for varying flight speed, main rotor speed, blade twist, rudder controls, and take-off weight, incrementally obtaining a higher wing lift share, and moving on to the next variable. Figure 1.11, shows the fifth and last trim point of the study (point E), after which, a wing lift share of 80.2% is achieved [16]. This study is a key one to understanding the importance and potential of lift-compounding in rotorcraft. Although the effects might not be as visually present in flight maneuvers such as with thrust compounding, but equally as vital for the forward flight performance of the vehicle.

2. Rotor Theory

A key challenge faced by early rotary-wing inventors was the asymmetrical velocity field experienced by the rotor during forward flight, as depicted in Figure 2.12. In hover, the incident velocities around the rotor hub were symmetrical. However, during forward flight, the advancing side experienced higher normal velocities, while the retreating side had reduced velocities, with a region of reverse flow near the hub.
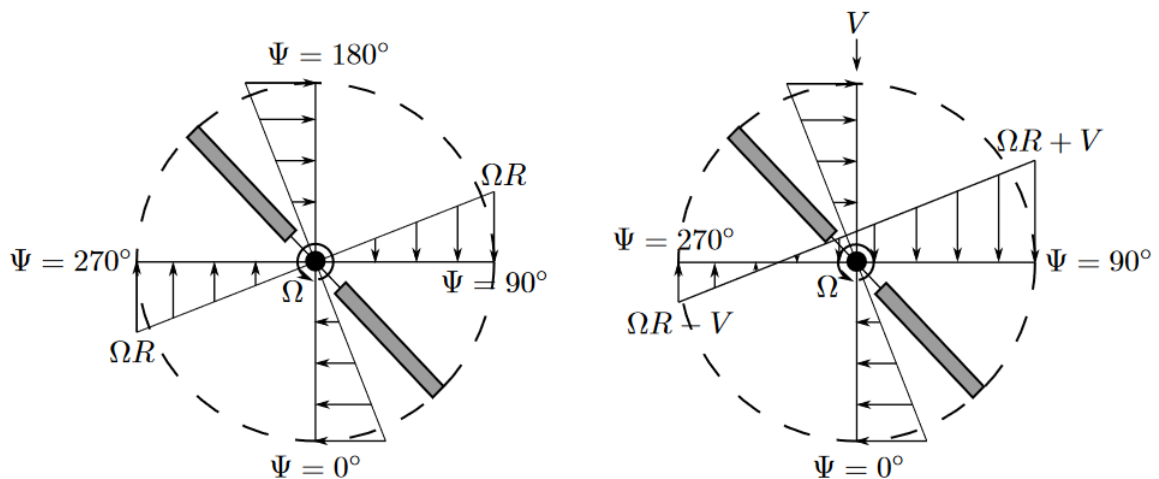
Figure 2.12: Rotor disc velocity distribution in hover (left) and forward flight (right) [17]

This asymmetry in velocities resulted in a non-uniform lift distribution, creating a roll moment in the

rotorcraft. To address this issue, Cierva introduced hinges in the blade roots, enabling flapping motion that adjusted the local angles of attack to compensate for the asymmetrical lift distribution. However, the introduction of hinges also introduced another challenge—blade root lag (or lead-lag) motion—as a result of Coriolis effects during flapping. This motion caused in-plane vibration at the blade root and gave rise to the phenomenon known as ground (or air) resonance, a significant dynamic issue in rotorcraft. To mitigate this vibration, lag hinges with dampers were introduced to attenuate its frequency.

In addition to flapping and lag motion, the blades could be feathered around an axis parallel to the blade span. This feathering motion played a crucial role in providing control for the entire helicopter, allowing the pitch of the blades to be adjusted. Figure 2.13 illustrates the three fundamental blade motions along with their associated hinges. These advancements in rotor design and control mechanisms were significant milestones in the development of rotary-wing aircraft, paving the way for further innovations in the field.

2.1. Rotor types

These blade motions generate significant stresses, resulting in the transmission of large moments through the rotor hub to the helicopter. The mechanical design of these components must carefully account for the blade motions and minimize the associated loads. The selection of the blade-to-shaft connection method fundamentally classifies the rotor. Various hinge arrangements exist, including the following commonly used types [18]:

- Articulated rotor: This rotor utilizes feathering, flap, and lag hinges for blade attachment. Due to operating under high loads, these hinges require frequent maintenance. Moreover, a hinged hub can become bulky for a larger number of blades, contributing to increased helicopter drag.
- Semi-hingeless rotor: Instead of lag hinges, this rotor employs a cantilever root restraint that allows blade lag through bending at the rotor.
- Hingeless (or rigid) rotor: Feathering hinges are the only hinges present in this type, as the flap hinges are eliminated by providing blades with greater bending flexibility (soft flapwise) and using tension-torsion straps to support the centrifugal load. Hingeless rotors offer advantages such as reduced maintenance, fewer hub parts, and improved control response.
- Bearingless rotor: This rotor eliminates all hinges in the attachment mechanism. It is based on composite materials with elastomeric elements, and its development has occurred more recently.
- Teetering rotor: This specialized arrangement mounts a pair of blades as a single unit, attaching them to the rotor shaft similar to a semi-hingeless rotor.
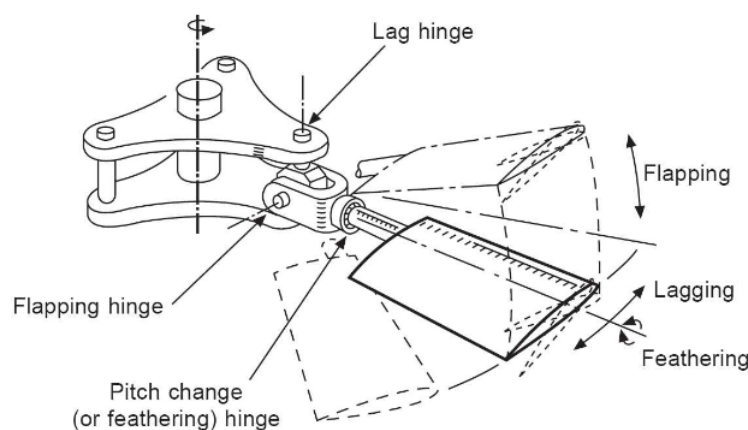
Figure 2.13: Fundamental blade motions [19]

2.2. Rotor controls

Cyclic   The cyclic pitch control is employed to manipulate the swashplate and, consequently, the tip-path plane of the rotor by introducing cyclic changes in blade pitch. As previously described, since the thrust vector is nearly perpendicular to this plane, the desired helicopter displacement can be achieved by tilting the thrust vector in the desired direction. The pilot utilizes a control stick to govern this tilt. Moving the stick forward or backward causes longitudinal tilting of the tip-path plane, resulting in the helicopter pitching the nose down or up, respectively. Similarly, moving the stick to the right or left induces lateral tilting of the tip-path plane, leading to the helicopter rolling to the right or left. It is worth noting that any combined movement can be decomposed into longitudinal and lateral components. Moreover, the cyclic stick commonly incorporates a trim switch, which, when activated, adjusts the spring tension to maintain the stick in a desired position. This feature reduces pilot workload during steady flight conditions.
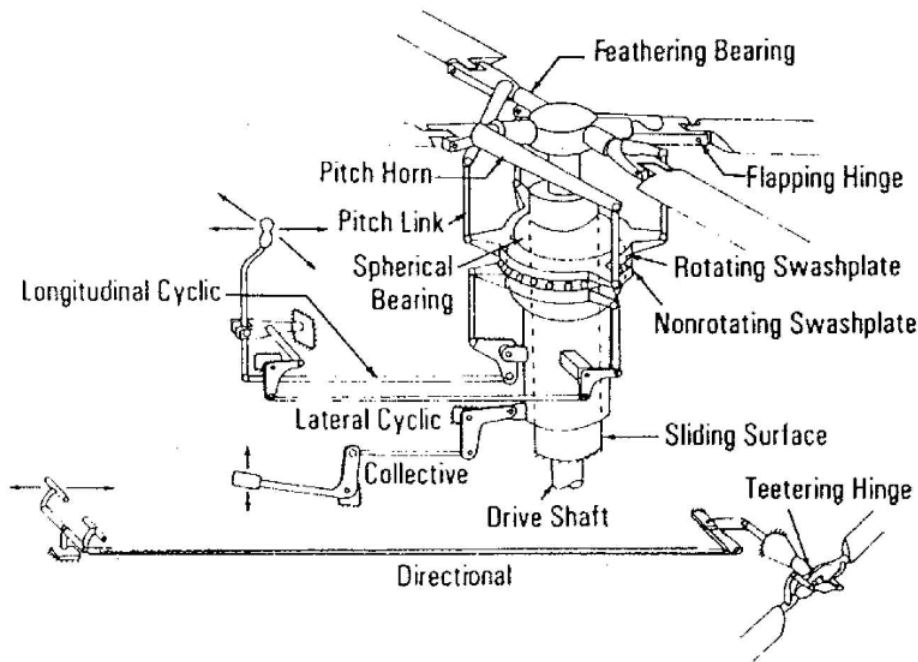
Figure 2.14: Helicopter control system scheme [20]

Collective   In addition to the cyclic control, there is a collective control that allows for simultaneous pitch adjustment of all blades. This collective control is made possible by the vertical movement of the swashplate along a sliding surface surrounding the rotor shaft. Operated by a lever positioned on the left side of the pilot, pulling this lever upward increases the pitch of the blades, resulting in greater lift generation and subsequently an increase in rotor thrust (provided the blades do not stall). Conversely, lowering the collective lever decreases the thrust produced by the rotor. This control mechanism is primarily utilized for climbing and descending maneuvers, as well as accelerating or decelerating horizontal motion of the helicopter. It is important to note that increasing the collective pitch of the blades not only generates more lift but also increases drag, leading to a drop in engine RPM. To maintain a constant RPM in this situation, additional power needs to be applied to the engine. This is achieved by simultaneously twisting the handle of the collective lever while adjusting the collective pitch.

3. Computational Modelling Methods

The unique flight dynamics of helicopters exhibit significant nonlinearity due to the complex aerodynamic interactions among the rotor, fuselage, tailplane, and any auxiliary propulsion devices. Additionally, the motion of the vehicle, its structural dynamics, and inertia must be taken into account

when studying flight dynamics modeling [21–23]. Numerous researchers have dedicated their efforts to modeling these nonlinear characteristics, resulting in a wide range of mathematical models for theoretical analysis [24–26], numerical simulation [27–30], and real-time simulation [31–35]. Various authors have also made valuable contributions to the field of helicopter mathematical modeling [36],[37],[38],[39]. There are two distinct types of non-linear mathematical models for helicopter flight dynamics. The first type utilizes differential equations to describe the non-linearity in helicopter motion. This method implicitly incorporates the linearity and nonlinearity of subsystems, such as the rotor model and dynamics of other components. It provides a relatively accurate and reliable foundation for designing the helicopter's flight control system. An example of this model is the ARMCOP model [32],[37], which is a low-order model employing a static inflow model and blade element theory to calculate rotor forces and moments in a periodic average form. In other words, this method is time-efficient and suitable for initial design and analysis procedures [40],[28].
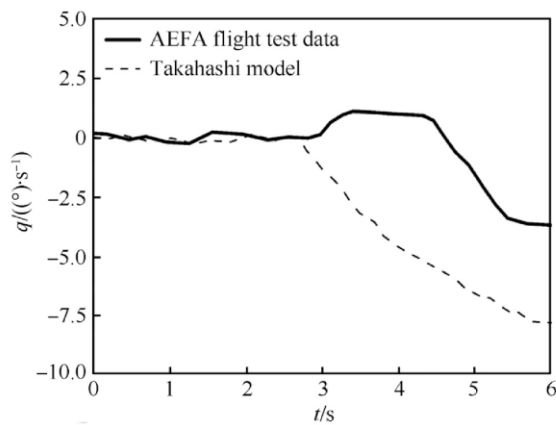
Figure 3.15: Comparison with Zhao & Curtiss model [41]
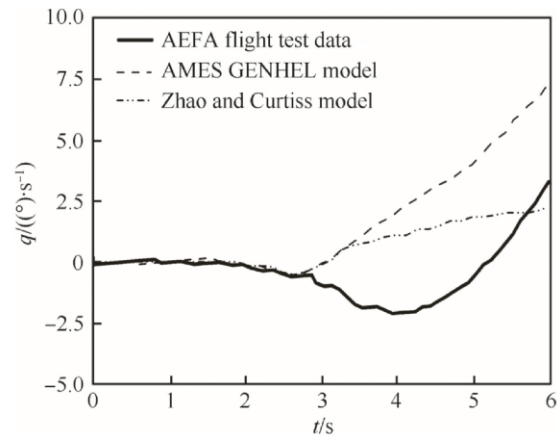
Figure 3.16: Comparison with Zhao & Curtiss model [41]

The second type of modeling technique encompasses nonlinearity not only in helicopter motion but also in every subsystem. This method is widely used for helicopter flight simulations. One typical example is the GENHEL simulation package [27] developed by Sikorsky helicopter company. While assuming the fuselage remains a rigid body, this model incorporates not only the six degrees of freedom (DOFs) related to helicopter motion but also additional DOFs for rotor motion, including flapping, lagging, torsion, and rotational motion. Empirical equations are employed to fit the torsion motion of the rotor blades. The rotor aerodynamic model combines a static non-uniform inflow model with blade element theory to calculate blade aerodynamics. It also considers rotor downwash effects on other parts of the helicopter and incorporates other aerodynamic interference effects based on experimental and theoretical analyses.

This modeling technique is well-understood in terms of accuracy and has been widely used in various studies, including ground numerical simulation [33], parallel processing investigations of nonlinear equations [34], and simplification of high-order linear models [35]. Notably, the GENHEL model also includes a representation of the engine/fuel control system, enabling the simulation of variable rotor speed strategies with higher accuracy. This feature is crucial for analyzing the flight dynamics of more advanced rotorcraft configurations. According to relevant flight test results [27],[35], the GENHEL model demonstrates relatively high precision in the mid-speed forward flight range. However, its accuracy in hover and high-speed ranges requires further improvement due to the lack of study on the rotor flow field and its aerodynamic interference on the sub-components in these flight regimes.
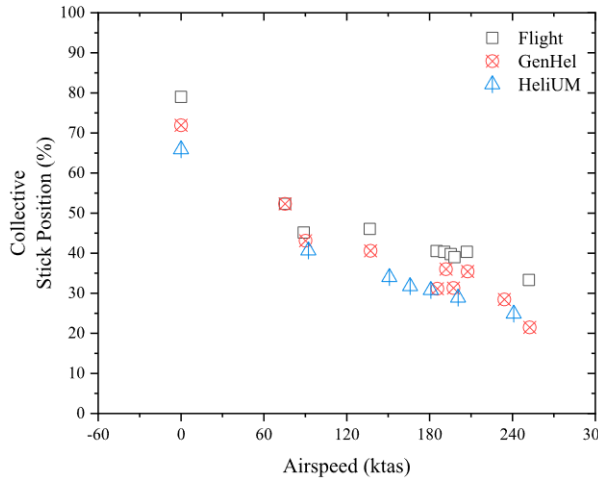
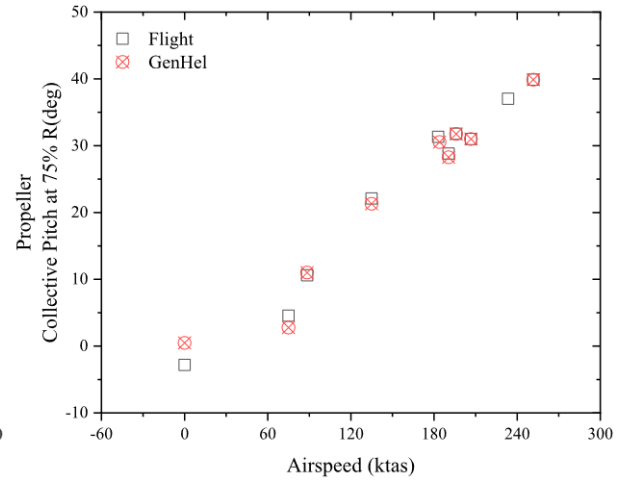**Figure 3.17:** Stick position trim of X2TD [42]

Figure 3.18: Propeller collective trim of X2TD [42]

Fegely et al. have presented the validation of flight dynamics models for coaxial compound helicopters, developed in GENHEL and HeliUM, is presented in this paper through correlation with X2TD flight test data. The article discusses the importance of validated physics-based flight dynamics models in aircraft design, highlighting their applications in load prediction, control system design, and handling qualities analysis. The paper focuses on the development and validation of two high-order mathematical models, namely the Sikorsky GenHel and HeliUM models, which have been traditionally used for single-main-rotor helicopters and are now adapted for the hingeless coaxial pusher configuration. Firstly, the study indicates that the GenHel and HeliUM X2TD models demonstrate excellent correlation with flight test data for both steady-state and dynamic responses in the piloted frequency range (up to 2 Hz), and that both models accurately predict rotor modes, with similar frequencies to each other. However, there is a slight overprediction of the regressive-lag and regressive-flap rotor modes, although the overprediction is more pronounced for the regressive-lag mode. Also, by employing a system identification approach using analytical equations of motion, a few key physical parameters were adjusted to improve the frequency response correlation across a wide range of frequencies (0.1 to 10 Hz), including both low-frequency rigid-body dynamics and high-frequency rotor dynamics. Relatively small adjustments, typically under 10 percent, were sufficient to significantly enhance the frequency response correlation of the HeliUM model with flight test data. Lastly, the pitch and roll responses of the X2TD, when evaluated against the ADS-33E pitch and roll bandwidth specification, fall within the Level 1 region, indicating satisfactory performance.

4. Rotorcraft Trim Methods
4.1. Numerical Trim Optimization

Having completed a demonstration of a solution to the redundant trim problem, the thesis moves on to asssessing how it compares to relevant studies. It should be noted that earlier, various other approaches where taken, leading to infeasible solutions, or over-simplifications. For example, initially, the parameters of the tail and elevator were fulfilling the pitching moment fully. In that case, the parameters had to be readjusted, since that would neglect the element of redundancy. In other words, the $\dot{q} = 0$ equation would have been fully satisfied by the control δ_e, the equation $\dot{w} = 0$, by ϑ_0, and the equation $\dot{u} = 0$ by the maximum amount of $\bar{\vartheta}_p$ possible, and ϑ_{1s}.

Following that, a series of attempts on numerical optimization were made, using a Matlab non-linear optimization function as well as a genetic algorithm routine to escape local optima. What proved to be problematic in that approach was the relationship between them and the mathematical model itself. Namely, the objective function along with its constraints were plotted as well, in order for effective debugging to happen where needed, and for easier visualization. What seemed to occur

were singularities due to the constraints sourcing from the EOMs. Trigonometric functions in the denominator in addition with the allowed ranges of the angles gave a line of very large values that hindered the effect of the optimization functions. Unfortunately, actions such as Taylor expansion and L'Hospital's rule did not overcome this, and so the approach taken after this was mechanics-based. Nevertheless, the benefits of a literature study that also features the modelling and trim of a 3DoF model has the significant benefit ofa much better understanding of the problem at hand.

(Sagan et al. 2021) have formulated a power optimization problem in which an over-actuated 3DoF model is constrained in conventional parameters such as accelerations, angles, rotor rotational velocities and thrust coefficients. The process is carried out via OpenMDAO, a NASA-developed optimization framework using the gradient-based Sparse Nonlinear OPTimizer (SNOPT)[43]. A combination of the already applied methods and a similar version of Sequential Quadratic Programming optimization is yet to be attempted and can produce promising results.
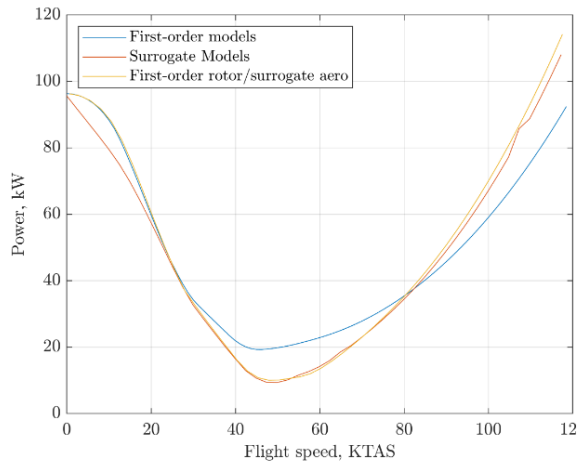
Figure 4.19: Totall shaft power required objective function in level flight [43]
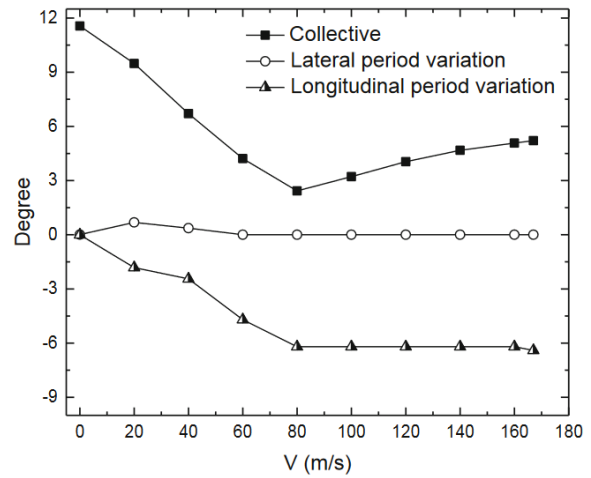
Figure 4.20: Rotor pitch controls in trim from Lin et al. [44]

Figure 4.21: Results of two optimization strategies in trim from literature

In (Lin et al. 2019), the trim strategy of a vehicle very similar to the X^3, is done by dividing the problem of manipulation redundancy in three stages, namely the hovering low speed stage, the pre-transition flight stage, and the high-speed forward flight stage. In each of these, a different set of controls are dominant, which is imposed with weighting factors. From that, it is possible to solve analytically and obtain the trim results in all flight-speed stages [44]. Essentially, a similar way has been entailed in this trim solution, with the speicfication of a transition from helicopter to airplane mode, which sets the presmise for the control allocation that has been explained.

Lastly, an effective trim analysis method has been done by Ferguson & Thomson, as well as Cao et al., focusing on trim, stability and control of a coaxial compound helicopter version. There, they eliminate control redundancy by presenting a pitch angle scheduling to the model, which provides a control setting constraint for all flight speeds that is to be limited by. Resulting from that, is a system of equations including forces, moments, flapping motion, induced velocity, and a lateral lift offset equation, that are equally as many as the unknowns, which makes it a determined system solved in Matlab ([15],[45]).

4.2. Control Allocation

When it comes to the procedure of manoeuvre simulation, the complexity varies in levels from a simple ascend-cruise-descent routine to accel-decel and pullup-pushover manoeuvres from certification documentation, to large-amplitude simulated manoeuvres to test performance at the edges of the flight envelope. Since the late 20th century, inverse simulation has been researched. Approaches to

the solution of inverse redundant problems in flight mechanics showed neither necessity for filtering nor excessive sensitivity to the initial values in all the tested cases when compared with other earlier procedures. In redundant cases, in particular, the introduction of a minimum of a performance index allows for better control and the convergence of the solution. Furthermore introducing cost functions where penalty coefficients appear can push the solution toward a terminal equilibrium state as seen in global optimization procedures. Many more authors working on nonlinear inversion techniques applied to aircraft dynamics do not use iterative methods and excessive demands for control action may begin to rise. A few investigations have been conducted on manoeuvrability characteristics of the compound helicopter so far, notably by Kevin Ferguson ([46],[47]).Possibly, a flight dynamics model can be tuned by way of empirical factors, in order to improve the accuracy in steady, small amplitude manoeuvring flight. However, the accuracy of the simulation results is still questionable due to the lack of the relevant flight test data. The verified simulation research on the large amplitude manoeuvre is mainly related to the conventional helicopter UH-60A, and in many cases, difficulties are met by authors in the applications, mainly due to, either suboptimal choice of cost function, evaluation of time-dependent sensitivity of outputs relative to controls, or laws assumed for the outputs themselves[48].

In conventional aircraft, pitch control is achieved through an elevator, roll control via ailerons, and yaw control using a rudder. However, as aircraft design progresses, there is an increasing inclusion of control effectors, some of which are unconventional. In certain cases, specific controls can exert significant influence over multiple axes. This leads to a situation where the system becomes over-actuated or redundant when there are more effectors than control axes. The control allocation problem arises, which involves the allocation, blending, or mixing of these control effectors to accomplish desired objectives. Over the years, a wide range of Control Allocation (CA) methods has been developed, catering to both linear and non-linear aerodynamic models. Extensive research on CA methods has been conducted, and a comprehensive survey can be found in [49]. These methods typically involve solving an optimization problem to determine the most effective control forces. In some CA formulations, the primary objective is to minimize the disparity between the desired control forces and the achieved forces, as depicted in Equation II.1. However, other methods go beyond this and aim to optimize additional parameters, such as the displacement of total effectors, trim drag ([50],[51]), or structural loads [52]. By considering these secondary parameters, these advanced CA approaches offer the potential for further performance enhancements and operational efficiency.

$$\min_{\delta} \mathcal{G} = \|\Delta C_F - B\delta\| \tag{II.1}$$

The control allocation problem is complex due to the challenges posed by over-actuation and the coupling effects of control surface actions. Determining an appropriate method to translate a flight control command into a control surface command becomes difficult. Additionally, the rate and position limits of the control surfaces must be taken into account to ensure a realistic solution. It is not only critical to effectively mix the control surface effects but also crucial to enable the aircraft to recover from off-nominal conditions, including the failure of a control surface, when physically feasible. In reconfigurable control systems, a control allocation algorithm is necessary to automatically distribute control power requests among numerous control effectors while adhering to the rate and position limits of the actuators. Furthermore, this algorithm has the potential to facilitate recovery from off-nominal conditions.

5. Control & Manoeuvre Simulation

In the context of advanced helicopter configurations, it is vital that the results be in coherence with validation data in performance evaluation of the vehicle in design. Both handling qualities and manoeuvre simulation related research provides virtual representation on what such a dynamic model displays in realistic conditions. This chapter outlines how a pilot's performance with the available inputs, translates to the outputs of the system, as well as various methods that are able to map the inputs to output desired manoeuvre laws, specifically regarding redundant aircraft designs.

5.1. Pilot control

Looking back at the beginning of section 4, one notices the control vector from Equation III.14 which is the set of ways that forces and moments can be imposed on the mechanics of the vehicle in order for it to be able to either achieve equilibrium or follow a desired trajectory. But how does the pilot exert these controls?Having additional handles for a pilot significantly reduces performance and increases the risk of misjudgement mid-flight. In the compound helicopter of this study, it is important that the set of pilot inputs are almost identical to the baseline helicopter. By almost identical, it is meant that the pilot again inputs longitudinal cyclic and collective pitch to the helicopter, but now also applies the elevator input at one moment, that is during the transition to airplane mode at around 150 knots. For the rest, control allocation is automatically applied by means of weighting function.
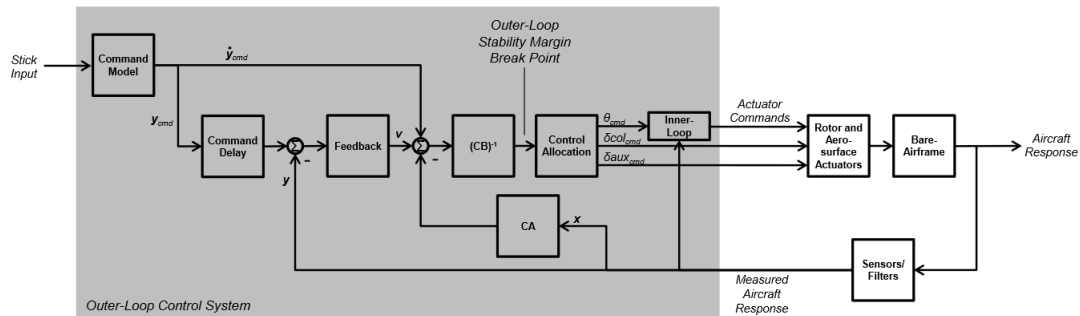
Figure 5.22: Outerloop control system representation [53]

In (Horn et al. 2020) developed a full-flight envelope outer-loop control system for a tiltrotor and a coaxial-pusher helicopter. Figure 5.22, the outer loop can be seen from the stick input to the actuator command, and the measured aircraft response feedback. In the controller, a Moore-Penrose pseudoinverse operation is used, but also incorporating weighting factors to enhance importance of some actuators over others, like it is aimed in this study.

$$\underline{u}_{des} = W^{-1}G^T(GW^{-1}G^T) + \underline{v} \tag{II.2}$$

The weight matrix W includes the weights w_i for the individual actuators. The study chose a weighting matrix $\mathbf{W} = \text{diag}\{1, 20, 1\}$, particularly for the coaxial pusher helicopter, with the purpos of fading out collective input at the minimum power required speed [53].
Similarly, O. Harkegard proposed a weighted least squares method for control allocation, which is summarised by Equation II.3.

$$u_w = \arg \min_{\underline{u} \le u \le \bar{u}} \gamma ||W_v(Gu - v)||^2 + ||W_u(u - u_p)||^2 \tag{II.3}$$

Effectively, this equation penalizes control performance, and actuator usage. The first term of the two evaluates if the computed actuator input u matches the virtual control v. For prioritization of axes to control over others, the weighting matrix W_u is enforced. In this particular case, it has been shown in Table 4.1 that the longitudinal cyclic is present in two equations in the longitudinal model. What would be preferably imposed, is the priority of the pitch axis over the x-axis. The reason is that at higher speeds, the pitching moment will have demand for both the elevator and the longitudinal cyclic. On the other hand, the primary control in the horizontal acceleration will be the auxiliary thrust of the propellers, like explained earlier in the trim process.

Regarding the second term, the objective function of Equation II.3 penalizes the position u of an actuator, away from a position u_p. This is a useful feature, particularly in the case of the elevator of the vehicle in this study, and the effect of an its deflection on the total increase in drag. In the end, the last factor in the function is the weight γ, which prioritizes the first term over the second, since the virtual control input should be matches at first, before the preferred position u_p is targeted. Overall, the aforementioned methods of control allocation have proved highly effective in literature, and provide an applicable solution to assisting an operator of an over-actuated aircraft in controlling it.

6. Research Scope

In this thesis, the search for literature has produced some promising questions, that give a direction for the entire project. A pair of identified knowledge gaps will introduce the research objectives, which in turn will be broken down to a set of research questions for better comprehension.

6.1. Knowledge gap

The literature study that this report concerns, begun with a very general idea of a flight dynamics modelling related interest for compound rotorcraft. Firstly, the last part of this idea in itself is a tree of different directions. As this report has expressed, the compounding of a conventional helicopter is a collection of designs that is not even fully explored yet. With every combination of auxiliary lift and propulsion that is possible, new concepts are being created constantly. After a specific design type was decided on, based on the quantity of related literature, the modelling process was research, a step that brought forth the first identified knowledge gap:

Among all analyses and research of compound helicopter configurations, there is no clear direction for compounding a conventional helicopter Matlab model with auxiliary propulsion and lift in its dynamics

Furthermore, it is paramount that the created model be exploited for trim and control purposes. Given that the part of development of an aerial vehicle is one of the very first ones here, the mathematical model uses approximate values for the required computational purposes to follow. The controls of the compound helicopter in focus become significantly more, with respect to the three ones of its conventional counterpart, and so the next knowledge gap is rather easily identified:

There are 7 controls in a hybrid compound helicopter, for 6 degrees of freedom. There needs to be an optimal way to allocate control between the redundant inputs.

With the above two primary concerns of this research, it now becomes more clear to see how the process can move forward, by generating some fundamental objectives to be pursued in this research project, in order to end up in some valuable observations are results that will be further utilised in the future.

6.2. Research Objective

The two knowledge gaps are goals that are bridged with multiple steps in the research process. Specifically, between creating a mathematical model and controlling it, there exist steps involving trim, flight envelope development and more. The following three objectives generalize the entire timeline that sources from the aforementioned gaps.

Develop a 6 Degree-of-Freedom Flight Mechanics model of the hybrid compound helicopter.

The development of such a model will be in need of verification and following that, it will be able to give way to the next primary objective:

Determine the flight envelope of a conventional compound helicopter and look for a potential conversion corridor.

This is a relatively uncertain objective, as the flight envelope of a compound helicopter is a challenging one to create, and even more so, the search for a conversion corridor, to transition from hover state to forward flight. However, should these be obtained, the final and perhaps most important objective takes place:

Apply an appropriate trim strategy and discover how to allocate the controls in the vehicle.

This will answer the last knowledge gap, about which the curiosity for the research topic began. A hybrid compound helicopter certainly needs a mathematical model created for it, and approximated in terms of numerical data, but most importantly the last objective gives way to advanced control of an overactuated vehicle.

6.3. Research Questions

Finally, it comes down to a set of questions thaht need to be answered. While, the knowledge gap was identified earlier, and the objectives were stated, the simplification of the above to these questions bring clearer direction to this research. A mathematical model that will be made for a model of 6 degrees of freedom must then reach optimality in trim, but also prove stable after linearization. Once this happens, the following can be answered:

1. **What are the advantages of the compound helicopter in terms of flight envelope expansion?**
2. **Can the model be trimmed analytically? If not, what other ways provide an acceptable trim result?**
3. **Does a conversion corridor exist in the flight envelope, between the hover, and forward flight state?**
4. **What is the general way to allocate controls in an overactuated compound helicopter?**

III

Preliminary Work

1. 3-DoF flight mechanics model

In this chapter, the primary setup for the development of an aerial vehicle will be discussed. Specifically, one of the starting stages of the procedure is the mathematical model of the aircraft. The mathematical model is the basis for evaluation of flying and handling qualities, and the development of the flight control system of helicopters and other dynamical systems. In order for any trim, control, or manoeuvre simulation to happen, the model must be available for manipulation. The compound helicopter entails many different novel components that a conventional one does not, and they will shortly be visible in symbolic form too. The first step is the Equations of Motion. Specifically, the sum of forces and moments applied on a concept design lead the path for modifications that come next.

1.1. Free Body Diagram

Many adaptations of reference frames systems can be taken when breaking down a body's mechanics. It all depends on what definitions and assumptions are initially set, and if done correctly, the mathematical model should be representative of the same vehicle. Figure 1.17 displays the two FBDs used for reference for the directional forces and moments of the compound helicopter in design.
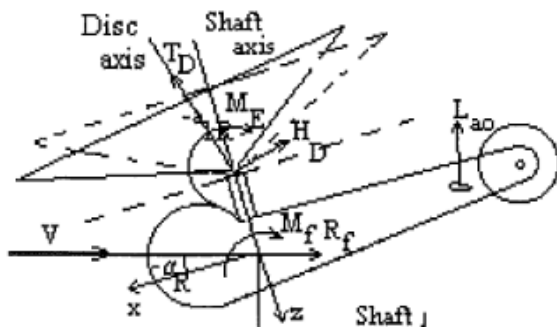
Figure 1.1: Longitudinal FBD by M. D. Pavel [54]
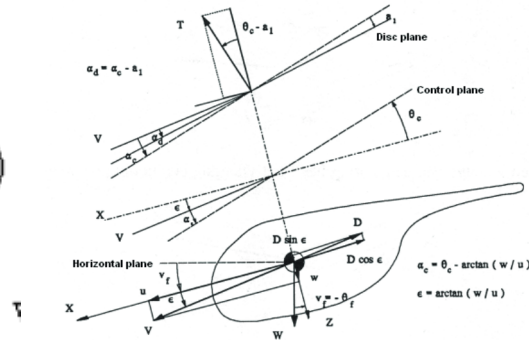
Figure 1.2: Longitudinal tail-less FBD

Figure 1.3

In flight mechanics, the crucial contributors, being forces and moments, habve to be specified, and shown in relation to each other using relevant angles. The derived FBD of the helicopter of this study can be seen below. It entails notations from literature, but primarily sources from the ones important ones to the X^3.
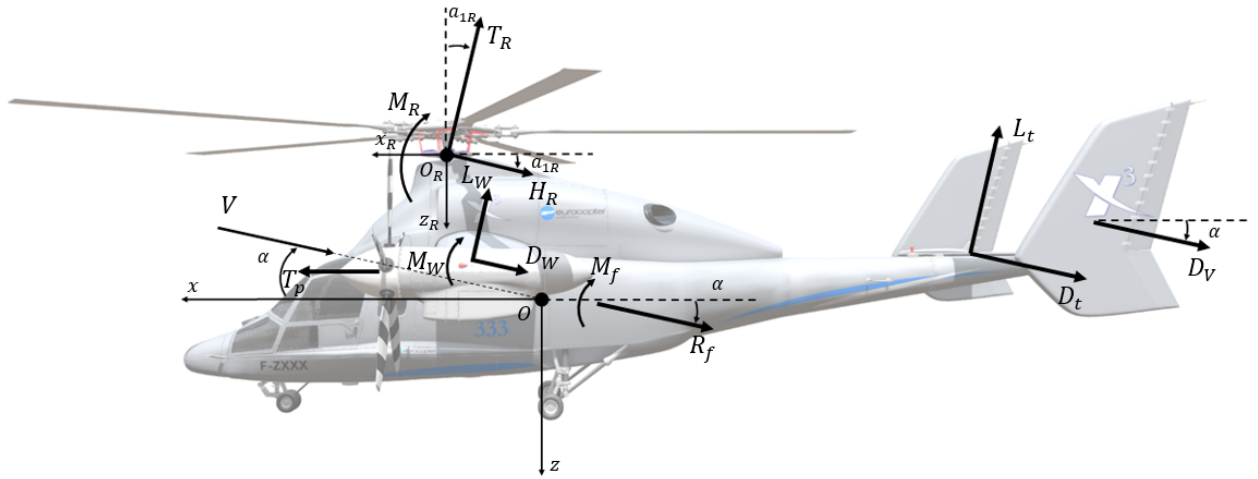
Figure 1.4: Free-body diagram port side view
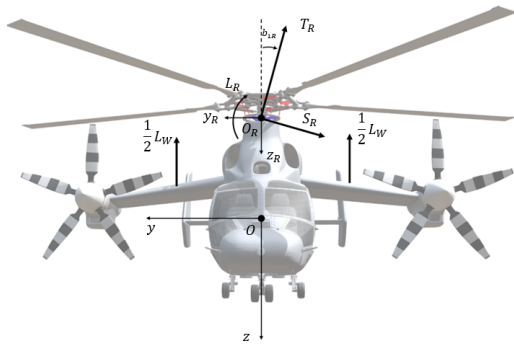
Figure 1.5: Free-body diagram front view
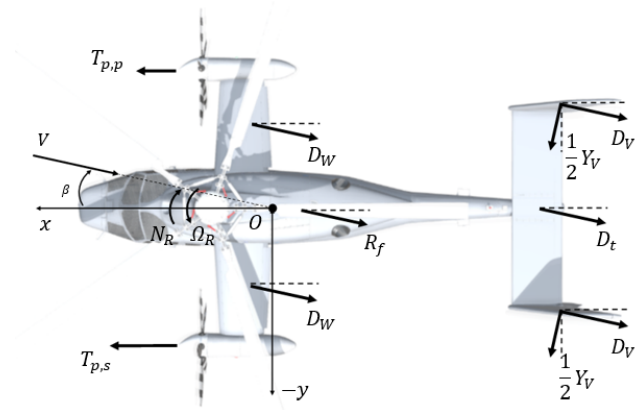
Figure 1.6: Free-body diagram top view

The drag-contributing components, are the wing, fuselage, tail and vertical fins, while the drag induced by the rotor blades is in the form o the H-force. Regarding the lift, the wing plays a large role, as has been pointed-out in subsection 1.3, and further in the following parts of the report. However, the tail-lift is assumed to not contribute to the vertical forces, but only to the pitching moments of the EOMs. Also, the auxiliary thrust of the propellers, labeled X_P is assumed to act along the x-axis, as the moment that will impose is negligible, and the pitch rate will be chosen to be evaluated later, based on only the elevator deflection and the longitudinal cyclic pitch of the main rotor.

1.2. Longitudinal EOMs formulation

The thesis objective will be the development of a 6 degree-of-freedom model of a hybrid compound helicopter, with wing-mounted propellers. This report begins with the 3 DoF one, which concerns the directional motion, namely forward and vertical translation, as well as pitch attitude. All general equations are written in the sets III.1 and III.2, with the longitudinal ones highlighted in blue .

Force equations

$$
\begin{cases}
\dot{u} = -(wq - vr) + \dfrac{X}{M} - g \cdot \sin\vartheta \\[2mm]
\dot{v} = -(ur - wp) + \dfrac{Y}{M} - g \cdot \cos\vartheta \cdot \sin\varphi \\[2mm]
\dot{w} = -(vp - uq) + \dfrac{Z}{M} - g \cdot \cos\vartheta \cdot \cos\varphi
\end{cases}
\tag{III.1}
$$

Moment equations

$$
\begin{cases}
I_{xx}\dot{p} = (I_{yy} - I_{zz})qr + I_{xz}(\dot{r} + pq) + L \\
I_{yy}\dot{q} = (I_{zz} - I_{xx})rp + I_{xz}(r^2 - p^2) + M \\
I_{xx}\dot{r} = (I_{xx} - I_{yy})pq + I_{xz}(\dot{p} - qr) + N
\end{cases}
\tag{III.2}
$$

The above sets provide a broad notation for the dynamics of any dynamic vehicle. It is the applied forces and moments that make them representative of a unique model. These, specifically are the terms **X, Y, Z, L, M, N**. The process of collapsing them to 3 equations is the equivalent of constraining the vehicle's movement in the sideways translation, roll, and yaw attitudes [55].

Forces X-axis

$$
X = -T{\cdot}\sin(a_{1R})+H+D_{tot}{\cdot}\sin\vartheta_f+L_W{\cdot}\sin\vartheta_f-W_g{\cdot}\sin\vartheta_f \approx -T{\cdot}a_{1R}+H+D_{tot}{\cdot}\sin\vartheta_f+L_W{\cdot}\sin\vartheta_f-W_g{\cdot}\sin\vartheta_f \tag{III.3}
$$

Forces Z-axis

$$
Z = -T \cdot \cos(a_{1R}) + D_{tot} \cdot \cos\vartheta_f - L_W \cdot \cos\vartheta_f + W_g \cdot \cos\vartheta \approx -T + D_{tot} \cdot \cos\vartheta_f - L_W \cdot \cos\vartheta_f + W_g \cdot \cos\vartheta_f \tag{III.4}
$$

Moments Y-axis

$$
M = -T \cdot \cos(a_{1R}) \cdot h_R + L_W \cdot \cos\vartheta_f \cdot d_W - L_T \cdot \cos\vartheta_f d_T \approx -T \cdot h_R + L_W \cdot \cos\vartheta_f \cdot d_W - L_T \cdot \cos\vartheta_f d_T \tag{III.5}
$$

Equations III.3, III.4 and III.5 specify the contributions of the different subsystems of the compound vehicle to the forces in the X and Z direction, as well as to the pitching moment equations. The small angle approximation is implemented for the numerical calculation for the angle a_{1R}. Note that it is not applied. Now the focus extends to the force variables. The thrusts of the main rotor and propeller are modelled to follow the conventional thrust formulas, shown in Equation III.6 and Equation III.6. Furthermore, the lift and drag are visible in relations III.8, III.9 and III.10.

$$
T = C_T \cdot \rho \cdot \Omega^2 R^2 A \tag{III.6}
$$
$$
X_P = T_P = C_{TP} \cdot \rho \cdot \Omega_P{}^2 R_P{}^2 A_P \tag{III.7}
$$
$$
L = \frac{1}{2} \cdot C_L \cdot \rho \cdot V^2 S \tag{III.8}
$$
$$
L_T = \frac{1}{2} \cdot C_{LT} \cdot \rho \cdot V^2 S_T \tag{III.9}
$$
$$
D = \frac{1}{2} \cdot C_D \cdot \rho \cdot V^2 A_{eq} \tag{III.10}
$$

Regarding the flapping dynamics of the main rotor, the three key angles can be seen below in Figure 1.7. The flapping dynamics problem is solved by way of Taylor expansion. In studies of accuracy like the one here, it is acceptable that the first order coefficients are taken as approximation of the solution.
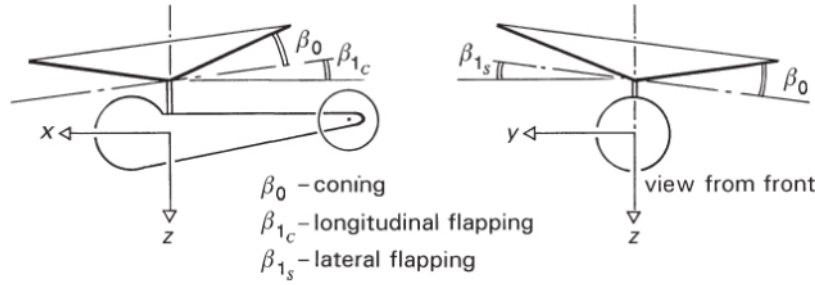
Figure 1.7: Flapping angles (In this report they are labeled a_0, a_1, and b_1 respectively)

The first order approximation of the solution is given by Equation III.11 of the quasi-steady-state flapping rotor motion.

$$\beta = a_0 - a_1 \cdot \cos\psi - b_1 \cdot \sin\psi \qquad\qquad \text{(III.11)}$$

For now, this report only concerns the longitudinal model, so the relations for a_0 and a_1 are given by:

$$a_0 = \frac{\gamma}{8}\left((1+\mu^2)\vartheta_0 + \frac{4\lambda}{3}\right) \qquad \text{(III.12)} \qquad\qquad a_1 = \frac{2\mu(\frac{4\vartheta_0}{3}+\lambda)}{1-\mu^2/2} \qquad \text{(III.13)}$$

The above representations are then substituted by numerical values from literature and the iterative process of solving for the four controls ϑ_{1s}, ϑ_0, $\bar{\vartheta}_p$ and δ_e in trim occurs.

1.3. Trim process

Past the procedure of the mathematical model formulation, the trim of the vehicle takes place. Depending on the model in design, different trim strategies are applicable. The corresponding aircraft, being a version of the experimental Eurocopter X^3, is an overactuated one, meaning there are multiple control inputs available per desired manoeuvre. The vector **U** of the controls is described in Equation III.14. These are representative of the rotor collective and cyclic pitch, mean propeller pitch, and elevator deflection, respectively. Concerning the third control variable, the pitch is not going to be equal for the portside propeller and the starboard one. In this longitudinal model, only the mean propeller pitch is used, for forward thrust and pitch moment contribution, where as an additional control variable of the differential propeller pitch ϑ_{diff} will be part of the vector, and will contribute to yaw control and compensation of the main rotor rotational velocity.

$$\mathbf{U} = [\vartheta_0, \vartheta_{1s}, \bar{\vartheta}_p, \delta_e]^{\mathrm{T}} \qquad\qquad \text{(III.14)}$$

It is noticeable, that there are 4 controls that make up the above vector, for a model of 3 degrees of freedom. For at least one the accelerations $\dot{u}, \dot{w}$ or $\dot{q}$, there are more than one inputs available. An overactuated problem in dynamics is translates to an overdetermined sytem of more unknowns than equations in mathematics. As a result, the trim solution is not the conventional analytical one, but it is an example of problems where trim optimization needs to take place. There are multiple paths to a result here, which are explored and talked about in this chapter.

Trim in control redundancy has a generalized core procedure presented by the workflow scheme of Figure 1.8, which is adjusted for the specific circumstances of the trim problem from this base version. It is vital that the objective function chosen is an effective one, as it will ultimately be the one that selects resulting values in the optimization operation. This is why the workflow diagram shows a small loop

between that and the lower box. At every attempt, the objective function should be evaluated based on the equations in place and vice versa. The Initial value block represents the conditions for which the optimization algorithm gives a numerical trim vector that is then to be inserted to the equations block. Lastly, the trim calculation is the one that displays all the trim results and plots in this report. The judgement of the complete start-to-end procedure by the engineer is based upon these plots, after which tuning of the blocks in the lead-up might be needed.
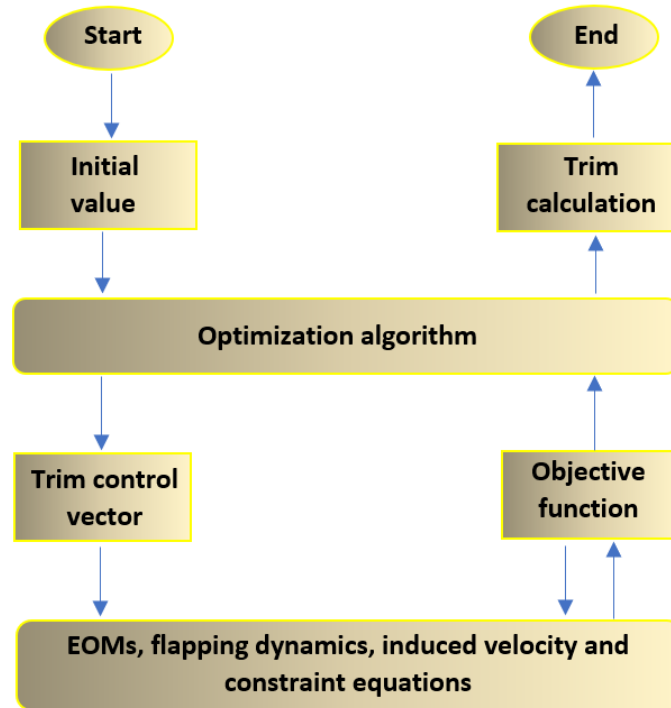
Figure 1.8: Trim process adapted from Wang et al. [56]

As it will be shown later, study of relevant literature has shown different approaches to resolving control redundancy. Criteria for optimality vary over the research in trim optimization. In the vehicle of this project, control allocation is the method for trimming the compound aircraft. That is, the controls available to the pilot for longitudinal motion are effectively distributed so that the trim requirement is satisfied.
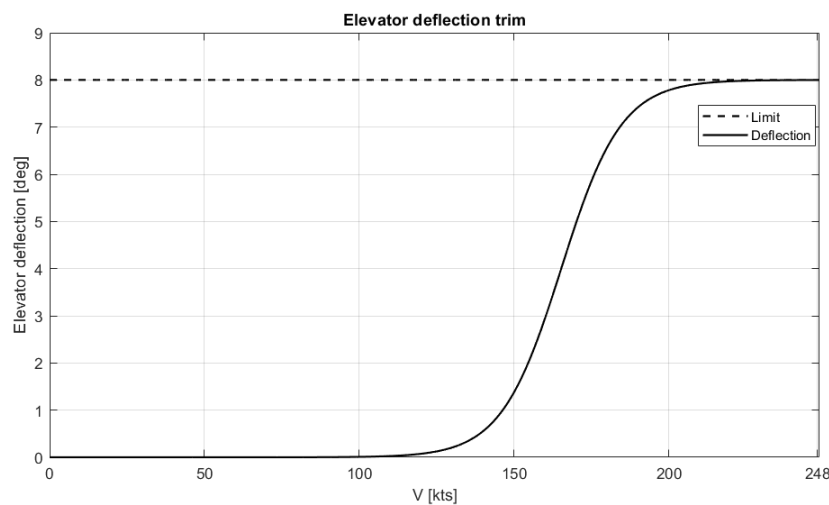
Figure 1.9: Trim plot of elevator deflection

It all begins here with the elevator deflection. While the actuator is capable of relieving the rotor in all airspeeds, it is more valuable that it is applied at around 150 knots, where the aircraft is essentially transitioning from helicopter mode to airplane mode. As mentioned, the general idea of the experimental vehicle is to offload the main rotor, so that higher cruise speeds are reached, without compressibility effects on the advancing blade and stalling of the retreating blade occur. In the longitudinal plane, the main rotor has three duties, based on the three Equations of Motion, namely, the vertical force, horizontal force, and pitching moment duties. This is whats sets the computational base, in the control allocation problem. Initially the elevator was chosen to be saturated, and compensate as much of the moment requirement as possible. Based on the chosen elevator parameters from literature, the limits are set to [-8°, 8°]. The model derived earlier with the empirical numerical parameters gives a pitching moment requirement that varies with speed as viewed by the top line of Figure 1.10. At lower airspeeds the initial allocation of elevator actuation was both inefficient and unrealistic for a compound helicopter. Hence, a logistic-shaped step to saturation was applied and shown in Figure 1.9

As a result, the elevator provides the moment compensation visualised by the lower curve of Figure 1.10. As this does not complete the full requirement, the remainder negative pitching moment is caused by the main rotor, as plotted by the lower yellow curve of the same plot. Overall, the positive aerodynamic pitching moment caused, is compensated primarily by the elevator, to the maximum of its capabilities and secondarily by the longitudinal cyclic input of the main rotor. For verification, the resultant is shown to be zero for all airspeeds.
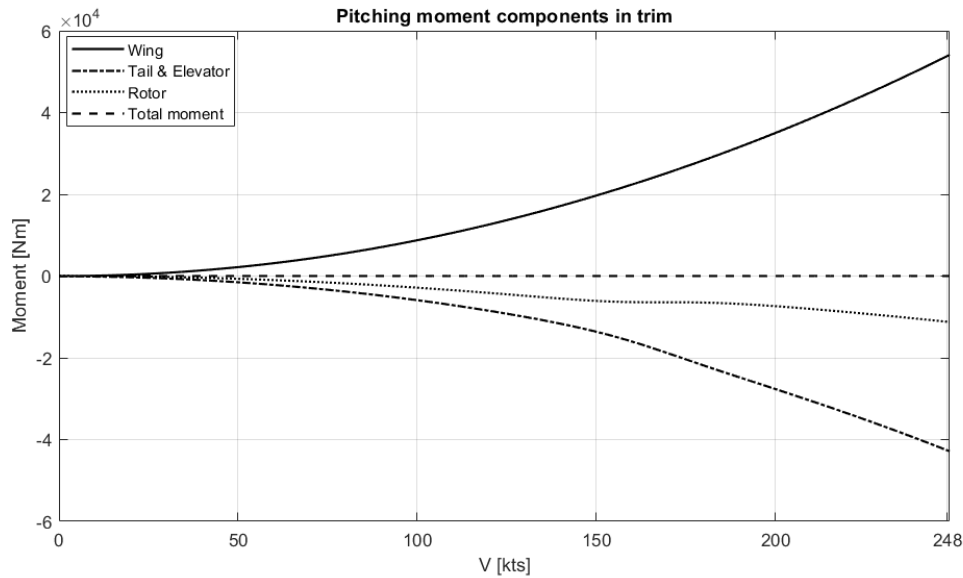
Figure 1.10: Pitching moment components in trim

Having fulfilled the trim condition in the pitch rate equation of the EOMs, the trim process moves on to horizontal force equilibrium. Further manipulation is required here, as the force output provided by the rotor is not within limits, but a specific one at every airspeed, so that the vehicle remains in equilibrium. It must be noted that there will exist a different horizontal force component required of the rotor to counteract the pitching moment, and a different one to match the total drag and H-force. Table **??** outlines the trim problem in the longitudinal degrees of freedom for the helicopter. As indicated by red, the accelerations $\dot{u}$ and $\dot{q}$ are coupled by the longitudinal cyclic input. Since we have the elevator deflection input already, we also have this from the $\dot{q}$ equation, and it will be the same as in the $\dot{u}$ equation because they obviously cannot be different. Therefore, we also obtain the value of the mean propeller pitch to satisfy the horizontal force balance.

Table III.1: Controls available for each acceleration of the 3DoF

Acceleration	Value in trim	Available controls	Symbols
$\dot{u}$	0	Mean propeller pitch & Longitudinal cyclic	$\bar{\vartheta}_p$ & ϑ_{1s}
$\dot{w}$	0	Collective cyclic	ϑ_0
$\dot{q}$	0	Elevator deflection & Longitudinal cyclic	δ_e & ϑ_{1s}

Following the aforementioned result, the non-dimensional thrust requirement sourcing from the mathematical model in trim is summarized in Figure 1.11. It is the next step in solving the trim problem after the elevator deflection is applied. This can be viewed by the pitching moment requirement curve, which is the remaining horizontal thrust needed by the main rotor, which, multiplied by the moment arm from the CG is going to satisfy the condition $\dot{q}$ = 0. Note the slight change in gradient at around 150 knots, which is where the elevator is applied. Furthermore, in sight of the horizontal force requirement curve, one can deduce where the mean propeller pitch trim comes in. As mentioned before, the longitudinal cyclic input at a particular airspeed cannot be different for the horizontal acceleration and the pitch rate. Hence, the difference between the two curves will be the thrust of the propellers. Final part of the main rotor trim calculation is the vertical force component, obtained through the vertical acceleration equation in the EOMs. This is another visible example of the effect of lift compounding discussed earlier, in subsection 1.3. Over the range of airspeeds, the lift of the helicopter's components is increased, and as a result, there will be reduction of the main rotor output demand in the vertical direction. Overall, as airspeed increases, so does horizontal thrust of the rotor and propellers, to counteract the increasing drag and H-force, and satisfy horizontal acceleration and pitch rate equilibrium. Conversely, the vertical thrust component is reduced due to auxiliary lift that rises in value and assists in equalling the weight.
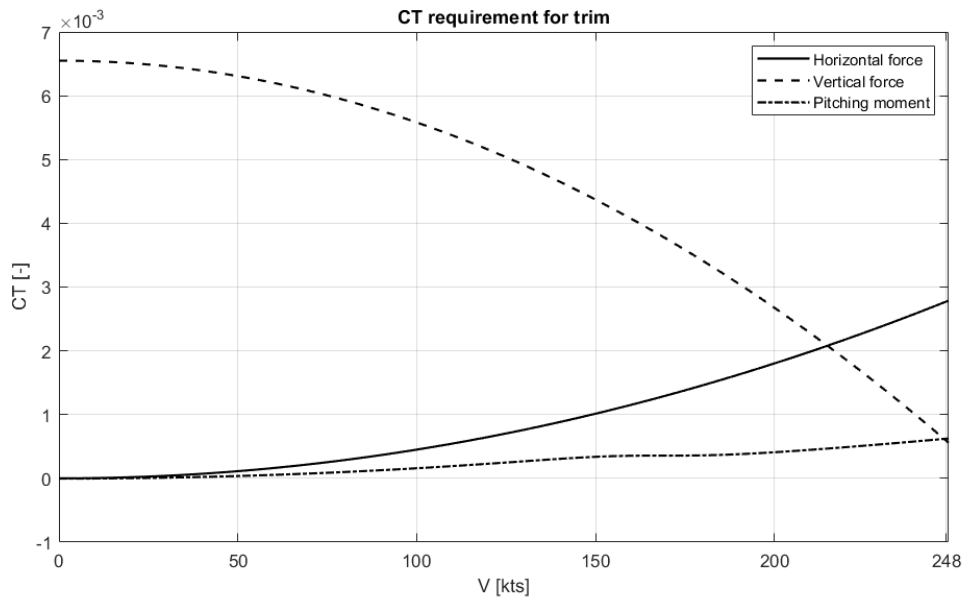
Figure 1.11: Non-dimensional thrust requirement in trim

From the thrust coefficient components of the main rotor in the two axes, one is obtained through Pythagora's theorem in Figure 1.3.

$$C_{T, \text{Rotor}} = \sqrt{C_{T,\text{vertical}}^2 + C_{T,\text{horizontal}}^2}$$

Following that, the equivalent rotor pitch trim curves can be formed from that one thrust coefficient value at every airspeed. For comparison, the trim for the given mathematical model has been done with and without the auxiliary controls. In Figure 1.12, the elevator, and propellers are fully inactive. The entire force requirement, in both longtudinal axes is fulfilled by the main rotor, where the collective cyclic reaches a value of 27.6°and the longitudinal cyclic goes up to 28.4°, both resembling experimental curves, of a conventional helicopter in trim. After applying the control allocation method described previously, the resulting trim curves for the main rotor are displayed in Figure 1.13.
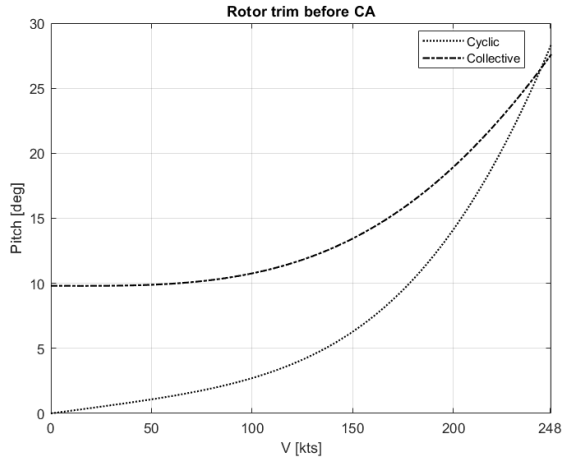
Figure 1.12: Rotor control inputs before CA
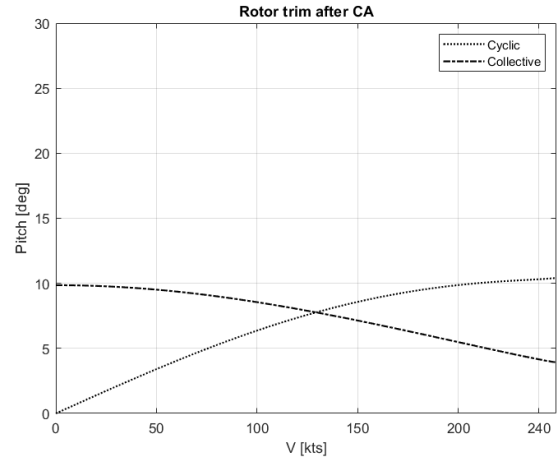
Figure 1.13: Rotor control inputs after CA

Figure 1.14: Rotor collective and longitudinal cyclic in trim

On the left-hand-side however, it easy to see a completely different formation of pitch values of the main rotor in trim. The two curves start at the same angle, which is intuitive, as there is no influence of the auxiliary controls in hover. Nevertheless, as the speed of the vehicle increases, the collective pitch is reduced instead of following a logarithmic-like trajectory. This is again due to the aforementioned reduction in need for vertical thrust, as the presence of the wing complements the rotor with auxiliary lift that increases with airspeed.
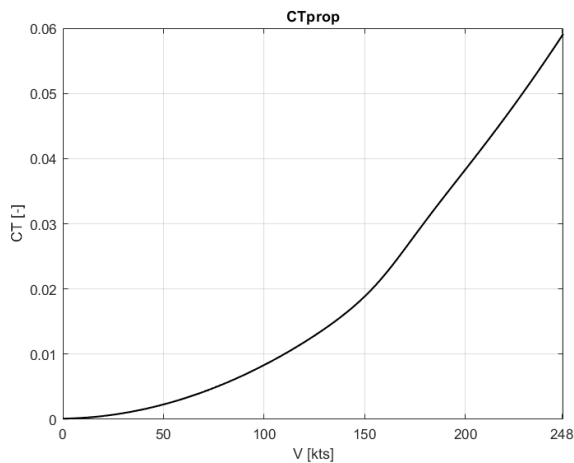
Figure 1.15
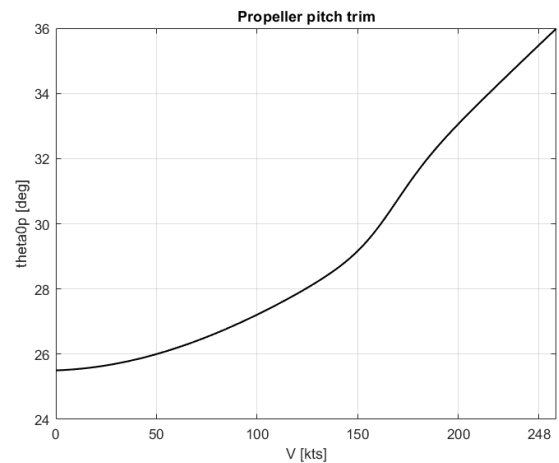
Figure 1.16

Figure 1.17: Rotor collective and longitudinal cyclic in trim

On the other hand, the longitudinal cyclic crosses over the collective curve at around 7.7°, instead of following the collective at a similar path as before. At the lower speeds, there is faster rise of the pitch value than earlier. This is because of the demand to counteract the moment of the wing. Conversely, at the higher end of the speed spectrum, the curve fattens out, because the introduction of the elevator at around 150 knots and the propeller thrust relieve the rotor from its horizontal thrust duties significantly. At 248 knots, one sees a value of around 3.9°for the collective and 10.4°for the longitudinal cyclic. In a very similar manner, the propeller needs to provide a certain thrust for the trim solution, which leads to the coefficient values of Figure 1.15. From there, the mean propeller pitch is calculated to range from 25.5°to 36°. Once again, one should note the gradient increase at around 150 knots, when the elevator is applied, which leads to a decrease in longitudinal cyclic, which leads to an increase in propeller thrust. In the end, the complete picture of all the controls of the longitudinal 3DoF model in trim can be viewed in Figure 1.18.
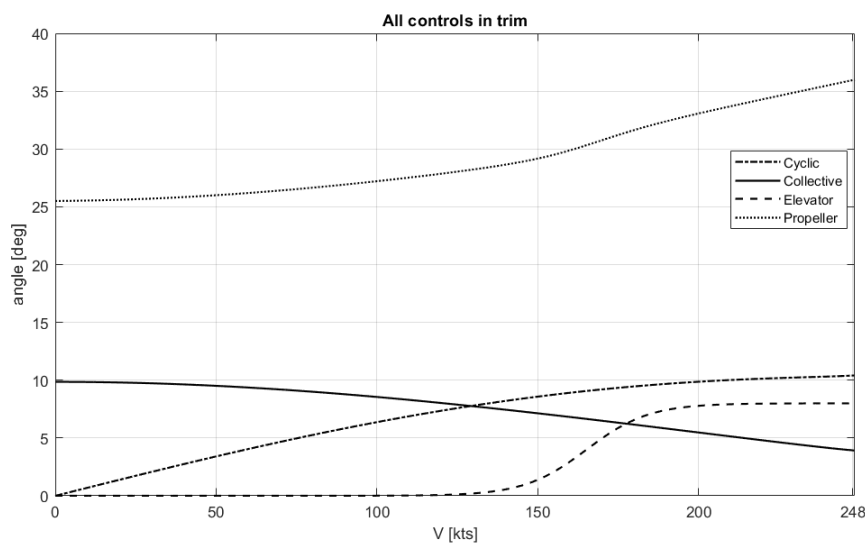
Figure 1.18: All longitudinal controls in trim

2. Mathematical modelling

Determining the appropriate level of detail required for helicopter modeling is a crucial issue in the field. While incorporating a large number of mechanical Degrees Of Freedom (DOF) related to rotor dynamics can result in a highly complex system, oversimplifying the model can lead to significant undermodelled dynamics. The key is to identify the essential effects while discarding insignificant contributions of the system dynamics within the operational range of interest. Simple helicopter models for small UAVs can be found in previous studies. Depending on the specific application, the number of DOF considered in 3-D mathematical models ranges from the basic 6-DOF body-only model to a more complex 16-DOF model, which includes detailed descriptions of rotor dynamics and nonlinear aerodynamics. The accuracy required for the model also varies based on the helicopter characteristics. For instance, while a 6-DOF model is typically sufficient to determine the natural behavior of an articulated helicopter, this approximation is no longer applicable to hingeless rotorcraft. Hingeless configurations are characterized by a rapid rotor response followed by a slower fuselage response, and the stiffness of the blades flapwise plays a significant role in this type of influence. As a result, helicopter modeling is a complex process. For the purpose of designing AFCSs to hingeless helicopters without using rotor feedback, it is concluded that the models adopted more often consist of a 6-DOF body simulation plus 3 more to account for the quasi-dynamic inflows of the rotor and propellers plus a quasi-steady or a first-order description of the rotor disc-tilt dynamics, as noted in a literature survey on helicopter simulation and modeling presented in Pavel (2001). The present research thesis focuses only on steady-state rotor disc-tilt angles for simplicity.

2.1. Derivation of the rotor model

This research thesis assumes incompressible flow and Linear aerodynamics are used to model the tails and fuselage, and the angular velocity of the main rotor is assumed constant and anticlockwise. The rotorcraft modelled in this research resembles the Eurocopter X3, a high-maneuverability compound helicopter with a hingeless rotor. The rotor hub is the most important mechanical part of a helicopter from a control perspective, as it is where the rotor blades are actuated and where all the forces and moments generated by the rotor are transferred to the fuselage. The rotor blades are attached to the rotor via hinges that allow for three possible rotations: flapping, lagging, and feathering. However, only the feathering angle can be controlled by the pilot or control system, while the other two angles are determined by the dynamics of the rotor. Hinges were first introduced by Juan de la Cierva in 1922 to compensate for the dissymmetry of lift during non-hovering flight. During hovering flight, the rotating blades experience the same apparent velocity vector at every azimuth during a full rotation. However, when the helicopter moves in a certain direction, a difference in lift between the two sides of the rotor plane builds up. Flapping hinges were installed to allow the blades on the advancing side to flap up and the blades on the retreating side to flap down in a harmonic fashion, overcoming this problem.

Rotor reference frames

As it is fundamental in all dynamics, here too the relationship between systems of reference are in need of definition. In modelling the rotor, three key systems play a role, namely the shaft plane, control plane and disc plane, perpendicular to the shaft axis, control axis, and disc axis respectively. The angular velocity vector is about the DA, and their relative rotation angles are visually represented by Figures 2.19 and 2.20.
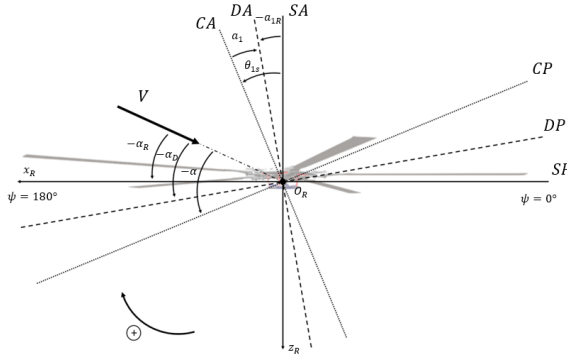
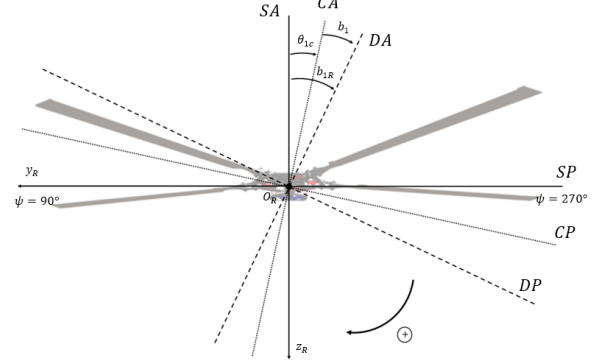**Figure 2.19:** Rotor reference systems view from port side

Figure 2.20: Rotor reference systems view from port aft

The shaft or hub plane is the one about which the equilibrium is equated, and which is also at a slight tilt angle γ_s to the body-fixed xy plane. is at . The DP is the one in which the tip-path plane of the blades is drawn, and is perpendicular to the resulting thrust. The CP is also known as no-feathering plane, meaning the one one of identical orientation to the DP if no flapping motion took place. Therefore the flapping angles explained later are measured in relation to it. In hovering flight of conventional helicopter configurations, these three coincide, however here, they compensate for other factors too, as it will be shown later.

Flapping Dynamics

The dynamics of the flaps are a significant aspect of helicopter dynamics as they contribute to rotations of the rotor disk, which in turn affects the helicopter's attitude. The individual flap angles of each blade are converted to rotor cone flap angles using a Coleman transformation, resulting in multi-blade coordinates [57].Equation III.15 provides the differential equation used to calculate the derivative of the three parameters.

$$\int_{e_\beta}^{R} dT_1 \left(r_{bl} - e_\beta\right) dr_{bl} = \int_{e_\beta}^{R} \rho_{bl} \left(r_{bl} - e_\beta\right)^2 \ddot{\beta} dr_{bl} + \int_{e_\beta}^{R} \rho_{bl} \Omega^2 r_{bl} \left(r_{bl} - e_\beta\right) \beta dr_{bl} \tag{III.15}$$

Depending on the desired simulation accuracy and the type of helicopter, one may consider setting the second and/or first derivative to zero, which calculates only the steady-state disk tilt angles. This is acceptable for trim calculations or articulated rotors where the body modes and flap modes have significant separation in time and frequency.

$$M_A = \ddot{\beta} \int_{e_\beta}^{R} \rho_{bl} \left(r_{bl} - e_\beta\right)^2 \ dr_{bl} + \Omega^2 \beta \left(\int_{e_\beta}^{R} \rho_{bl} r_{bl}^2 \ dr_{bl} - \int_{e_\beta}^{R} \rho_{bl} r_{bl} e_\beta dr_{bl} \right) =$$

$$= \ddot{\beta} \int_{e_\beta}^{R} \rho_{bl} \left(r_{bl} - e_\beta\right)^2 \ dr_{bl} + \Omega^2 \beta \left(\int_{e_\beta}^{R} \rho_{bl} \left(r_{bl} - e_\beta\right)^2 \ dr_{bl} + \int_{e_\beta}^{R} \rho_{bl} e_\beta \left(r_{bl} - e_\beta\right) dr_{bl} \right) = \tag{III.16}$$

$$= \ddot{\beta} \int_{0}^{R-e_\beta} \rho_{bl} r_{bl}^2 \ dr_{bl} + \Omega^2 \beta \left(\int_{0}^{R-e_\beta} \rho_{bl} r_{bl}^2 \ dr_{bl} + e_\beta \int_{0}^{R-e_\beta} \rho_{bl} r_{bl} \ dr_{bl} \right)$$

In the absence of lead-lag dynamics, and under the rigid blade assumption, the flapping dynamics in steady-state modes are modelled here up to and including the first harmonics of the Fourier series of the periodic motion $\beta(\Psi)$;

$$\beta(\Psi) = a_0 - a_1 \cos \Psi - b_1 \sin \Psi \tag{III.17}$$

where a_0 is the coning angle, a_1 is the longitudinal disc-tilt angle, and b_1 is the lateral disc-tilt angle. Truncation of the Fourier series sources from the fact that free motion of the blades like fast eigenmodes is not of interest but only the effect on the airframe, and that the response to control inputs is instantaneous

leading to asymptotic approximation of the flapping behaviour. As proposed by Bramwell the coefficients of Equation III.17 are expressed as follows [19];

$$a_0 = \frac{\gamma}{8}\left[\vartheta_0(1 + \mu_x^2) + \frac{4\lambda}{3} + \frac{2}{3}\mu_x\bar{p}\right]$$ (III.18)

$$a_1 = \frac{\frac{8}{3}\mu_x\vartheta_0 + 2\mu_x\lambda + \bar{p} - \frac{16}{\gamma}\bar{q}}{1 - \frac{1}{2}\mu_x^2}$$ (III.19)

$$b_1 = \frac{\frac{4}{3}\mu_x a_0 + \bar{q} - \frac{16}{\gamma}\bar{p}}{1 + \frac{1}{2}\mu_x^2}$$ (III.20)

where $\bar{q} = q/\Omega$ and $\bar{p} = p/\Omega$ are the non-dimensional pitch and roll rate respectively. It is important to list assumptions made for these simplified versions for the level of modelling fidelity of this research. For them, the flapping hinge offset is neglected ($\varepsilon = 0$), and only a first-order relationship with rates p and q is considered. Also, induced velocity is assumed uniform along the rotor disc here. To compensate for that, the model follows (Pavel, 2002) in the usual inclusion of a correction factor, expressed as in Equation III.21;

$$K_{corr} = \frac{1.33\mu_x/|\lambda|}{1.2 + \mu_x/|\lambda|}$$ (III.21)

in order to obtain the new lateral disc tilt angle of Equation III.22 [58].

$$b_1 = \frac{4\mu_x a_0/3 + \bar{q} - \frac{16}{\gamma}\bar{p}}{1 + \mu_x^2/2} + \frac{K\lambda_0}{1 + \mu_x^2/2}$$ (III.22)

As mentioned, the above takes place in the control plane, so it will be shown shortly, how these help the transition to the disc plane, and how they end up affecting the total movement of the body.

Inflow modelling

The blade element theory assumes uniform induced velocity across the rotor disc, which holds true at high forward speeds but not at low speeds when the inflow velocity at the rotor blade is comparable to other velocity components. An alternative approach, proposed by Glauert, is based on the momentum theory and treats the rotor as an actuator disc—a circular surface that can accelerate air by creating a pressure difference. This model assumes steady loading, although it allows for variation over the surface. While it is an idealized approximation of the actual rotor and has limited applicability, it is commonly used to estimate wake-induced flow. In this theory, the rotor disc is considered an actuator disc of area A and total thrust T in hover conditions. The induced velocity at the rotor disc is denoted as v0, and the wake-induced velocity infinitely far downstream is represented as vinf, where the pressure matches ambient level p0.

This approach disregards rotational energy in the wake caused by rotor torque and assumes an incompressible, inviscid fluid. Accurately modeling rotor inflow is crucial in rotorcraft dynamics, and extensive research has been conducted in this area. Understanding rotor inflow is essential for achieving simulation fidelity. Among various approaches for induced velocity, this research focuses on a quasi-dynamic inflow model. It treats the variable as an additional state in the model and dynamically varies it by equating the thrust coefficient obtained from the Blade Element Method with that resulting from Glauert's theory. Initially, a uniform inflow method was implemented in the longitudinal model during the preliminary phase of this research and early stages of complete 6-DoF modeling for the vehicle. However, assuming uniform inflow in forward and maneuvering flight led to misinterpretation of the induced velocity in the rear region of the rotor disc, resulting in overestimated blade lift in that area. Therefore, this more advanced model, considering the quasi-dynamic inflow, was adopted for applications involving piloted simulation or control-related research.

$$C_T^{Gl} = 2\lambda_0\sqrt{\left(\mu\cos\alpha_{dP}\right)^2 + \left(\mu\sin\alpha_{dP} + \lambda_0\right)^2}$$ (III.23)

Regarding the Blade Element method, it will be used later in this section to derive the overall forces. Although, its drawback is that it assumes uniform velocity over the rotor disc, which at high speeds proves valid, but but at low speeds, measurement error diverges as inflow velocity approaches the other velocity vector components acting on the blade. Using the momentum theory, Glauert analyzed the rotor as an actuator disc, of zero thickness, which assumes a steady loading, but variable across the circular surface [59]. This ideal approximation, is equivalent to an infinite-blade rotor, though gives a decent first estimate of the wake-induced flow. Using non-dimensional values μ and λ_0, for the airspeed and the induced velocity at the rotor disc respectively, the thrust coefficient according to Glauert's theory is given by Equation III.23. Equating it with the one from the Blade Element Method, and dividing by the time-constant τ_{λ_0}, provides the rate of change of inflow as shown below.

$$\dot{\lambda}_0 = \frac{1}{\tau_{\lambda_0}}(C_T^{BEM} - C_T^{Gl}) \tag{III.24}$$

In the end, the idea is that the inflow becomes dynamic, and that in steady-state condition, $\dot{\lambda}_0 \to 0$, which in turn means that, as such, the variable inflow takes place in the state vector, and in trim the zero-valued derivative is targeted like all other states. (Simplicio et al. 2013) follows the same strategy in modelling, and uses a time-constant value of 0.1, as seen in Appendix **??**.

2.2. Rotational speed reduction

Firstly, one should account for the ultimate goal, which is achieving a cruise speed range up to 255 knots, with a slowed rotor rotational velocity. Specific effect to be bypassed here, is drag divergence at the tip of the advancing blade, the fastest moving segment of the helicopter. The occurrence is the abrupt increase in drag, at certain Mach numbers. Experimentally, it has been shown that this happens between M = 0.85 and M = 0.92 [**sipe65**]. Following the modelling of Ferguson, the Mach bound to stay under, is chosen to be M = 0.89 [47]. Figure 2.21 shows the rise of the advancing blade tip Mach number, across the forward speed range of the flight envelope, but also the aforementioned Mach bound.
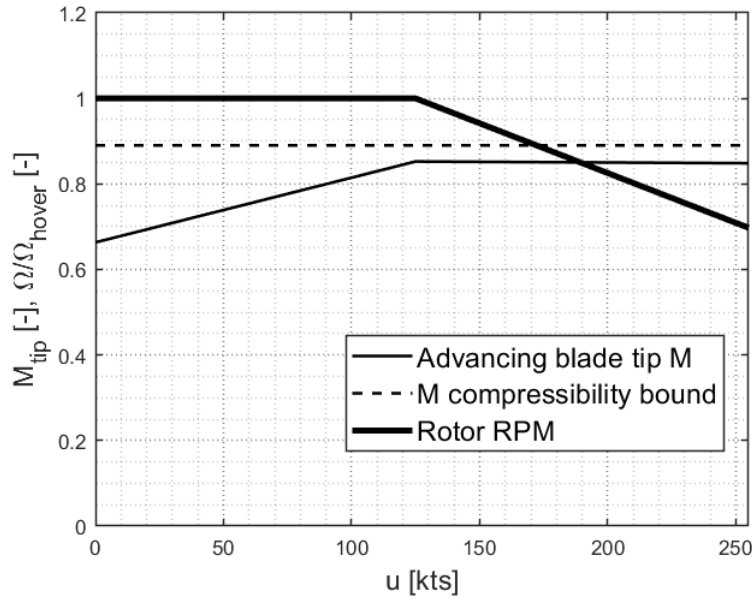
Figure 2.21: Advancing blade tip Mach number with rotor speed reduction

Ferguson's approach involves a logarithmic-like reduction of the rotor's rotational velocity, resulting in larger decreases at higher airspeeds. In order to maintain a tip Mach number of approximately 0.85, a linear reduction of the rotational velocity is implemented after reaching 125 knots. The figure illustrates the initial step of this research strategy, showcasing how the compound vehicle surpasses the

conventional helicopter's aerodynamic limitations. This achievement is made possible by incorporating auxiliary thrust mechanisms, enabling the vehicle to attain higher speeds.
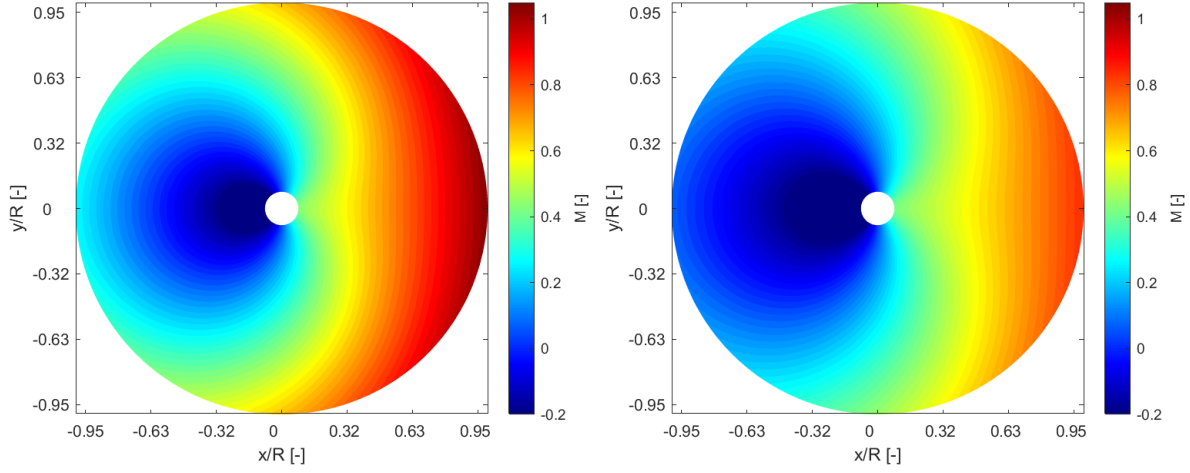
Figure 2.22: Rotor disc M at u = 255kts before RPM reduction   **Figure 2.23:** Rotor disc M at u = 255kts after RPM reduction

By linearly reducing the rotational velocity from the hover Ω at u = 125kts, the contour significantly improved overall, but especially at the advancing blade region, as Figure 2.23 shows.

2.3. Derivation of the propeller model

The propeller model follows the same calculation paths to the rotor. In this vehicle, the pair of wing-mounted propellers is not just responsible for forward thrust, like in most aircraft, but also yaw control in the absence of the conventional tail rotor, a result achieved with differential thrust. As mentioned in the assumptions of this section, the engine dynamics are not modelled. Should that have been the case, a time-delay consideration between command and output would have been applicable here. Like with the rotor, the rotational velocity of the propellers is constant, and their thrust is manipulated solely through pitch command. It must be noted here, that they are modelled such that their line of thrust does not coincide, but is parallel to the x_b-axis. As a result, the thrust sum contributes directly to the x-component of the total force. For overall modelling integrity, the inflow ratio for the propellers is also modelled under the quasi-dynamic inflow method of the rotor. The pair of the last two entries of the state vector is given by Equations III.25 and III.26.

$$\dot{\lambda}_{0pp} = \frac{1}{\tau_{\lambda_{0p}}}(C_{Tpp}^{BEM} - C_{Tpp}^{Gl}) \tag{III.25}$$

$$\dot{\lambda}_{0ps} = \frac{1}{\tau_{\lambda_{0p}}}(C_{Tps}^{BEM} - C_{Tps}^{Gl}) \tag{III.26}$$

In a configuration like the one under focus here, it is important to realise that all components operate inside the rotor's wake region. This is also true for the empennage, but for high speeds only. The effect of this observation, is an unconventional airflow near these components, and thus a strong rotr-component aerodynamic interaction. In this research, and for the level of fidelity targeted here, this is addressed in the form of interference factors. It will also be specified in the subsequent chapters but for the propellers specifically, it takes place in the equation of their advance ratio. Looking at Equation III.27, one can notice this the $K_p \Omega R \lambda_0$ factor, which negatively affects the vertical component of the velocity experienced tangentially at the propeller disc. Also, the permeability of each propeller is given by Equations III.28 and III.29.

$$\mu_{x_P} = \frac{\sqrt{v^2 - (w + K_p \Omega R \lambda_0 - q d_p)^2}}{\Omega_p R_p} \tag{III.27}$$

To further represent the adjusted airflow, both advance ratio and permeability in each propeller are affected by induced local velocities cause by attitude rates. Factors qd_p, qh_p, rs_{pp} and rs_{ps} are exactly for this, and in each instance, it is shown that a positive corresponding rate will affect the flow either positively or negatively.

$$\lambda_{pp} = \frac{u - qh_p + rs_{pp}}{\Omega_p R_p} - \lambda_{0pp} \tag{III.28}$$

$$\lambda_{ps} = \frac{u - qh_p - rs_{ps}}{\Omega_p R_p} - \lambda_{0ps} \tag{III.29}$$

Notice the opposite signs in front of the yaw rate factor in the last two equations. It is intuitive to picture the vehicle performing a non-zero yaw rate turn, and that this will cause enhanced inflow at the port side propeller, and a negative one at the starboard side propeller. This detail, together with the variable pitch inputs, are the reason the two propellers end up having the desirable differential thrust. Lastly, the induced by the forces are added with a torque cause around the y-axis, of the form, $Q_p = \rho \pi R_p^2 (\Omega_p R_p)^2 R_p C_{Q_p}$, the coefficient of which is approximated from literature. Overall, forces and moments regarding the auxiliary propellers are expressed in the body frame, and are summarized by Equation III.30.

$$\begin{cases} \vec{\mathbf{F}}_\mathbf{p} = \begin{bmatrix} T_{pp} + T_{ps} & 0 & 0 \end{bmatrix}^T = \vec{\mathbf{F}}_\mathbf{pp} + \vec{\mathbf{F}}_\mathbf{ps} \\ \vec{\mathbf{M}}_\mathbf{p} = \begin{bmatrix} 0 & Q_p & 0 \end{bmatrix}^T + \vec{\mathbf{6}}_\mathbf{pp} \times \vec{\mathbf{F}}_\mathbf{pp} + \vec{\mathbf{6}}_\mathbf{ps} \times \vec{\mathbf{F}}_\mathbf{ps} \end{cases} \tag{III.30}$$

where the last two factor are appear split because of the CG offset, and means that the moment induced around the z-axis comes after multiplying with slightly different arms $s_{pp} = s_p - s_{off}$ and $s_{ps} = s_p + s_{off}$. The sum of the two cross products in vector form equals $\begin{bmatrix} 0 & -(T_{pp} + T_{ps})h_p & T_{pp}s_{pp} - T_{ps}s_{ps} \end{bmatrix}^T$.

Table III.2: Propeller parameters

Parameter	Symbol	Value	Unit
Radius	R_p	1.2	m
Number of blades	N_p	5	-
Rotational velocity	Ω_p	305	rad/s
Blade lift curve slope	$C_{L_{\alpha p}}$	5	rad^{-1}
Equivalent blade chord	c_{ep}	0.15	m
Angle of twist	ϑ_{twp}	-9	deg
Induced flow time constant	$\tau_{\lambda_{0p}}$	0.1	s
Aerodynamic interference factor	K_p	2	s

2.4. Derivation of the wings model

As mentioned, in addition to thrust compounding, this compound helicopter configurations features lift compounding by including wings in the design. These are a set of short-span wings in high positioning and at an anhedral angle. Contrary to the real Eurocopter X^3, the model does not include aileron surfaces. Therefore, their representation in the mathematical modelling is through their aerodynamic forces and induced moment about the pitch axis. Equation III.31 outlines the lift force as follows;

$$L_w = \frac{1}{2} \rho V_w^2 S_w C_{L_w} \cos(\Gamma) \tag{III.31}$$

where Γ is the anhedral angle and the angle of attack experienced at the wing position is affected by the induced velocity factor qd_w caused in a pitch rate motion.

$$\alpha_w = \arctan\left(\frac{w + qd_w}{u}\right) + i_w - K_w \varepsilon_0 \tag{III.32}$$

As with most components in the model, for improved fidelity, the aerodynamic interaction effect between the rotor and the wing is included using an interference factor K_w that alters the total angle of attack. Lastly, the design uses a conventional lift curve slope where $C_{L_w} = C_{L_{\alpha,w}} \alpha_w + C_{L_{\alpha=0}}$. Additionally, the drag coefficient of the wing follows a parabolic drag polar equation, as expressed in Equation III.33, where AR is the aspect ratio of the wing and e is the Oswald efficiency factor.

$$C_{D_w} = C_{D_0} + \frac{C_{L_w}^2}{\pi \cdot AR \cdot e_0} \tag{III.33}$$

The forces and moments expressed in the body axis of the system can be grouped as shown below.

$$\begin{cases} \vec{F}_w = \begin{bmatrix} -D_w & 0 & -L_w \end{bmatrix}^T \\ \vec{M}_w = \vec{r}_w \times \vec{F}_w = \begin{bmatrix} 0 & h_w D_w + d_w L_w & 0 \end{bmatrix}^T \end{cases} \tag{III.34}$$

Table III.3: Wing parameters

Parameter	Symbol	Value	Unit
Surface area	S_w	10	m^2
Lift curve slope	$C_{L_{\alpha w}}$	5	rad^{-1}
Zero-AoA Lift coefficient	C_{L_0}	0.3	-
Drag polar offset	C_{D_0}	0.02	-
Aspect ratio	AR	5	-
Oswald efficiency factor	e_0	0.89	-
Aerodynamic interference factor	K_w	2	-
Anhedral angle	Γ	5	deg

2.5. Derivation of the fuselage model

The fuselage of the vehicle is represented in this model by its parasite drag force R_{fus}, defined by Equation III.35, and its aerodynamic moment contributions $C_{M_{fus}}$ and $C_{N_{fus}}$, around the y- and z-axis respectively. The drag of the body is approximated by its equivalent flat-plate area F_0.

$$R_{fus} = \frac{1}{2} \rho V^2 F_0 \tag{III.35}$$

Furthermore, due to the geometry of the fuselage, there exist induced aerodynamic moments around the pitch and yaw axes, the coefficients of which are shown in Equations III.36 and III.37 respectively. The fuselage is assumed symmetrical around the roll axis, thus no moment coefficient $C_{L_{fus}}$ is considered. It is necessary to take into account the effect of the aerodynamic interaction between the rotor and fuselage, which will impact the resulting angle of attack and sideslip angle, and which are represented by interference factor K_f. In (Pavel, 1996), citing (Marinescu & Anghel 1992), a value of 0.83 is suggested for the first one [**pavel96**] [**marinescu92**].

$$C_{M_{fus}} = \left(\frac{V}{\Omega R}\right)^2 \frac{1}{AR} K_f V_{f_M} \alpha_f \tag{III.36}$$

$$C_{N_{fus}} = \left(\frac{V}{\Omega R}\right)^2 \frac{1}{AR} K_f V_{f_N} \beta_f \tag{III.37}$$

V_{f_M} and V_{f_N} represent the volume of a body observed from their respective view, but having circular sections. Considerable to mention, is the assumption of the direct relationship between $C_{M,fus}$ and α_f. The angle of attack at which $M_{fus} = 0$ and the average downwash angle, are both considered to be zero, and would both be subtracted from α_f otherwise, to result in an effective AoA $\alpha_{eff} \neq \alpha_f$. The above are

gathered in the body frame as expressed in Equation III.38. R_{fus} was previously defined as such in the velocity frame, and so the vector is transformed using $\mathcal{T}_i^v$ from Appendix **??**.

$$\begin{cases} \vec{\mathbf{F}}_{\mathbf{fus}} = \mathcal{T}_i^v \cdot \begin{bmatrix} -R_{fus} & 0 & 0 \end{bmatrix}^T \\ \vec{\mathbf{M}}_{\mathbf{fus}} = \begin{bmatrix} 0 & M_{fus} & N_{fus} \end{bmatrix}^T \end{cases}$$

(III.38)

Table III.4: Fuselage parameters

Parameter	Symbol	Value	Unit
Equivalent flat plate area	F_0	18	m^2
Side view body volume having circular sections	V_{fusM}	25.53	m^3
Top view body volume having circular sections	V_{fusN}	6.13	m^3
Aerodynamic interference factor	K_f	0.83	-

2.6. Derivation of the empennage model

The empennage of this vehicle is an H-tail configuration featuring a central horizontal tail and one vertical fin on each side of it. The horizontal tail incorporates an elevator surface, the deflection of which assists primarily in pitch moment control. The the vertical tails entail a rudder surface each, that control yaw movement upon deflection. Initially, the velocity at which the airflow meets the horizontal and vertical tail are visible in Equation III.39 and Equation III.40 respectively.

$$V_t = \sqrt{u^2 + (w + ql_t)^2}$$

(III.39)

$$V_v = \sqrt{u^2 + (v + ph_v - rd_v)^2}$$

(III.40)

As seen, both airspeeds above are affected by the vehicle's attitude rates, via the induced velocity factors ql_{ht}, ph_{vt} and rl_{vt}. More specifically, a positive pitch rate increases the horizontal tail airspeed, and a positive roll rate does the same to the vertical tails, while a positive yaw rate negatively affects the latter. These affect the angle of attack and sideslip angle in an identical manner as they do V_t and V_v. The resulting force definitions of the empennage elements are expressed below.

$$L_t = \frac{1}{2}\rho V_t^2 S_t C_{L_{\alpha,t}} \alpha_t$$

(III.41)

$$Y_v = \frac{1}{2}\rho V_v^2 S_v C_{Y_{\beta,v}} \beta_v$$

(III.42)

The effect of the control surfaces are embedded in the coefficients $C_{L_{\alpha,t}}$ and $C_{Y_{\beta,v}}$ by way of vertical translation of the slope curves. That is, a positive elevator deflection δ_e raises the L_t/α_t slope by a factor of $dC_{L_{\alpha,t}}/d\delta_e$. In the same manner a positive rudder deflection δ_r raises the Y_v/β_v slope by $dC_{Y_{\beta,v}}/d\delta_r$. The contribution of the tail in the body dynamics is primarily through the negative pitch moment created by the positive lift. The lift force itself has little effect. A drag force is also present for model integrity, but negligible both in terms of force and moment contribution. Overall, the resulting vectors for the empennage are gathered. Equation III.43 outlines those for the horizontal tail, and Equation III.44 those for the vertical tails.
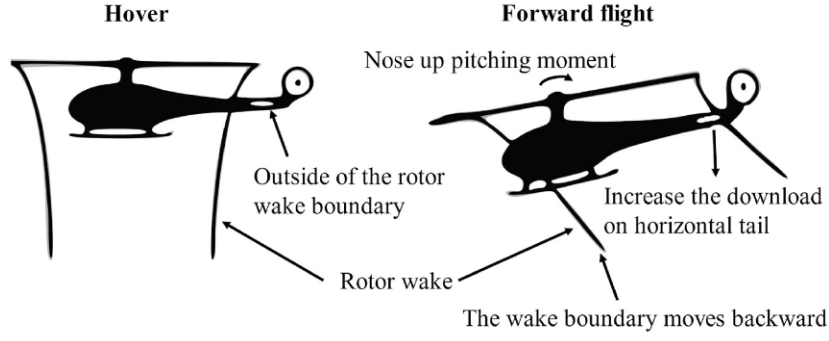
Figure 2.24: Aerodynamic interference between the tail and rotor wake [41]

Once again, the tail interacts with the rotor wake, but here at higher speeds mostly, as can be portrayed by Figure 2.24. This is modeled by an interference factor, multiplied by the effective downwash, which is airspeed dependent.

$$\begin{cases} \vec{\mathbf{F}}_\mathbf{t} = \begin{bmatrix} -D_t & 0 & -L_t \end{bmatrix}^T \\[2mm] \vec{\mathbf{M}}_\mathbf{t} = \vec{\mathbf{r}}_\mathbf{t} \times \vec{\mathbf{F}}_\mathbf{t} = \begin{bmatrix} 0 & h_t D_t - d_t L_t & 0 \end{bmatrix}^T \end{cases} \tag{III.43}$$

$$\begin{cases} \vec{\mathbf{F}}_\mathbf{v} = \begin{bmatrix} 0 & -Y_v & 0 \end{bmatrix}^T \\[2mm] \vec{\mathbf{M}}_\mathbf{v} = \vec{\mathbf{r}}_\mathbf{v} \times \vec{\mathbf{F}}_\mathbf{v} = \begin{bmatrix} h_v Y_v & 0 & -d_v Y_v \end{bmatrix}^T \end{cases} \tag{III.44}$$

Table III.5: Empennage parameters

Parameter	Symbol	Value	Unit
Lift curve slope	$C_{L_{\alpha t}}$	3.5	-
Lift-elevator slope	$dC_{L_{\alpha t}}/d\delta_e$	0.859	rad^{-1}
Drag-elevator slope	$dC_{D_{\alpha t}}/d\delta_e$	0.03	rad^{-1}
Horizontal tail Incidence angle	α_{0t}	0.07	rad
Horizontal tail surface area	S_t	2.5	m^2
Aerodynamic interference factor	K_t	1.5	-
Y-force curve slope	$C_{Y_{\beta v}}$	4	-
Drag-rudder slope	$dC_{D_{\beta v}}/d\delta_r$	0.03	rad^{-1}
Y-rudder slope	$dC_{Y_{\beta v}}/d\delta_r$	0.859	rad^{-1}
Vertical tail Incidence angle	β_{0v}	-0.08	rad
Vertical tail surface area	S_v	2	m^2

2.7. Unified body dynamics

This section unifies the total dynamics of the modelled vehicle, analyzed over this section. Equation III.45 gathers all forces an moments in two corresponding vectors, both acting on the center O^b of the body-fixed reference frame $O^b x^b y^b z^b$. Note that due to offset distance s_{off} of the CG, these two do not coincide.

$$\begin{cases} \vec{\mathbf{F}}_\mathbf{tot} = \vec{\mathbf{F}}_\mathbf{R} + \vec{\mathbf{F}}_\mathbf{p} + \vec{\mathbf{F}}_\mathbf{w} + \vec{\mathbf{F}}_\mathbf{fus} + \vec{\mathbf{F}}_\mathbf{t} + \vec{\mathbf{F}}_\mathbf{v} \\[2mm] \vec{\mathbf{M}}_\mathbf{tot} = \vec{\mathbf{M}}_\mathbf{R} + \vec{\mathbf{M}}_\mathbf{p} + \vec{\mathbf{M}}_\mathbf{w} + \vec{\mathbf{M}}_\mathbf{f} + \vec{\mathbf{M}}_\mathbf{t} + \vec{\mathbf{M}}_\mathbf{v} \end{cases} \tag{III.45}$$

A total of 12 states are part of this model's system of equations and they are listed below;

- The body velocities: $\vec{\mathbf{u}} = \begin{bmatrix} u & v & w \end{bmatrix}^T$

- The Euler angles that express the vehicle's attitude with respect to the $O^n x^n y^n z^n$ frame: $\vec{\theta} = \begin{bmatrix} \varphi & \vartheta & \phi \end{bmatrix}^T$

- The body angular velocities: $\vec{\omega} = \begin{bmatrix} p & q & r \end{bmatrix}^T$, and

- The quasi-dynamic inflows of the rotor and the two propellers described earlier: $\vec{\lambda_0} = \begin{bmatrix} \lambda_0 & \lambda_{0pp} & \lambda_{0ps} \end{bmatrix}^T$

Note the positional vector $\begin{bmatrix} x & y & z \end{bmatrix}^T$ is not of interest in this study as the purpose is the finding of steady-state operating points in forward flight, and these states are necessary in control-system design, and simulation of maneuvering flight. This article assumes a rigid body with constant mass M and inertia $\mathbf{J}$ moving along a flat, non-rotating Earth with a uniform gravity field of acceleration $\vec{\mathbf{g}}$. The final EOMs is a final set of differential equations, to be solved, and fed back to the system dynamically as states next to the inputs. In the computational aspect of this thesis, their solution was obtained using Runge-Kutta numerical integration, by way of the MATLAB® function *ode45*. They are firstly comprised of the translational dynamics of Equation III.46, where the second factoy of the right-hand side entails the gravitational force transformation to the body frame, which in some expression in literature, is embedded in the $\mathbf{F_{tot}}$ vector.
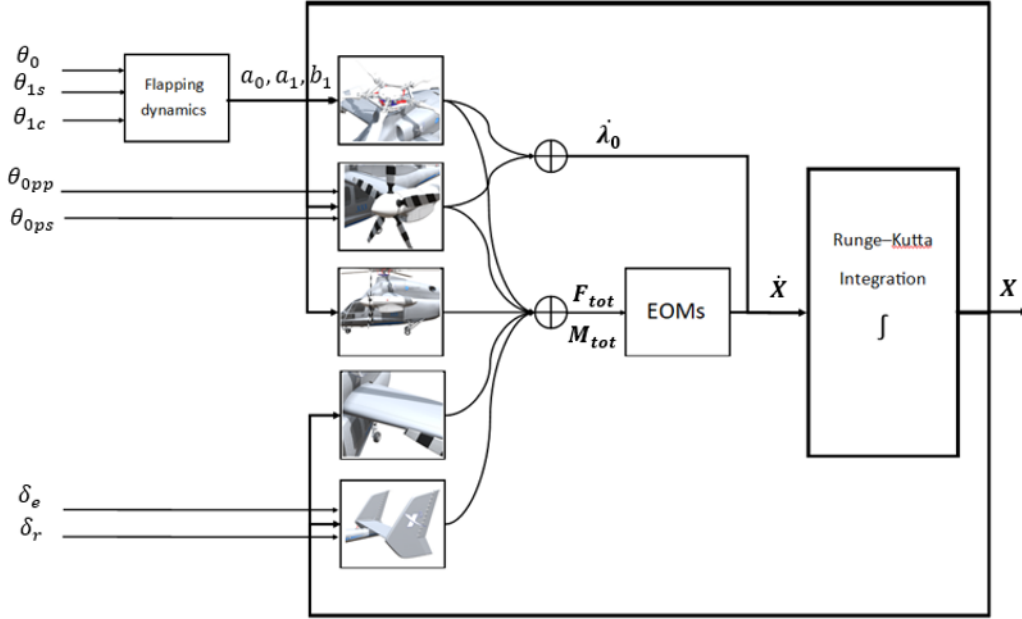
Figure 2.25: Modeling scheme

$$\dot{\mathbf{u}} = \frac{1}{M}\mathbf{F_{tot}} + \mathcal{T}_n^b \begin{bmatrix} 0 & 0 & g \end{bmatrix}^T - \omega \times \mathbf{u} \tag{III.46}$$

In the absence of the positional vector, that was just mentioned, the kinematics of the translational motion are not included in the EOMs, but for expansion of this model, they are represented by the differential equation $\dot{\mathbf{x}} = \mathcal{T}_b^n \mathbf{u}$, where $\dot{\mathbf{x}}$ is the derivative of $\begin{bmatrix} x & y & z \end{bmatrix}^T$ and $\mathcal{T}_b^n = \{\mathcal{T}_n^b\}^{-1}$ is the transformation back to the NED frame. Additionally, the definitions of the dynamics and kinematics of the rotational motion are respectively displayed in Equations III.47 and III.48.

$$\dot{\omega} = \mathbf{J}^{-1}[\mathbf{M_{tot}} - \omega \times \mathbf{J}\omega] \tag{III.47}$$

$$\dot{\theta} = \mathcal{O}_b^n \omega \tag{III.48}$$

Although, translational kinematics are not included, the rotational description is necessary to this research, as the orientation of the vehicle relative to the NED frame in steady-state operation is vital. Lastly, the three quasi-dnamic inflows are part of the EOMs, all three of which follow the same expression as that of Equations III.24, III.25 and III.26. Now that the mathematical model is finalized, and ready to be manipulated dynamically, the following steps towards a linearized compound helicopter will be investigated.

3. Trim Optimization

Having modelled the 9-DoF compound helicopter thoroughly under valid assumptions and approximations, the research proceeds to the trim phase of said model. In this section, steady-state operating points are discovered throughout the vehicle's airspeed range in forward flight, under which it will function in mechanical equilibrium. The challenge that is presented now, is the redundant number of available control inputs on the aircraft. That is, in order to achieve higher cruise speeds, as is the goal of compound helicopters, the total control effort has to be allocated among the actuators, which then should lead to the slowing of the main rotor, avoiding therefore compressibility effects on the advancing side and dynamic stalling on the retreating side. The second of the fundamental problems of flight dynamics concerns trim and states there exists a set of state and input vectors $\mathbf{X}^*$ and $\mathbf{U}^*$ such that:

$$f(X^*, U^*) = 0 \tag{III.49}$$

and in this particular case:

$$\mathbf{f}(X^*, U^*) = \dot{X} = \begin{bmatrix} \dot{u} & \dot{\theta} & \dot{\omega} & \dot{\lambda}_0 \end{bmatrix}^T \tag{III.50}$$

For clarity, the function f here is the derived nonlinear model. In literature, the section focusing on the trim is a relatively small one, as it is usually a straightforward process. Most aircraft models are critically actuated, leading to an analytical trim that will provide a unique solution $(\mathbf{X}^*, \mathbf{U}^*)$ for each operating condition in the flight envelope. This is not the case in discussion here. More specifically, the control inputs vector $\mathbf{U}$ is displayed in Equation III.51. In some models in literature the control of the propellers have been represented by inputs $\bar{\theta}_{0p}$ and θ_{diff}, meaning mean and differential propeller pitch instead of directly having available ϑ_{0pp} and ϑ_{0ps} [15]. However, the only difference the first version makes, is two additional equations, a sum and a subtraction of the two within the model.

$$\mathbf{U} = \begin{bmatrix} \vartheta_0 & \vartheta_{1s} & \vartheta_{1c} & \vartheta_{0pp} & \vartheta_{0ps} & \delta_e & \delta_r \end{bmatrix}^T \tag{III.51}$$

Between this, and the 12-entry state vector, the objective leads to a trim vector showed below.

$$\mathbf{u_{trim}} = \begin{bmatrix} \varphi & \vartheta & \lambda_0 & \lambda_{0pp} & \lambda_{0ps} & \mathbf{U}^T \end{bmatrix}^T \tag{III.52}$$

Thus, this is evidence of an over-actuated system, for which analytical trim is not possible, as the system is highly coupled, meaning there is multiple instances where more than one controls affect a single motion of the helicopter, either translational or rotational. Mathematically, this case serves as an under-determined system of equations, with more unknowns than equations in place. The solution is searched therefore, by means of numerical trim optimization.

3.1. Process

Gaining a deeper physical comprehension and insight into the behavior of a compound helicopter system can potentially expedite the identification of optimal control parameters. This could entail determining which redundant controls have greater efficacy and which ones exhibit less sensitivity towards specific objectives, or identifying the optimal sequence for executing redundant controls and their corresponding effects. This knowledge base could significantly reduce the search space for both numerical optimization algorithms and fly-to-optimal approaches, thereby enabling a faster in-flight determination of the optimal state [60]. In the context of model-based optimization, a common approach to compute a steady-state operating point involves imposing constraints on the system variables, inputs, or outputs. These constraints may take the form of fixed values or bounds, which guide the optimization search towards a suitable solution. Nevertheless, in certain scenarios, the optimization search may benefit from increased flexibility in the definition of its parameters to accommodate specific system requirements or application constraints. The main element in need of definition during numerical optimization are an objective function given by;

$$\text{cost} = \min_{\mathbf{u_{trim}}} J = \arg\min_{\mathbf{u_{trim}}} \left\| \dot{\mathbf{X}} \right\|, \tag{III.53}$$

$$\text{subject to} : \mathbf{c}(\mathbf{U}) : \delta_{\mathbf{lb}} \leq \mathbf{U} \leq \delta_{\mathbf{ub}}$$

where Table III.6 outlines the constraint function set $\mathbf{c}(\mathbf{U})$, sourcing from the physical upper- and lower-bound limits of the actuators. Computational optimization algorithms interpret equalities and inequalities separately, but given their decimal points size, essentially the constraints follow the "less than or equal to" constraint. Furthermore, these can only be coded as one-sided, meaning the table translates to 14 constraints applied to the algorithm.
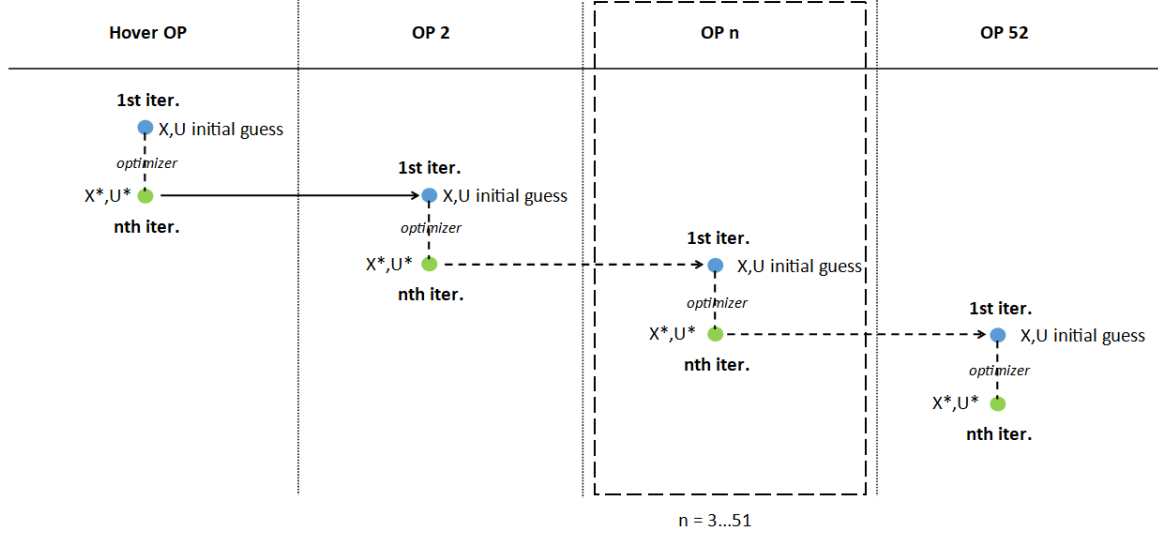
Figure 3.26: Operating point search scheme

The point of this subsection has been to overcome the hurdle of not being able to obtain an operating point analytically. However, remaining in this stage is still not a desirable result. Let the aforementioned formulation of Equation III.53 and Table III.6. Given the physical capabilities there exist multiple operating points $\text{OP}_k = \{\mathbf{X}^*, \mathbf{U}^*\}$ that follow the relation;

$$\text{OP}_k \in \mathbb{S}^7 \quad \forall k \in \{1, 2, 3, ...n\} \tag{III.54}$$

where $\mathbb{S}^7$ is the seven-dimensional space of solutions that satisfy Equation III.53 at a single forward airspeed under the applied optimization tolerance. Lowering this tolerance will potentially reduce the size of this set but still to a non-singular amount of solutions. The next approach at this point can take many directions depending on the goal of the study, such as a secondary objective function making this solution a multi-objective optimization. This research however, utilizes the methods of control allocation to obtain the required operating points.

Table III.6: Controls limits

Constraints	Limits
Rotor Collective	$0.4° \leq \vartheta_0 \leq 16.4°$
Longitudinal cyclic	$-16° \leq \vartheta_{1s} \leq 16°$
Lateral cyclic	$-8° \leq \vartheta_{1c} \leq 8°$
Port-side propeller pitch	$0.4° \leq \vartheta_{0pp} \leq 16.4°$
Starboard-side propeller pitch	$0.4° \leq \vartheta_{0ps} \leq 16.4°$
Elevator	$-25° \leq \delta_e \leq 15°$
Rudder	$-15° \leq \delta_r \leq 15°$

3.2. Control Allocation

In this field, various processes are devised in order to either tackle the over-actuation problem, or eliminate part of a control effort in certain scenarios. Suppose a system with a control effectiveness

matrix $\mathbf{B_e}$ as defined below. The highlighted problem exists when the matrix is non-square, and more columns are present than rows. As it is known in classical control theory and linear algebra, the inverse of such matrix cannot be computed, and so, no direct solution can be found.

$$\mathbf{B_e} = \begin{bmatrix} \frac{\partial L}{\partial \delta_1} & \frac{\partial L}{\partial \delta_2} & \cdots & \frac{\partial L}{\partial \delta_n} \\[2mm] \frac{\partial M}{\partial \delta_1} & \frac{\partial M}{\partial \delta_2} & \cdots & \frac{\partial M}{\partial \delta_n} \\[2mm] \frac{\partial N}{\partial \delta_1} & \frac{\partial N}{\partial \delta_2} & \cdots & \frac{\partial N}{\partial \delta_n} \end{bmatrix} \tag{III.55}$$

In the field of control allocation, strategies are searched for in order to bring this matrix to invertible form, and obtain a set of inputs as a result to the trim problem, most of which have been attempted, and a particular one proved the best. Explicit ganging, firstly, is an a priori method for combining or ganging effectors in order to produce a single effective control from multiple devices. Additionally, the weighted Moore-Penrose pseudo-inverse matrix has been calculated according to [61]:

$$\mathbf{B_{mp}} = \mathbf{W}^{-1}\mathbf{B_e}^T \left(\mathbf{B_e}\mathbf{W}^{-1}\mathbf{B_e}^T \right)^{-1} \tag{III.56}$$

It should be noted as a reminder, that this system is non-linear, which implies that the control-effectiveness matrix $\mathbf{B_e}$ is not readily available, in order for this method to be given a try. It has therefore, been manually constructed, after initially trimming the model numerically, obtaining one of the operating points in the solution subspace $\mathbb{S}^7$, and then perturbing the inputs from their trimmed state to come up with the required matrix. This virtual "re-allocation" method, requires a solution subspace that is not null, and non-singular. In literature, control allocation is applied primarily in control systems desing, in which stage, an linear system is potentially already available, where as here, it is the final goal. Furthermore, it is inefficient for the weighted methods to be used as such, because multiple instances of trial and error have to happen to get a unique useful $\mathbf{W}$ matrix for each airspeed in trim. The resulting method that has been followed overall, is a Direct Allocation, by means of a mapping function f_{CA} in the optimization, which also uses weighted penalization of certain undesirable controls.

$$f_{CA}(U) = \delta_{lb} \leq WU \leq \delta_{ub}$$

$$\text{with} : \mathbf{W} = \begin{bmatrix} w_1 & 0 & \cdots & 0 \\ 0 & w_2 & \cdots & 0 \\ \vdots & \vdots & \ddots & \vdots \\ 0 & 0 & \cdots & w_7 \end{bmatrix} \tag{III.57}$$

Along the forward flight speed range, the penalty of the longitudinal cyclic increases at higher speeds, in order for the propellers to be used primarily for forward thrust. The empennage surfaces are constantly weighed by a small factor, in order. The collective left unallocated as it only adds vertical thrust on top of the wing lift, when necessary. Similarly, the lateral cyclic is unallocated since it is the only input that controls the rolling motion. The product of this methodology is outlined in the Results section.

Table III.7: Rotor parameters

Optimizer	Runtime	Cost at arbitrary OP
graddescent	1328.7	$3.9 \cdot 10^{-9}$
graddescent-proj	674.7	$3.8 \cdot 10^{-6}$
graddescent-elim	**500.6**	$\mathbf{8.1 \cdot 10^{-14}}$
lsqnonlin	805.5	$2.8 \cdot 10^{-3}$
lsqnonlin-proj	2930.0	$1.3 \cdot 10^{-3}$

After the detailed trim procedure, the research has ended up with the most challenging result to obtain, the trimmed operating points along the forward speed range of the aircraft's flight envelope. In contrast to literature, a higher trim resolution has been chosen, with an operating point being sought at every 5 knots. The reason for this is the fact that in this algorithm, each operating point is chosen as initial guess for the optimization of the next one. Such a method is needed, in similar problems, where there is a large number of available solutions, which is hard to navigate through. In combination with the inherent instabilities of helicopters, a smooth change in controls needs to be present, so that no large jump of input is needed suddenly. The following spider plots give a visual representation of how the controls of the aircraft are distributed following the trim process.
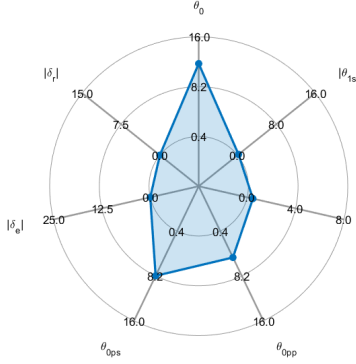
Figure 3.27: Control effort in hover
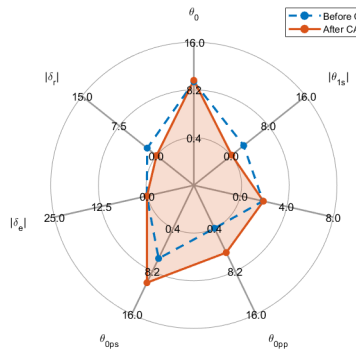
Figure 3.28: Control effort at u = 50kts
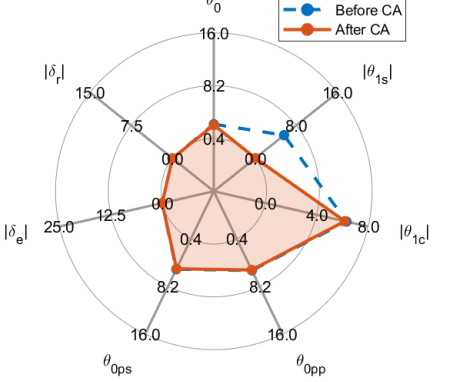
Figure 3.29: Control effort at u = 200kts
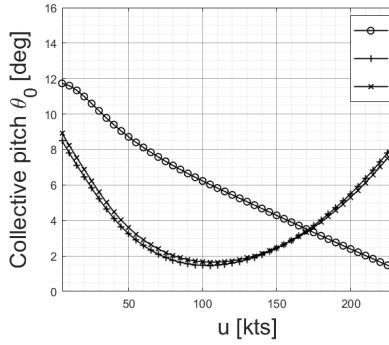
Figure 3.30: Collective pitch trim
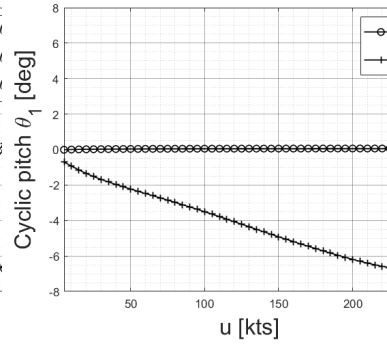
Figure 3.31: Cyclic trim
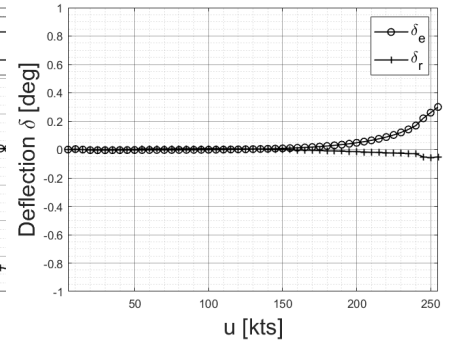
Figure 3.32: Empennage deflections trim

Note that, outside of the three collectives, the axes are in absolute value, because the amount of deflection from zero is important to see, rather than the actual sign of the controls. Initially, in Figure 3.27 a single line can be seen. The reason for this is that it has been the only stage in which control allocation has not been necessary. For hover, there is not airflow for the empennage surfaces to manipulate, so then, they are simply not deployed, which stops making the system over-actuated. In the adjacent two plots, the distribution of the control effort is shown for a low speed of 50 knots, and a high one of 200 knots. In them, the unallocated controls are seen in the dashed-blue contour, and the final distribution after control allocation in the shaded red region.
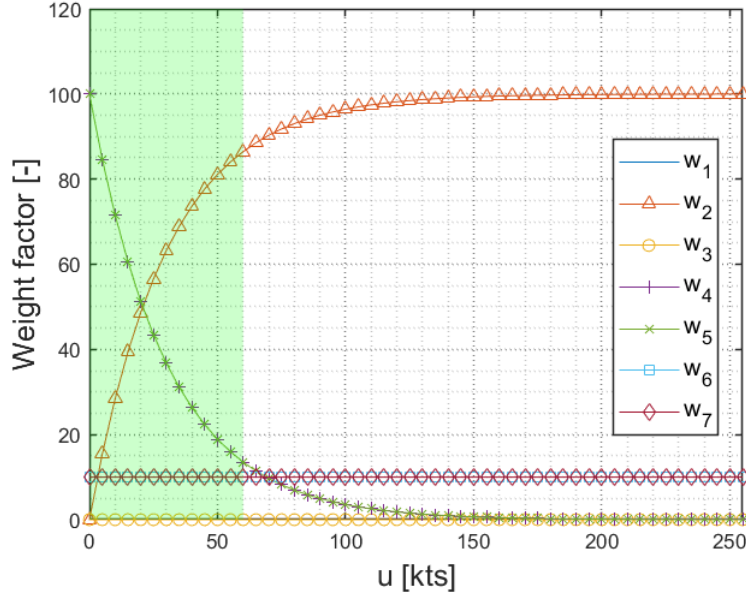
Figure 3.33: Resulting weight selection

In hover, the inputs δ_e and δ_r are at zero, as said before. The rotor collective is at its maximum value, since no lift-compounding takes place in the absence of airflow around the wing. Actually, the collective is even larger than it would be for the same helicopter without a wing, meaning not only does the wing not help with a lift force it hover, but it is a drawback, since its position in the middle of the rotor wake creates an induced download on the vehicle, to be compensated by the main rotor. The yaw control by the propellers can be visible by the slightly higher starboard propeller pitch value, which result in a higher thrust value, which in turn leads to a compensatory yaw moment. Regarding the two plots for forward flight, there is clear reduction of the rotor collective as speed increases, and the differential thrust remains present. Furthermore, the mean propeller pitch increases with speed, so that the required thrust is provided. Lastly, the very clear drop between the two contours is the one of the longitudinal cyclic of the rotor, an effect of the applied weights from **??**. In the end, the overall trim results of all controls at all airspeeds are viewed in Figures 3.30, 3.31 and 3.32.

3.3. Attainable Moment Set

The collection of moments that can be generated by the actuators at any operating point in this study is known in the field as the Attainable Moment Set (AMS) or sometimes as Effective Moment Set. It results from a hyper-rectangle in the seven-dimensional Control Space $\mathbb{R}^7$, the Admissible Controls Set (ACS), containing all possible combinations of inputs, and not to be confused with the set $\mathbb{S}^7$ from earlier, which has only the ones that satisfy the objective function. The characterization of the AMS in the presence of non-linearities and couplings within the control effectors' aerodynamic model poses a significant challenge. Linearizing the aerodynamic model with respect to control positions enables the definition of a linear function utilizing the control effectiveness matrix $\mathbf{B_e}$, serving as an approximation of the mapping between the ACS and the AMS. It has been proven that the resulting AMS exists as a bounded convex polytope in three-dimensional space $\mathbb{R}^3$ [62]. The construction of the AMS entails employing a geometric algorithm detailed in [63] for scenarios where the number of control effectors is either 2 or 3. Additionally, an extension of this algorithm has been proposed in [**varriale22**] to encompass systems with arbitrary dimensions in Moment Space. Here, the AMS then, is a convex hull in the Cartesian axis system in $\mathbb{R}^3$ with the change in moments Δ_L, Δ_M and Δ_N placed on each axis. It encloses all possible moment perturbation vector, attainable at a specific dynamic point, hence the name. Figures 3.34 and 3.35 display it for the operating points OP at low and high speed.
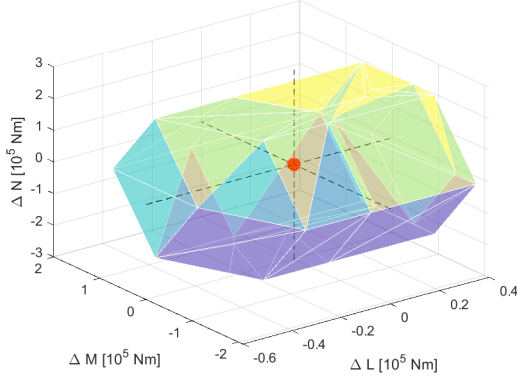
Figure 3.34: AMS from OP at u = 50kts
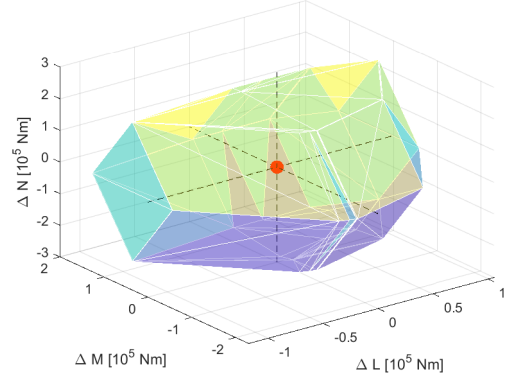
Figure 3.35: AMS from OP at u = 200kts

An additional feature is that when the non-linear model is linearized with respect to the operating points, the control effectiveness matrix $\mathbf{B_e}$ of Equation III.55 defines a linear function which maps the ACS to the AMS. The attribute of interest, though, is the trim point, indicate by the red marker at the origin of all surface plots. In a research of equilibrium search, it is necessary to show the dimension size of this problem that has been mentioned. Similarly to how $\mathbf{B_e}$ maps any point of the ACS to the surface, the pseudo-inverse fulfills the opposite route, and the function created in this study f_{CA} maps the trim point back to the solution space $\mathbb{S}^7$. This result is vital as it not only shows the order of the complex derived model, but also is a blueprint for coordination within it. these results, are crucial for the design of a control allocator, to follow a controller in a feed-forward loop, that will get fed a control effort vector necessary, which will lead to a smaller region within the AMS, called the Rerquired Moment Space (RMS), and will output a mapped solution to command the actuators. Figure 3.36 displays the utilization of the AMS surface in terms of mapping the trim point as well as the desirable maneuver moments back to the control vector.
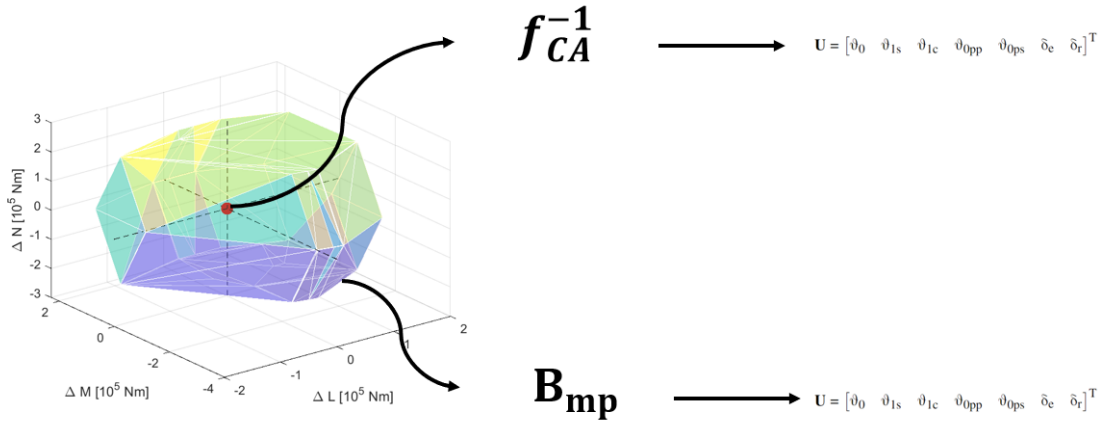
Figure 3.36: Attainable Moment Space to Control Space mapping

4. Linearization

Now that the desired operating points have finally been determined, it is time to linearize the system, in order for it to be efficiently controlled and simulated in the future.

4.1. Linearization methodlogy

Recall that this inherently non-linear model is easily reprenseted by;

$$\dot{\mathbf{X}} = f(\mathbf{X}, \mathbf{U}) \tag{III.58}$$

and the goal is to describe it in state-space formation, of the form:

$$\dot{\mathbf{x}} = \mathbf{A}\mathbf{x} + \mathbf{B}\mathbf{u} \tag{III.59}$$

Matrices $\mathbf{A}$ and $\mathbf{B}$ contain the stability and control derivatives respectively, whereas their adjacent vectors are the state and input perturbations from the trimmed operating points. This means this representation varies with airspeed. The numerical linearisation process to reduce the equations of motion into linear form follows the fundamental assumption that the vehicle's state derivatives can be expressed by a Taylor-series expansion. Let a perturbation from one of the trim state be denoted by the vectors $\delta_{\mathbf{X}}$ and $\delta_{\mathbf{U}}$. At that moment, the system's nonlinear motion is given by;

$$\dot{\mathbf{X}} + \delta\dot{\mathbf{X}} = f(\mathbf{X}^*, \mathbf{U}^*) + \frac{\partial f}{\partial \mathbf{X}}\delta\mathbf{X} + \frac{\partial f}{\partial \mathbf{U}}\delta\mathbf{U} \tag{III.60}$$

Having already chosen the set of $(\mathbf{X}^*, \mathbf{U}^*)$ in **??** such that $\dot{\mathbf{X}} = f(\mathbf{X}^*, \mathbf{U}^*) = 0$, the Taylor-series now becomes;

$$\delta\dot{\mathbf{X}} = \frac{\partial f}{\partial \mathbf{X}}\delta\mathbf{X} + \frac{\partial f}{\partial \mathbf{U}}\delta\mathbf{U} \Rightarrow \dot{\mathbf{X}} \approx \frac{\partial f}{\partial \mathbf{X}}\mathbf{X} + \frac{\partial f}{\partial \mathbf{U}}\mathbf{U} \tag{III.61}$$

and the approximation is finalized by dropping the differential notation δ from the vectors, and by equating the Jacobians $\frac{\partial f}{\partial \mathbf{X}}$ and $\frac{\partial f}{\partial \mathbf{U}}$ to $\mathbf{A}$ and $\mathbf{B}$ to obtain Equation III.59

4.2. Linearization results

Having processed everything up to now, the article is finalized with the linearization of the model in forward flight. Such a highly coupled non-linear system provides great benefit when having been realized, especially to the control system design phase. Following the methodology of section 4, the process ends up with a set of system and control matrices $\mathbf{A}, \mathbf{B}$. For the chosen cases of hover, low speed and high speed, the resulting matrices are available below. Having those, it is important to show the open-loop instability of such a system. It is a classic method in control-system design to view the sensitivity of a system, without being placed inside a control loop. In this test, the longitudinal cyclic is perturbed by 1 degree for 0.5 seconds from the trimmed state of hover, as visible below.
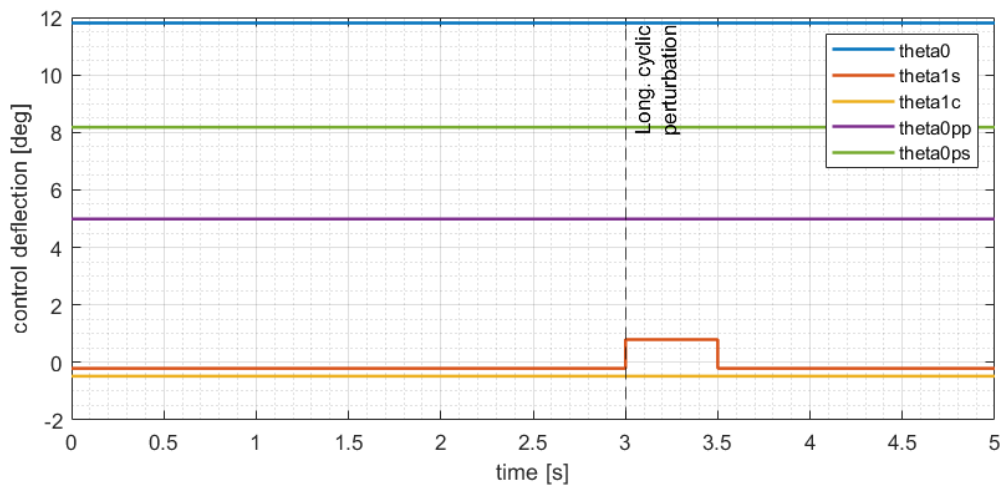
Figure 4.37: Perturbation of the longitudinal cyclic in hover

Note that this is the allocated control effort in hover, and hence, no elevator or rudder deployment is visible. As a result, the states of the helicopterdiverge as seen in
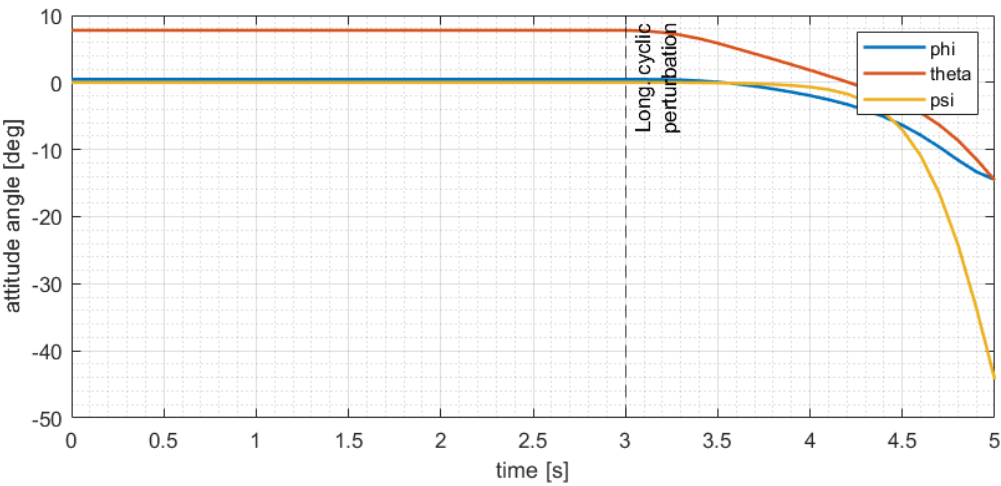
Figure 4.38: Instability of the translational states
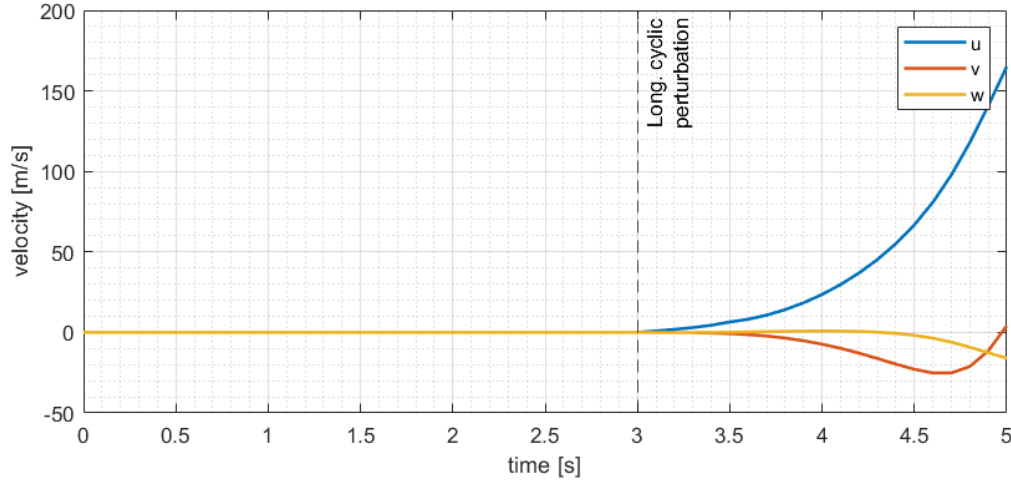
Figure 4.39: Instability of the angular states

Overall there is an obvious need need for a robust intelligent control system in feedback loop formation, in order to be able to achieve desired manoeuvres in between operating points of forward flight. With a linear system, this research definitively sets the stage for the following steps to take place in order for it to be achieved.

$$
A = \begin{bmatrix}
0.000 & 0.000 & 0.000 & 0.000 & 0.000 & 0.000 & 1.000 & 0.001 & 0.136 & 0.000 \\
0.000 & 0.000 & 0.000 & 0.000 & 0.000 & 0.000 & 0.000 & 1.000 & -0.008 & 0.000 \\
0.000 & 0.000 & 0.000 & 0.000 & 0.000 & 0.000 & 0.000 & 0.008 & 1.009 & 0.000 \\
0.000 & -9.720 & 0.000 & 0.128 & 0.000 & 0.003 & -0.577 & 0.990 & 0.000 & 11.463 \\
9.720 & -0.011 & 0.000 & 0.007 & -0.000 & 0.000 & 0.017 & 0.105 & 0.000 & 1.634 \\
-0.081 & -1.325 & 0.000 & 0.004 & 0.000 & -0.000 & 0.031 & -0.062 & 0.000 & 196.180 \\
0.000 & 0.000 & 0.000 & 0.089 & 0.000 & -0.000 & -2.019 & 1.717 & 0.038 & -13.664 \\
0.000 & 0.000 & 0.000 & -0.035 & 0.000 & -0.001 & 0.266 & -0.017 & -0.000 & 3.773 \\
0.000 & 0.000 & 0.000 & 0.014 & 0.000 & -0.000 & -0.334 & 0.294 & 0.083 & -5.477 \\
0.000 & 0.000 & 0.000 & -0.000 & 0.000 & 0.000 & 0.000 & 0.000 & 0.000 & -3.260
\end{bmatrix}
$$

$$
B = \begin{bmatrix}
0.000 & 0.000 & 0.000 & 0.000 & 0.000 & 0.000 & 0.000 \\
0.000 & 0.000 & 0.000 & 0.000 & 0.000 & 0.000 & 0.000 \\
0.000 & 0.000 & 0.000 & 0.000 & 0.000 & 0.000 & 0.000 \\
-7.015 & 9.720 & -0.004 & 11.870 & 11.870 & 0.000 & 0.000 \\
-1.089 & 0.000 & 9.734 & 0.000 & 0.000 & 0.000 & 0.000 \\
-130.787 & -0.521 & -0.081 & 0.000 & 0.000 & 0.000 & 0.000 \\
9.896 & 0.102 & 57.173 & 3.169 & -3.169 & 0.000 & 0.000 \\
-2.793 & -15.232 & -0.002 & -5.251 & -5.251 & 0.000 & 0.000 \\
5.359 & 0.170 & 9.206 & 6.881 & -6.881 & 0.000 & 0.000 \\
0.758 & 0.000 & 0.000 & 0.000 & 0.000 & 0.000 & 0.000
\end{bmatrix}
$$

Low speed: u = 50kts

$$
A = \begin{bmatrix}
0.000 & 0.000 & 0.000 & 0.000 & 0.000 & 0.000 & 1.000 & -0.002 & 0.116 & 0.000 \\
0.000 & 0.000 & 0.000 & 0.000 & 0.000 & 0.000 & 0.000 & 1.000 & 0.015 & 0.000 \\
0.000 & 0.000 & 0.000 & 0.000 & 0.000 & 0.000 & 0.000 & -0.015 & 1.007 & 0.000 \\
0.000 & -9.744 & 0.000 & 0.148 & 0.000 & -0.553 & -0.594 & 1.048 & 0.000 & -171.760 \\
9.743 & 0.017 & 0.000 & 0.011 & -0.006 & 0.066 & 0.122 & 0.069 & -25.669 & -16.102 \\
0.150 & -1.135 & 0.000 & -0.026 & 0.000 & -0.864 & -0.220 & 25.626 & 0.000 & 198.847 \\
0.000 & 0.000 & 0.000 & 0.082 & 53.933 & 0.041 & -1.561 & 1.691 & 0.890 & -10.079 \\
0.000 & 0.000 & 0.000 & -0.038 & 0.000 & 21.691 & 0.261 & -0.287 & -0.000 & 98.204 \\
0.000 & 0.000 & 0.000 & 0.010 & 117.272 & 0.011 & -0.424 & 0.315 & 0.983 & -2.629 \\
0.000 & 0.000 & 0.000 & -0.002 & 0.000 & 0.004 & 0.001 & 0.000 & 0.000 & -3.467
\end{bmatrix}
$$

$$
B = \begin{bmatrix}
0.000 & 0.000 & 0.000 & 0.000 & 0.000 & 0.000 & 0.000 \\
0.000 & 0.000 & 0.000 & 0.000 & 0.000 & 0.000 & 0.000 \\
0.000 & 0.000 & 0.000 & 0.000 & 0.000 & 0.000 & 0.000 \\
-15.273 & 5.962 & 0.001 & 64.907 & 64.907 & 0.000 & 0.000 \\
3.213 & 1.708 & 8.421 & 0.000 & 0.000 & 0.000 & 0.004 \\
-132.345 & -21.539 & 0.016 & 0.000 & 0.000 & 0.015 & 0.000 \\
20.988 & 1.173 & 59.126 & 41.592 & -41.592 & 0.000 & 0.033 \\
-0.662 & -16.252 & 0.001 & -28.715 & -28.715 & 0.031 & 0.000 \\
5.523 & 0.427 & 9.521 & 90.303 & -90.303 & 0.000 & -0.007 \\
0.767 & 0.108 & 0.000 & 0.000 & 0.000 & 0.000 & 0.000
\end{bmatrix}
$$

High speed: u = 50kts

$$
A = \begin{bmatrix}
0.000 & 0.000 & 0.000 & 0.000 & 0.000 & 0.000 & 1.000 & -0.087 & 0.491 & 0.000 \\
0.000 & 0.000 & 0.000 & 0.000 & 0.000 & 0.000 & 0.000 & 0.985 & 0.174 & 0.000 \\
0.000 & 0.000 & 0.000 & 0.000 & 0.000 & 0.000 & 0.000 & -0.195 & 1.100 & 0.000 \\
0.000 & -8.779 & 0.000 & -0.295 & 0.000 & -1.934 & -0.318 & 1.467 & 0.000 & -171.345 \\
8.644 & 0.763 & 0.000 & -0.004 & -0.023 & -0.012 & 0.109 & 0.190 & -102.678 & 2.976 \\
1.530 & -4.311 & 0.000 & -0.045 & 0.000 & -1.041 & -1.041 & 102.801 & 0.000 & 209.257 \\
0.000 & 0.000 & 0.000 & 0.098 & 215.731 & 0.389 & 0.581 & 1.271 & 2.079 & -94.295 \\
0.000 & 0.000 & 0.000 & 0.176 & 0.000 & 86.884 & 0.417 & -1.499 & 0.000 & 106.022 \\
0.000 & 0.000 & 0.000 & 0.005 & 469.086 & 0.037 & -0.579 & 0.245 & 0.716 & -8.994 \\
0.000 & 0.000 & 0.000 & -0.000 & 0.000 & 0.005 & 0.006 & 0.000 & 0.000 & -9.631
\end{bmatrix}
$$

$$
B = \begin{bmatrix}
0.000 & 0.000 & 0.000 & 0.000 & 0.000 & 0.000 & 0.000 \\
0.000 & 0.000 & 0.000 & 0.000 & 0.000 & 0.000 & 0.000 \\
0.000 & 0.000 & 0.000 & 0.000 & 0.000 & 0.000 & 0.000 \\
-23.484 & -11.795 & 0.008 & 64.885 & 64.885 & 0.000 & 0.000 \\
-21.351 & -1.259 & -1.899 & 0.000 & 0.000 & 0.000 & 0.069 \\
-163.369 & -82.936 & 0.077 & 0.000 & 0.000 & -0.046 & 0.000 \\
110.593 & 39.984 & 74.353 & 41.578 & -41.578 & 0.000 & 0.524 \\
14.316 & -16.207 & 0.003 & -28.705 & -28.705 & -0.093 & 0.000 \\
11.669 & 3.782 & 11.973 & 90.273 & -90.273 & 0.000 & -0.118 \\
0.962 & 0.482 & 0.000 & 0.000 & 0.000 & 0.000 & 0.000
\end{bmatrix}
$$

IV

Wrap-up

1. Conclusion

In conclusion, this research has demonstrated a commendable level of comprehensiveness and depth in presenting its findings, introducing innovative methods in the field of flight dynamics and numerical trim optimization. The derived linear 9 Degree of Freedom mathematical model has undergone extensive analysis, providing valuable insights into the stability, response characteristics, and the ability to simulate a wide range of maneuvers and trajectories. Through this thorough examination, the behavior of the system has been meticulously explored across the entire forward flight envelope, with operating points established at 5-knot intervals, spanning from hover to a remarkable 255 knots of forward flight airspeed. The transparency achieved in understanding the system's behavior throughout the forward flight envelope has played a pivotal role in facilitating the design of an efficient and effective control subsystem. By gaining comprehensive insights into the dynamic response of the compound helicopter, engineers and researchers have been able to develop a control system that enables precise command and control over the aircraft's performance.

The ability to finely tune and modulate the control inputs at various operating points has significantly enhanced the maneuverability, stability, and overall performance of the compound helicopter. Furthermore, the detailed examination of the system's behavior across the entire forward flight envelope has not only contributed to the design of the control subsystem but has also enabled a deeper understanding of the complex dynamics and aerodynamic interactions at play. This understanding can lead to further advancements in optimizing the compound helicopter's performance and enhancing its operational capabilities. It provides a solid foundation for future research and development efforts aimed at improving the control strategies and overall flight characteristics of compound rotorcraft. By presenting the research findings in a comprehensive and multi-layered manner, this study has made a substantial contribution to the field of flight dynamics and control optimization. The insights gained from the analysis and simulation of various maneuvers and trajectories have provided a valuable resource for researchers, engineers, and designers working in the domain of compound helicopter configurations. The outcomes of this research not only advance our understanding of the compound helicopter's behavior but also pave the way for future advancements in control system design, flight performance optimization, and the realization of safer, more efficient, and highly maneuverable aircraft.

Additionally, the research has delved into the importance of auxiliary lift and propulsion in expanding the flight envelope of the compound helicopter configuration. It has been established that the initial objective of achieving higher cruise speeds compared to conventional helicopters has been successfully validated. The linear reduction of the rotor's rotational velocity beyond 125 knots, down to 75% of its hover value, proves to be an effective measure in mitigating adverse effects such as drag divergence and dynamic stall. This remarkable capability enables the rotorcraft to adapt and allocate its control efforts among available controls, ensuring the attainment of the desired airspeed while maintaining stability and maneuverability. Regarding the transition phase of the flight envelope, the research findings reveal that there is no fixed predetermined pattern for the conversion corridor. Instead, a range of input combinations can be employed to gradually increase forward flight speed, with the specific weight selection influencing the approach. This flexible approach to the transition phase allows for versatility in adapting to different flight scenarios. Furthermore, the research has thoroughly addressed the challenge of over-actuation in the compound helicopter system. Recognizing that the system possesses more unknown variables than equations, resulting in an under-determined system, traditional analytical trim methods become infeasible. To overcome this limitation, numerical optimization methods have been employed. A custom mapping function has been developed, incorporating weighted penalties for undesired inputs and prioritizing smaller indices. This innovative approach has proven successful in identifying 52 operating points for forward flight speeds and their corresponding attainable moment sets.

These findings provide valuable insights into the maneuverability of the compound helicopter at each operating point, aiding in the optimization of flight control strategies and enhancing overall performance. Moreover, the adapted control mapping method introduced in this research possesses broader applicability that extends beyond the compound helicopter domain. Its potential utilization extends to similar over-actuated dynamical systems with similar objective functions, particularly within the realm of hybrid compound rotorcraft. This indicates the potential for the research findings to

make valuable contributions to the advancement of control theory and the development of efficient control strategies in various aerodynamic systems. The significance of this research extends beyond its immediate impact, as it has paved the way for a deeper understanding and optimization of flight dynamics in hybrid compound rotorcraft. The derived mathematical model, coupled with the insights garnered from stability analysis, control allocation, and simulation of diverse maneuvers, establishes a robust foundation for future investigations. It enables researchers to delve further into the intricacies of maneuvering flight, facilitating the realization of fully functional simulations for this captivating and innovative aircraft configuration. By shedding light on the complex dynamics and control challenges faced by hybrid compound rotorcraft, this research fills crucial gaps in knowledge and offers tangible solutions. It empowers engineers and designers to refine and optimize the flight control systems of such aircraft, enhancing their safety, performance, and efficiency. The findings from this research can serve as a reference and guide for future endeavors in the field of hybrid compound rotorcraft, stimulating further advancements and innovations in this exciting area of aviation.

In conclusion, this research has not only deepened our understanding of flight dynamics in hybrid compound rotorcraft but has also paved the way for future breakthroughs. Through its comprehensive analysis, the development of control strategies, and the establishment of a solid mathematical foundation, it has contributed significantly to the progress of this field. With its potential for wider applicability and its impact on control theory, this research holds great promise for the continued advancement and realization of efficient and maneuverable hybrid compound rotorcraft.

2. Recommendations

For research completeness, certain points are to be put forward in which further development would be beneficial for the field.

- It has been mentioned that the lateral cyclic is the sole control input available for roll manipulation. It is in the best interest of the model in terms of fidelity that a set of aileron surfaces are modelled at the wing. As it can be seen from the AMS surface, rolling maneuverability is around half of the other two axes. Incorporation of ailerons will improve that significantly, but will also prevent lateral cyclic saturation, which is imminent.

- In order to fulfill the flight envelope expansion capabilities it is essential that the scope be broadened towards climbing flight. It is suggested that the climb angle γ be varied in steps for a constant airspeed vector $\mathbf{V}$ initially, and that then the latter is varied for constant climb angles, while remaining within rate of climb limits, in order to have the entire flight envelope graphed and compared to that of the Eurocopter EC155.

- Regarding the inflow of the rotating components, a more sophisticated model can be implemented, most of which have been documented in the literature study of this research. Specifically, a quasi-dynamic inflow model can be advanced to a Peters-He or Pitt-Peters dynamic inflow one. Rotor and propeller performance are key to the dynamic response of this research, and could therefore be explored further in terms of fidelity.

- Vital is also the modelling of the aerodynamic interaction between components around this vehicle. In this study, this has been modelled by means of interference factors in the aerodynamic equations. However, a more complex method such as wind-tunnel data in the form of lookup tables would favor the progress. Recently, Laurianne Lefevre has conducted significant work with experimentation in rotor-propeller interaction, so research in the topic is advised ([64],[65]).

It is not effective for a study not to provide insight on how it can be used for further research, and while controlling and analyzing the model in its stability is the obvious route from here, the aforementioned discussion items are crucial in the improvement of said model.

V

Additional Information

1. Coordinate Frames

This appendix provides an overview of these reference frames and the coordinate transformations necessary to convert vector coordinates between them [66]. In the body-fixed reference frame the plane of symmetry of the vehicle contains the x-axis and the z-axis. The x-axis points towards the front of the vehicle and is aligned with the fuselage centerline, while the z-axis points downward perpendicular to the x-axis. The y-axis is defined to maintain a right-handed reference system. This coordinate system proves to be highly valuable in expressing the linear velocities (u, v, w) and angular velocities (p, q, r) of the aircraft around its three axes. Another commonly used reference frame is the North-East-Down (NED) frame, where the origin is typically attached to the vehicle's Center of Gravity (CG). The z-axis of this frame points vertically downward, aligning with the local gravity vector. The x-axis points toward the North, as observed from the vehicle's CG, while the y-axis points toward the East, establishing a right-handed coordinate system. In many applications, particularly for small distances, the orientation of this reference frame remains relatively constant with the vehicle's displacement, allowing us to neglect its rotation. This assumption simplifies the analysis of motion by disregarding the curvature of the Earth. Moreover, by considering the Earth as non-rotating, the NED frame can be treated as an inertial reference frame. However, it is important to note that this assumption holds true only for control design purposes and cannot be applied to guidance or navigation systems intended for long-distance flight.

1.1. Rotation definitions

The rotation matrices facilitate the conversion of vector coordinates between coordinate systems that are interconnected through a rotation of an arbitrary angle t around a specific axis. The resulting matrices vary depending on the axis of rotation, and are as follows:

$$
\mathscr{R}_x(t) \triangleq \begin{bmatrix} 1 & 0 & 0 \\ 0 & \cos t & \sin t \\ 0 & -\sin t & \cos t \end{bmatrix} \qquad
\mathscr{R}_y(t) \triangleq \begin{bmatrix} \cos t & 0 & -\sin t \\ 0 & 1 & 0 \\ \sin t & 0 & \cos t \end{bmatrix} \qquad
\mathscr{R}_z(t) \triangleq \begin{bmatrix} \cos t & \sin t & 0 \\ -\sin t & \cos t & 0 \\ 0 & 0 & 1 \end{bmatrix}
$$

All the transformations discussed in the subsequent sections can be decomposed into the multiplication of three fundamental matrices, which also yield orthogonal matrices.

1.2. NED to body-fixed frame transformation

The orientation of any reference frame relative to another one can be given by a sequence of three angles that describes the required rotations so that one frame is transformed into the other. These three angles are generally known as Euler angles and twelve different sequences exist to describe the referred transformation unambiguously. In flight dynamics, one of the most common sequences is defined as follows: first a rotation of the yaw angle ψ about the z-axis, then a rotation of the pitch angle ϑ about the intermediate y-axis and finally a rotation of the roll angle φ about the intermediate x-axis.
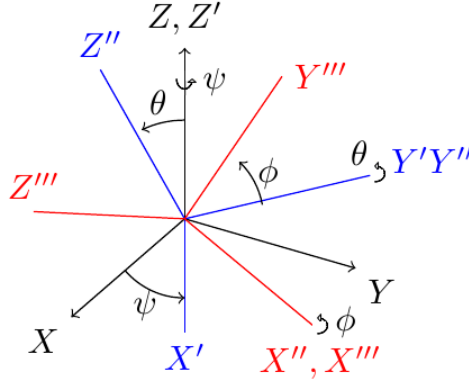
Figure V.1: Euler angles [67]

According to this, the transformation from the NED to the body-fixed reference frame

$$\mathcal{T}_n^b(\varphi, \vartheta, \psi) = \mathcal{R}_x(\varphi)\mathcal{R}_y(\vartheta)\mathcal{R}_z(\psi) = \begin{bmatrix} \cos\psi\cos\vartheta & \sin\psi\cos\vartheta & -\sin\vartheta \\ \cos\psi\sin\vartheta\sin\varphi - \sin\psi\cos\varphi & \sin\psi\sin\vartheta\sin\varphi + \cos\psi\cos\varphi & \cos\vartheta\sin\varphi \\ \cos\psi\sin\vartheta\cos\varphi + \sin\psi\sin\varphi & \sin\psi\sin\vartheta\cos\varphi - \cos\psi\sin\varphi & \cos\vartheta\cos\varphi \end{bmatrix}$$

1.3. NED to velocity frame transformation

Similarly to the previous scenario, a sequence of rotations can be defined to convert NED coordinates into the velocity reference frame. This conversion requires two angles: the flight path angle γ and the heading χ. The flight path angle represents the angle between the velocity vector and the local horizon, which is a plane perpendicular to the local gravity vector. On the other hand, the heading angle is the angle between the velocity vector and the North direction. The relationship between the three aforementioned coordinate frames is visible in Figure V.2
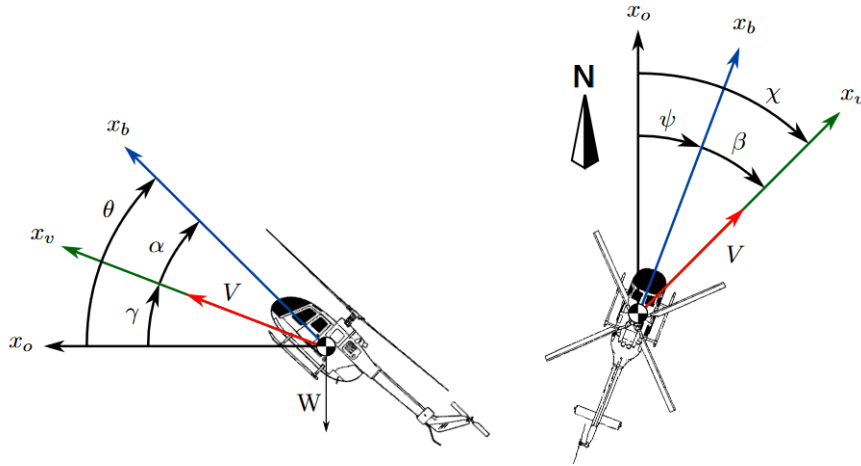
Figure V.2: NED, body, and velocity frames x-axis from portside view (left) and top view (right)

Furthermore, it can be observed that when the fuselage centerline aligns with the velocity vector, the pitch of the aircraft corresponds to the flight path angle, and the yaw angle aligns with the heading. In a broader context, two additional angles can be defined to describe the relationship between the body-fixed frame and the velocity reference frame: the angle of attack ($\alpha = \vartheta - \gamma$) and the sideslip angle ($\beta = \chi - \psi$). The angle of attack represents the difference between the pitch angle (ϑ) and the flight path angle (γ), while the sideslip angle represents the difference between the heading angle (χ) and the yaw angle (ψ). The transformation between the NED frame and the velocity frame is shown below:

$$\mathcal{T}_n^v(\gamma, \chi) = \begin{bmatrix} \cos\chi\cos\gamma & \sin\chi\cos\gamma & -\sin\gamma \\ -\sin\chi & \cos\chi & 0 \\ \cos\chi\sin\gamma & \sin\chi\sin\gamma & \cos\gamma \end{bmatrix}$$

2. Flapping angles
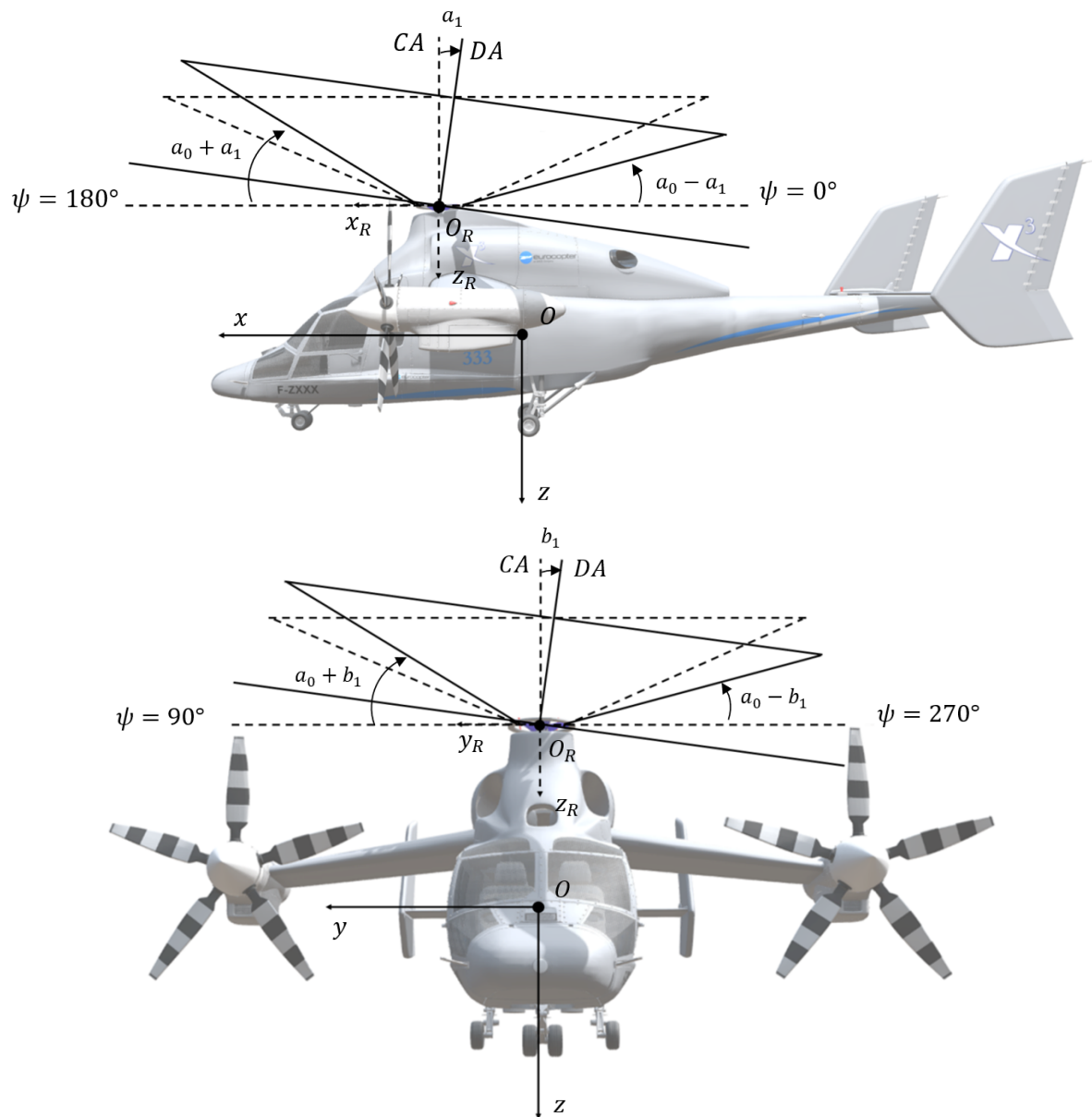
Figure V.4: Moment arms from top view

3. Moment arms
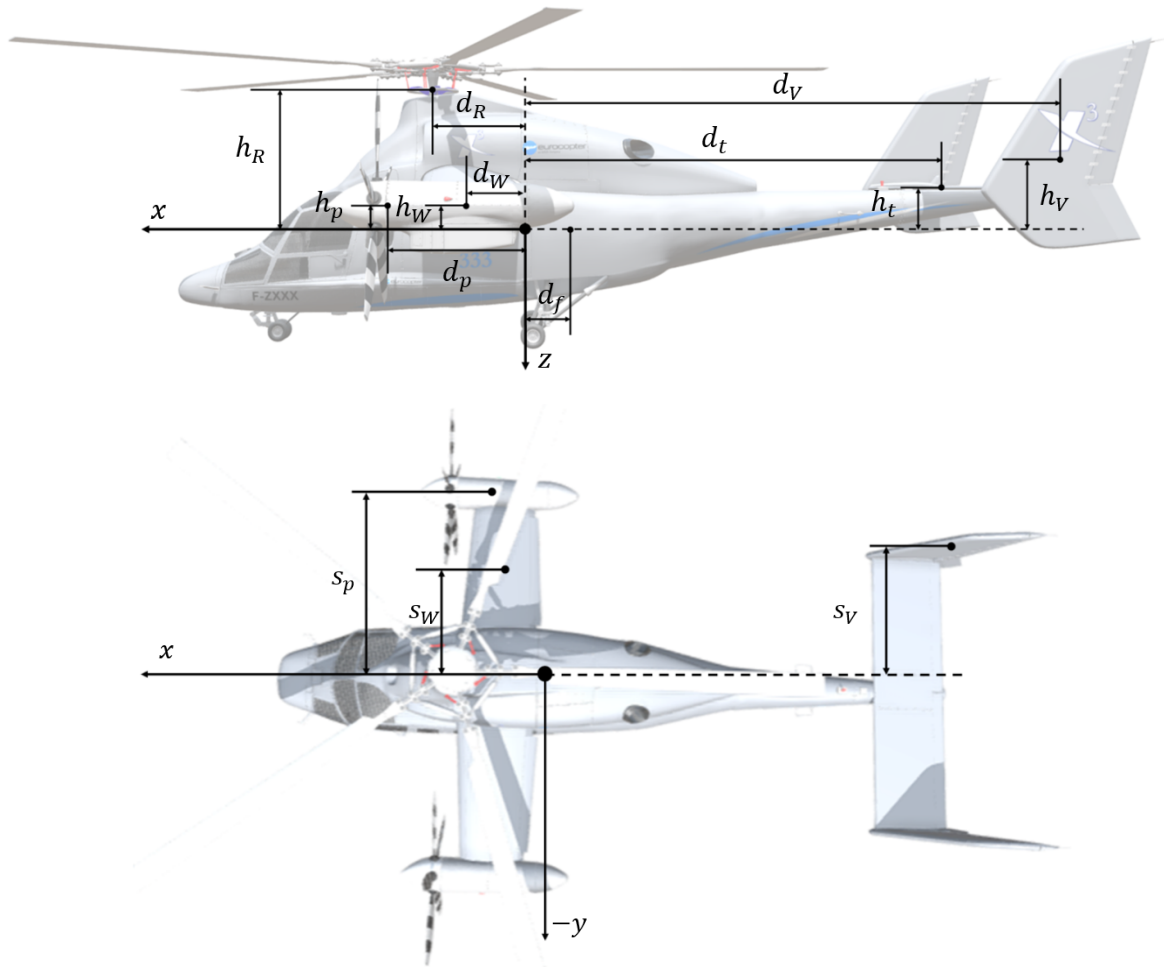
Figure V.6: Moment arms from top view

Table V.1: Moment arms

Parameter	Symbol	Value	Unit
Rotor x-arm	d_R	1.12	m
Rotor z-arm	h_R	1.7	m
CG y-offset	s_{off}	0.03	m
Propeller x-arm	d_p	1.66	m
Propeller z-arm	h_p	0.28	m
Mean propeller y-arm	s_p	2.38	m
Wing x-arm	d_w	0.73	m
Wing z-arm	h_w	0.3	m
Horizontal tail x-arm	d_t	5.10	m
Vertical tail x-arm	d_v	6.58	m
Vertical tail z-arm	h_v	0.88	m

4. Rotor disc Mach number distribution

In this section, the avoidance of compressibility effects is portrayed. Initially, the Mach number distribution is shown across the rotor disc for a constant rotational velocity Ω, and afterward, the effect of reducing this speed linearly can be seen.
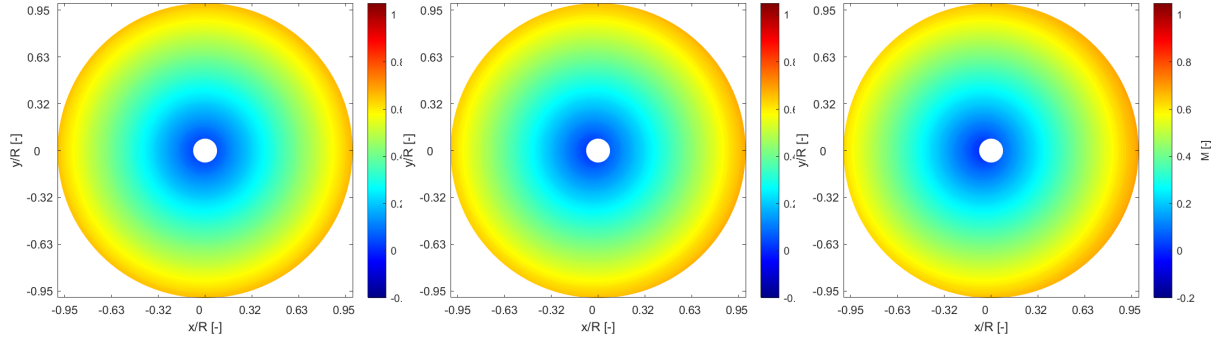
Figure V.7: Hover   **Figure V.8:** u = 10kts   **Figure V.9:** u = 20kts
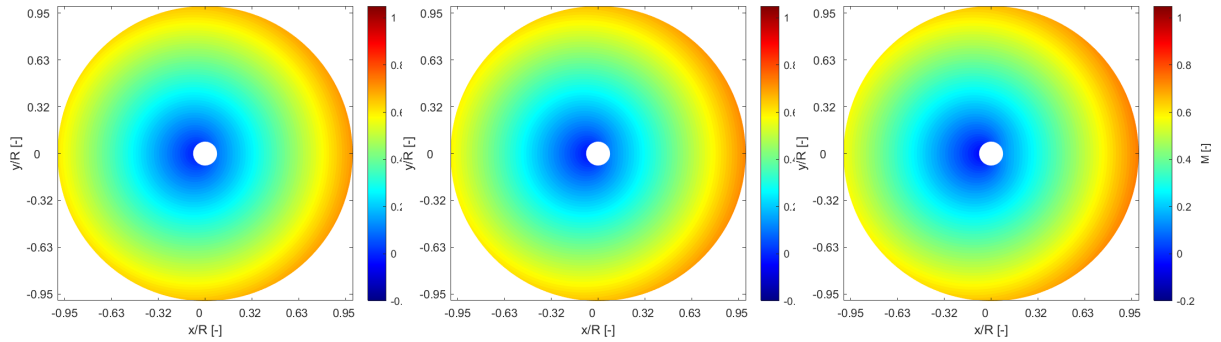
Figure V.10: u = 30kts   **Figure V.11:** u = 40kts   **Figure V.12:** u = 50kts
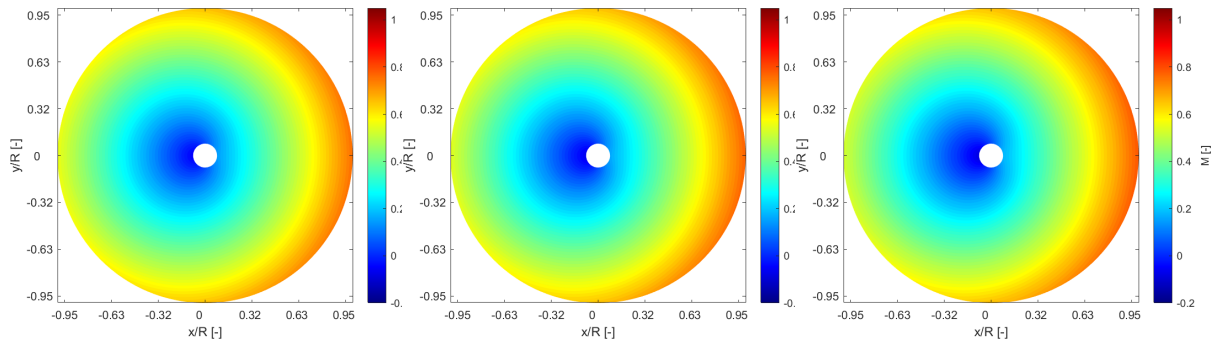
Figure V.13: u = 60kts   **Figure V.14:** u = 70kts   **Figure V.15:** u = 80kts
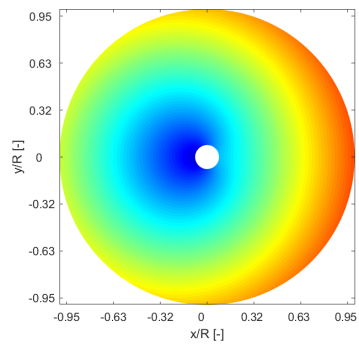
Figure V.16: u = 90kts
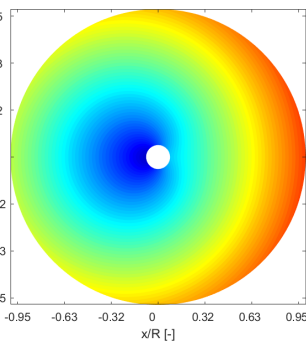
Figure V.17: u = 100kts
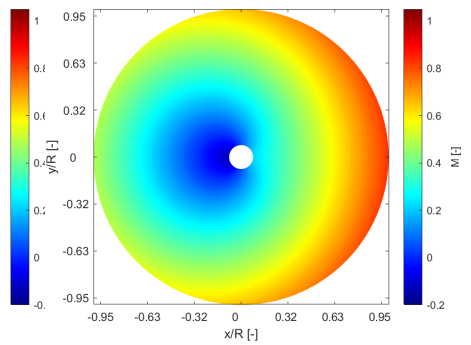
Figure V.18: u = 110kts
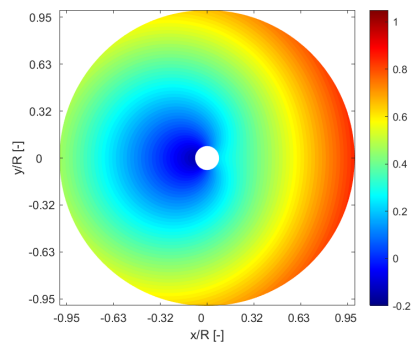
Figure V.19: u = 120kts

From this airspeed onward, the rotational velocity of the rotor is reduced linearly, as has been explained, in order to avoid compressibility effects at the advancing side. The following plots compare the Mach number distribution across the rotor disc, firstly if this measure had not been taken, and next the new one.
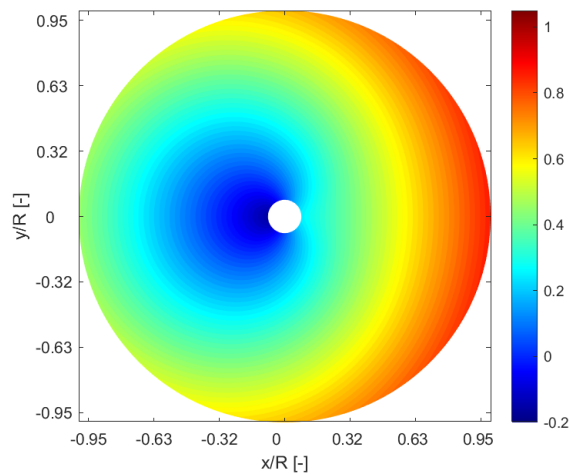
Figure V.20: u = 130kts before RPM reduction
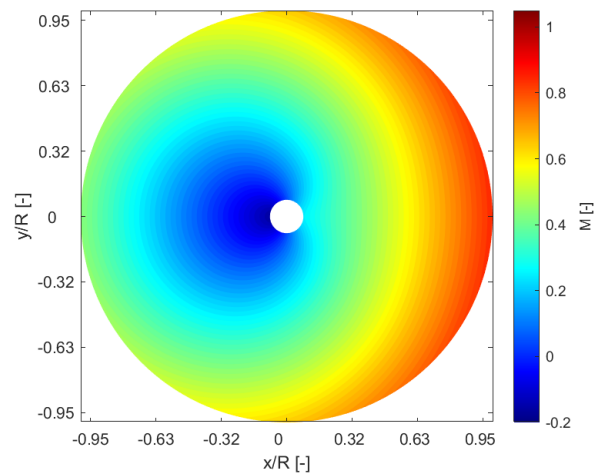
Figure V.21: u = 130kts after RPM reduction
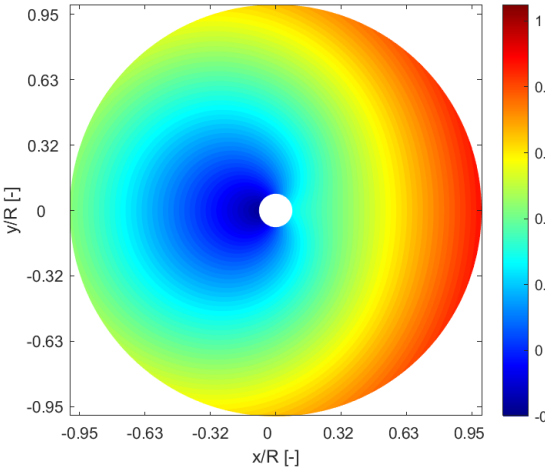
Figure V.22: u = 140kts before RPM reduction
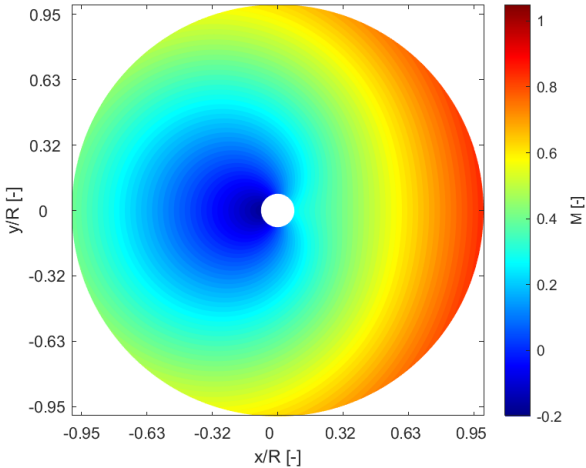
Figure V.23: u = 140kts after RPM reduction
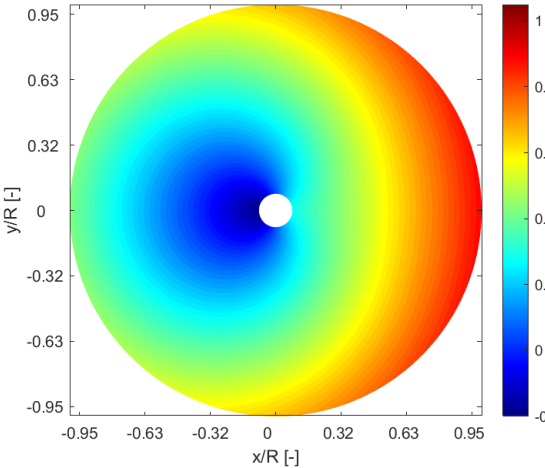
Figure V.24: u = 150kts before RPM reduction
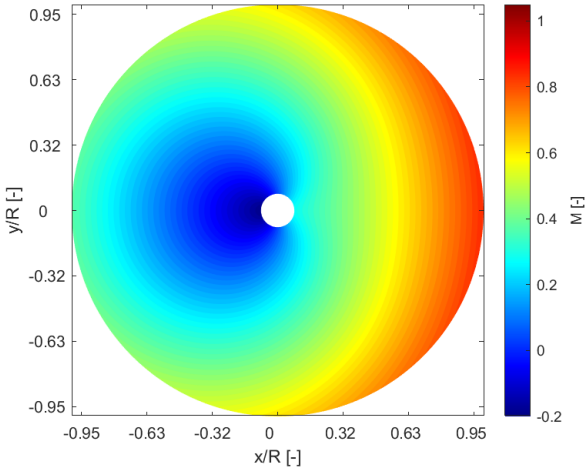
Figure V.25: u = 150kts after RPM reduction
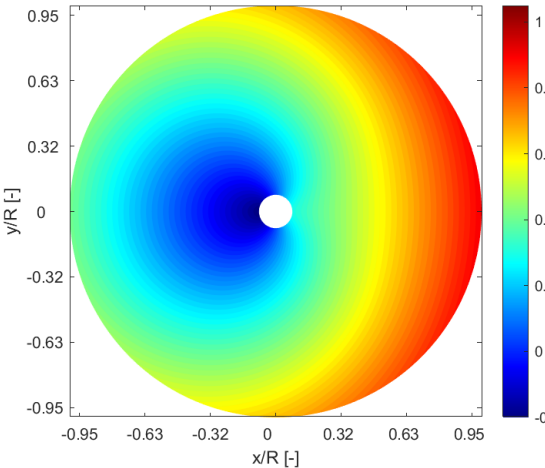
Figure V.26: u = 160kts before RPM reduction
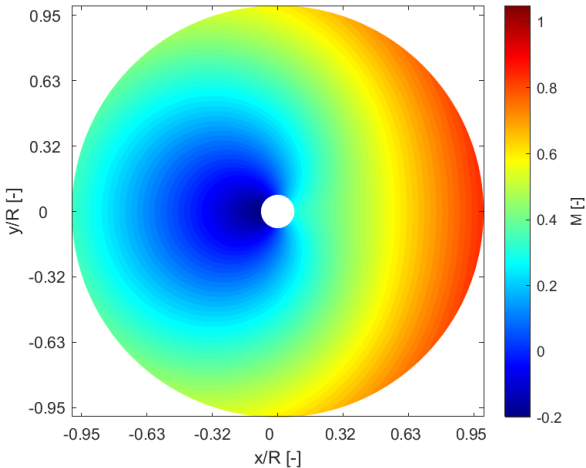
Figure V.27: u = 160kts after RPM reduction
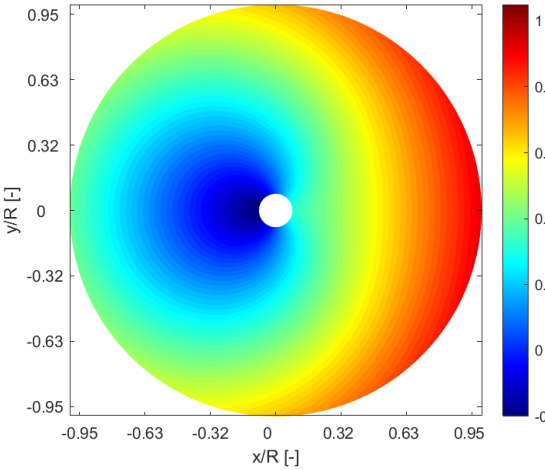
Figure V.28: u = 170kts before RPM reduction
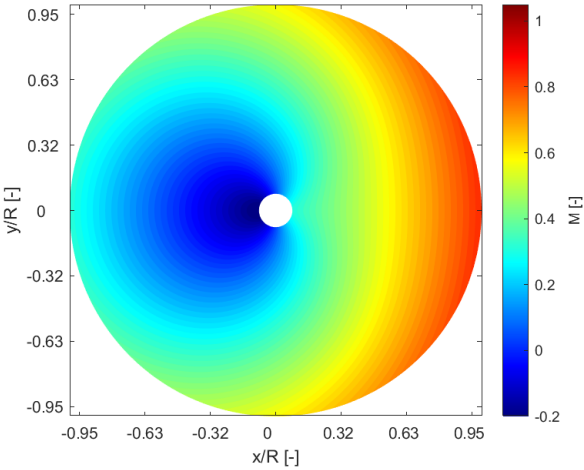
Figure V.29: u = 170kts after RPM reduction
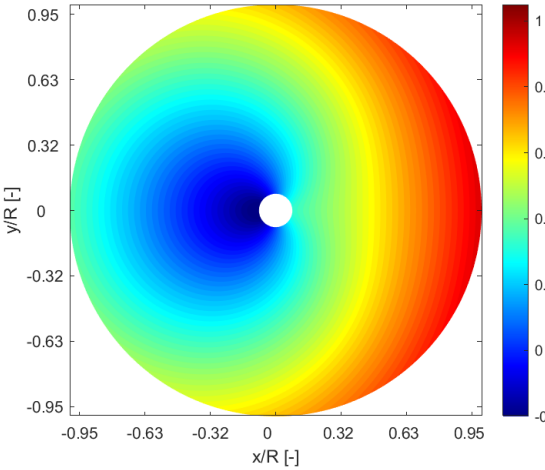
Figure V.30: u = 180kts before RPM reduction
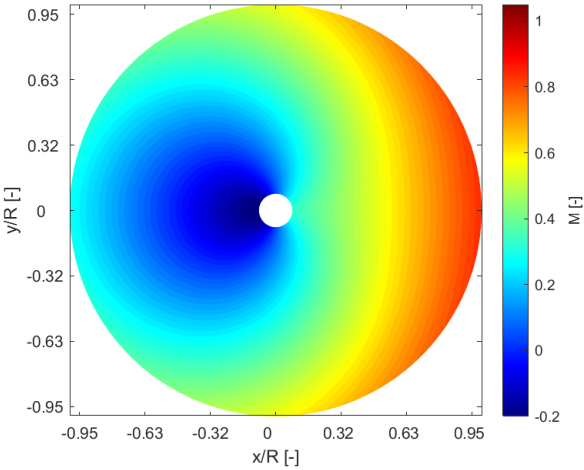
Figure V.31: u = 180kts after RPM reduction
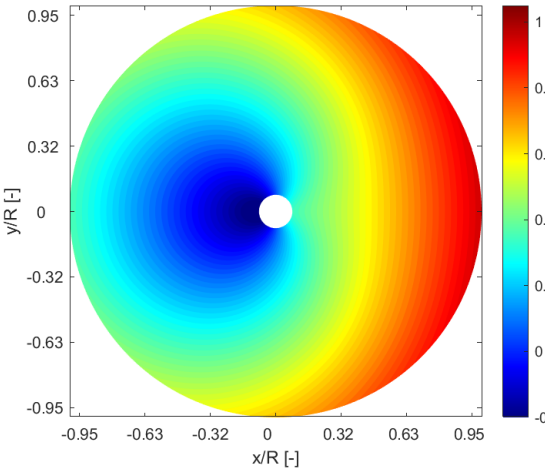
Figure V.32: u = 190kts before RPM reduction
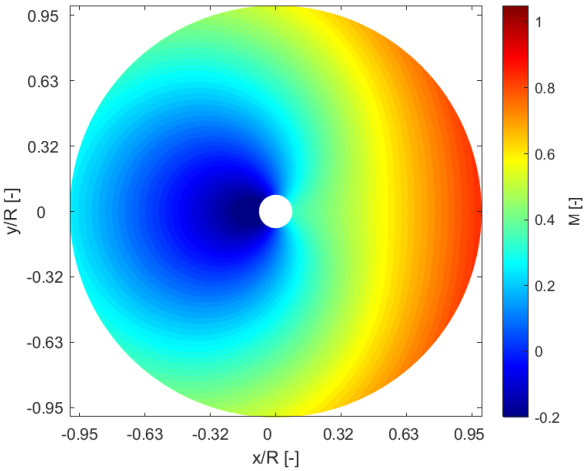
Figure V.33: u = 190kts after RPM reduction
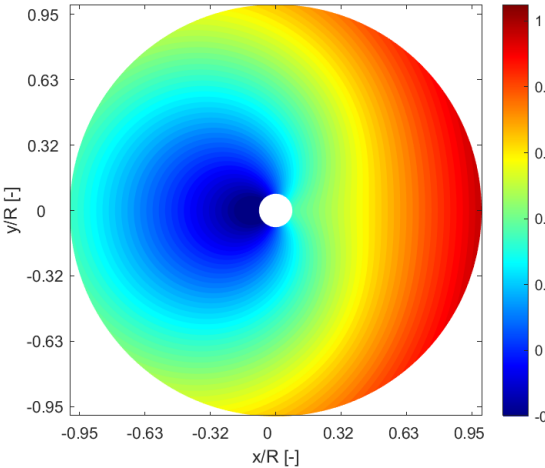
Figure V.34: u = 200kts before RPM reduction
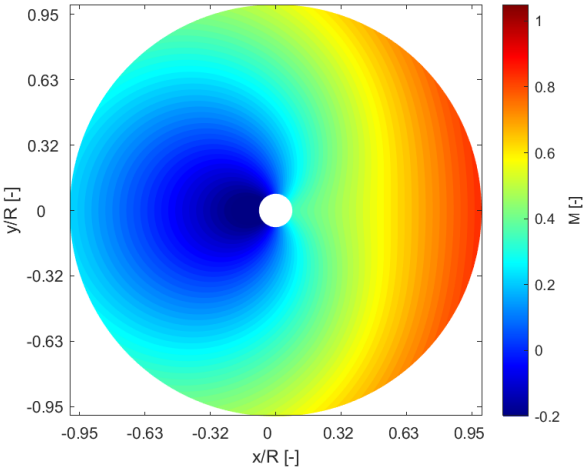
Figure V.35: u = 200kts after RPM reduction
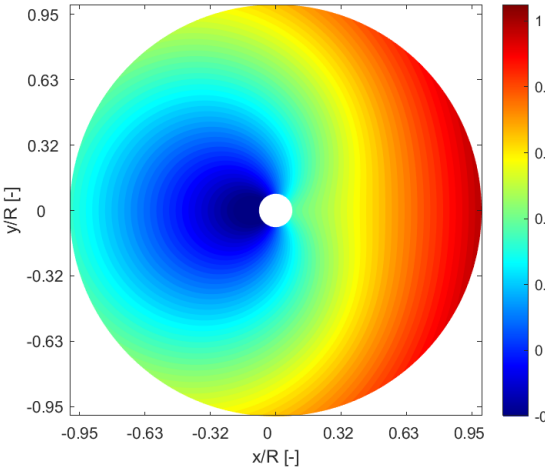
Figure V.36: u = 210kts before RPM reduction
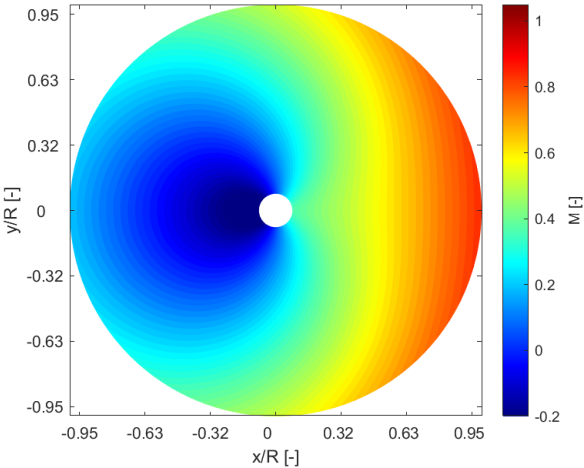
Figure V.37: u = 210kts after RPM reduction
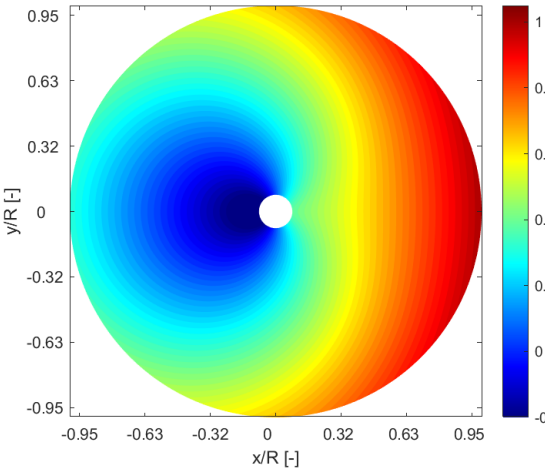
Figure V.38: u = 220kts before RPM reduction
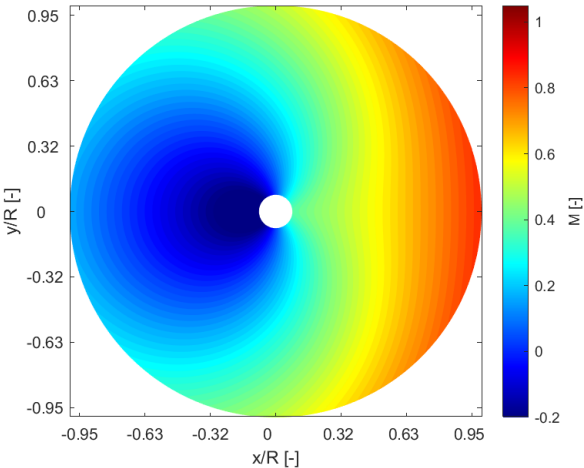
Figure V.39: u = 220kts after RPM reduction
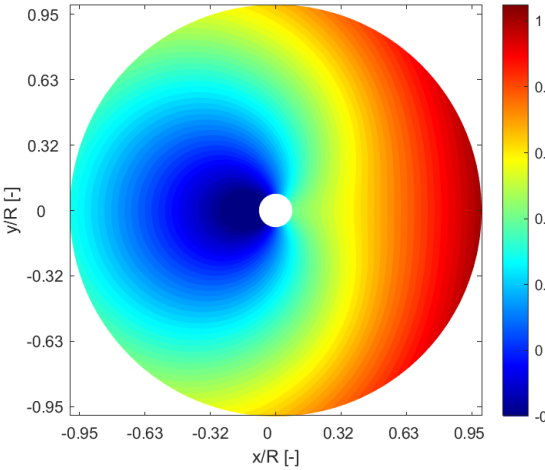
Figure V.40: u = 230kts before RPM reduction
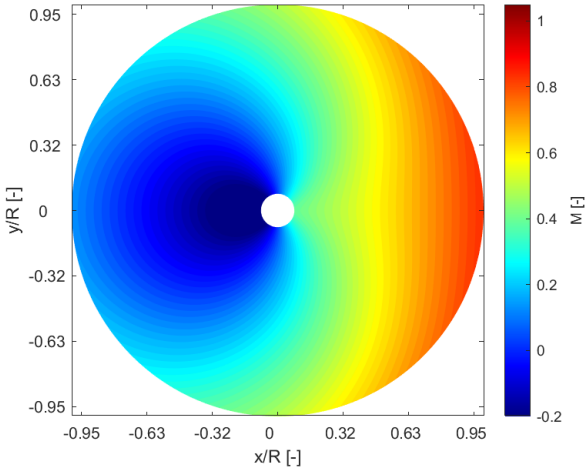
Figure V.41: u = 230kts after RPM reduction
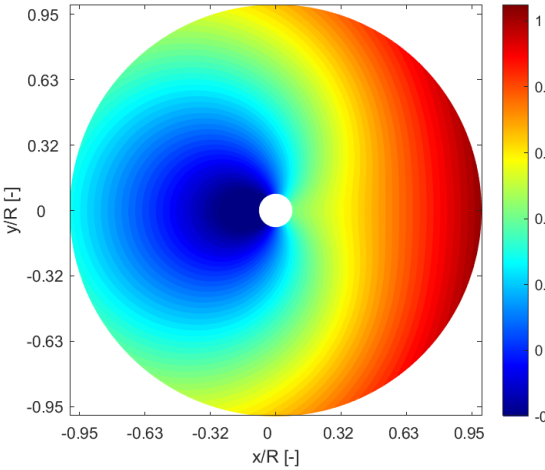
Figure V.42: u = 240kts before RPM reduction
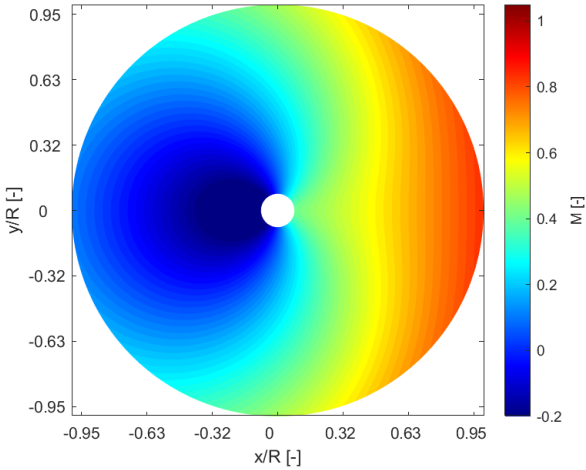
Figure V.43: u = 240kts after RPM reduction
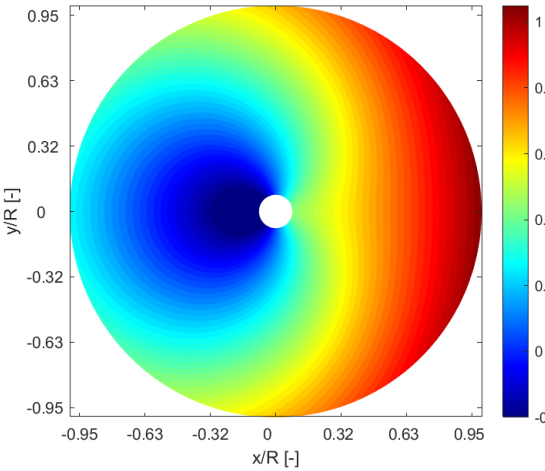
Figure V.44: u = 250kts before RPM reduction
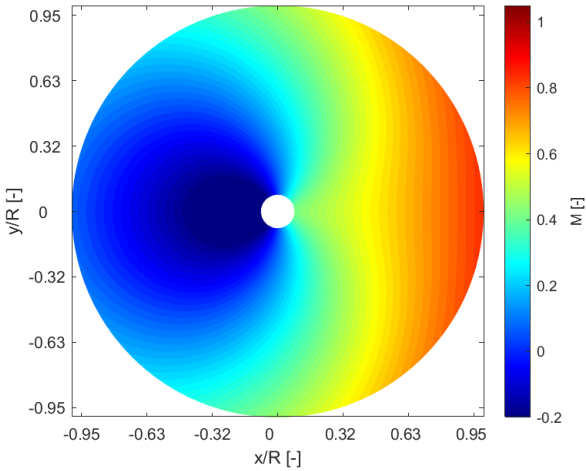
Figure V.45: u = 250kts after RPM reduction

5. **Allocated control effort**

This section includes all spider plots of the allocated control effort, that lead to the desired operating points from hover until maximum speed.
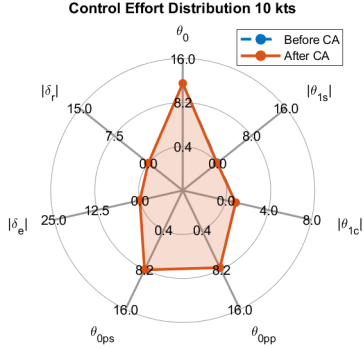
Figure V.46: u = 10kts
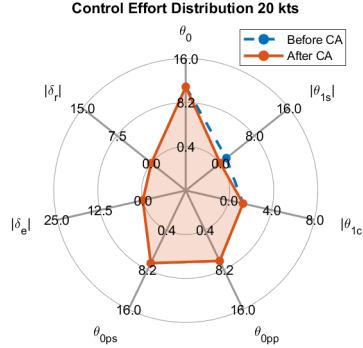
Figure V.47: u = 20kts
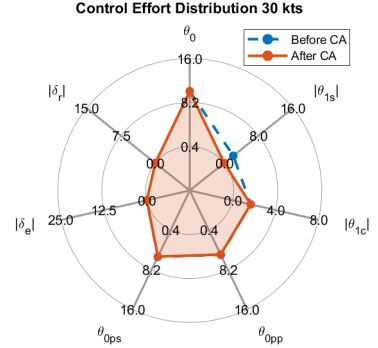
Figure V.48: u = 30kts
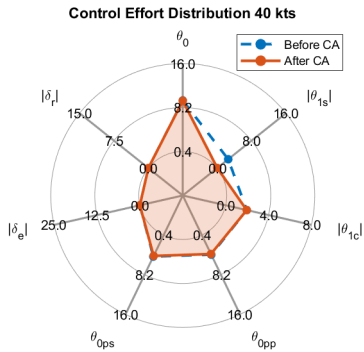
Figure V.49: u = 40kts
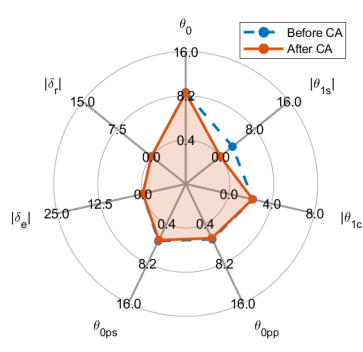
Figure V.50: u = 50kts
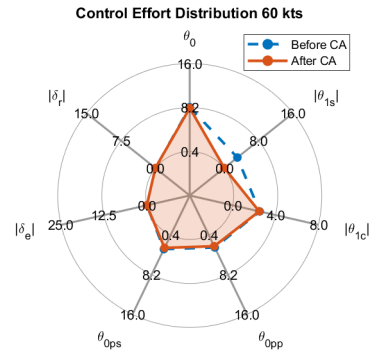
Figure V.51: u = 60kts
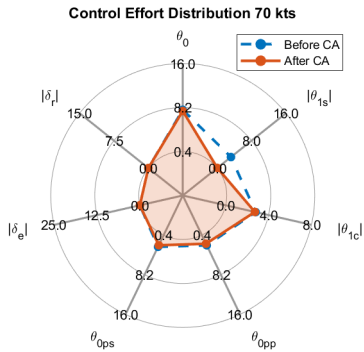
Figure V.52: u = 70kts
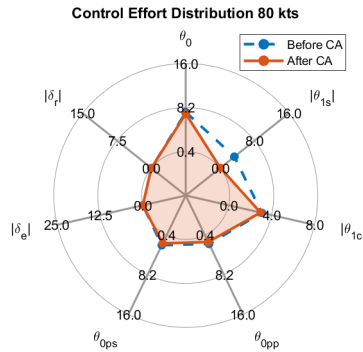
Figure V.53: u = 80kts
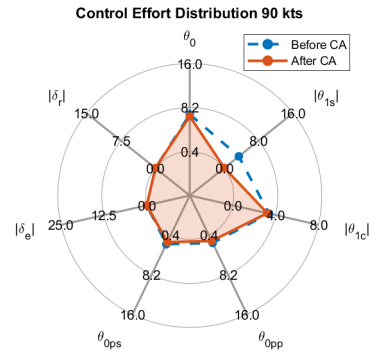
Figure V.54: u = 90kts

Figure V.55: u = 100kts

Figure V.56: u = 110kts

Figure V.57: u = 120kts

Figure V.58: u = 130kts

Figure V.59: u = 140kts

Figure V.60: u = 160kts

Figure V.61: u = 170kts

Figure V.62: u = 180kts

Figure V.63: u = 190kts

Figure V.64: u = 200kts

Figure V.65: u = 210kts

Figure V.66: u = 220kts
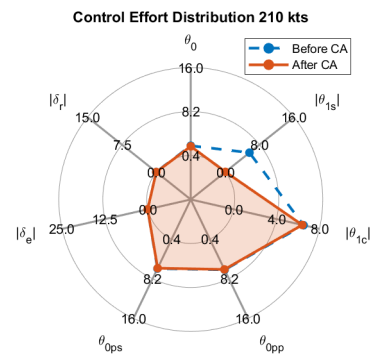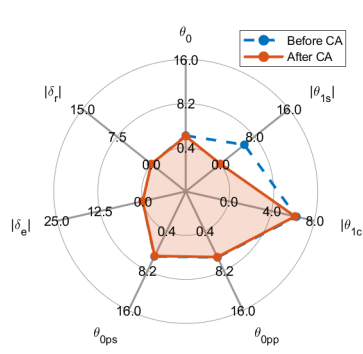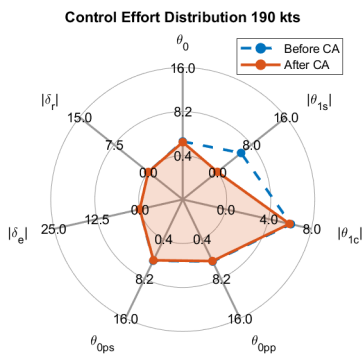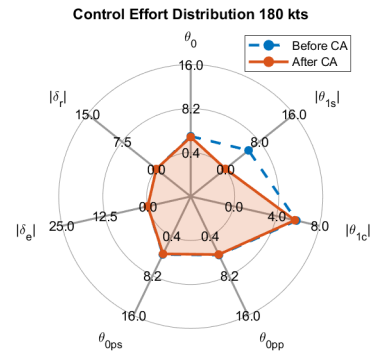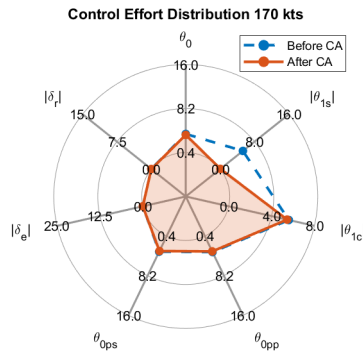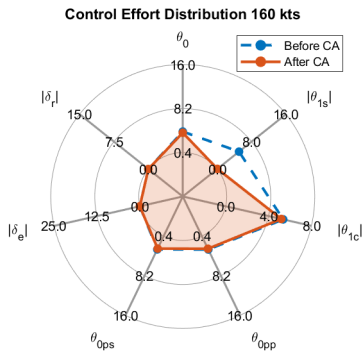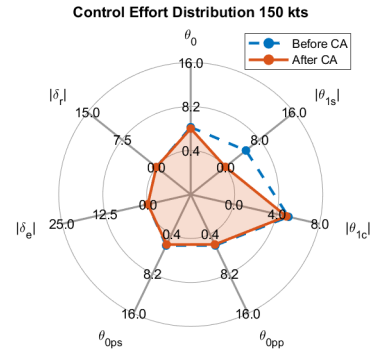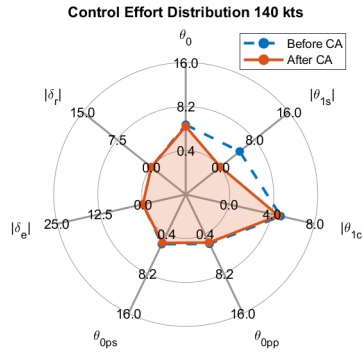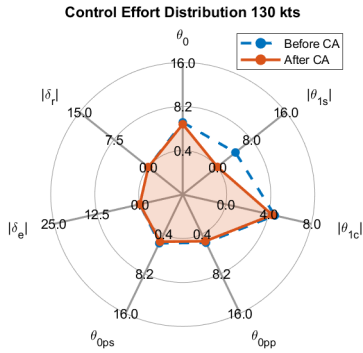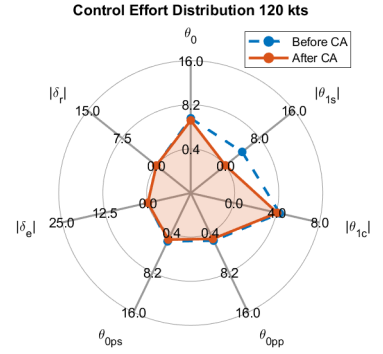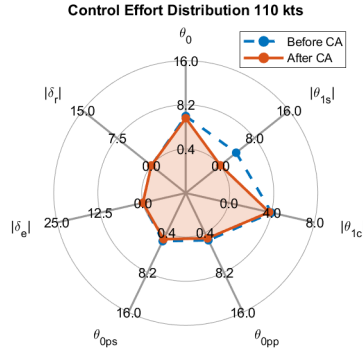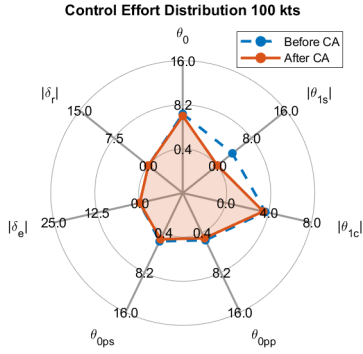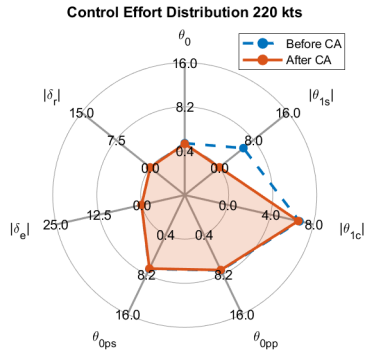
Figure V.67: u = 230kts
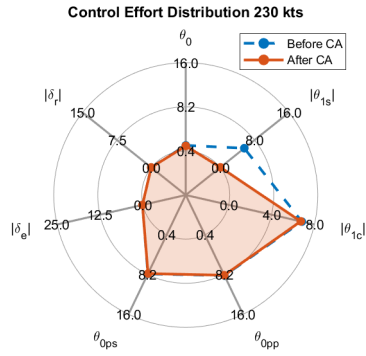
Figure V.68: u = 240kts
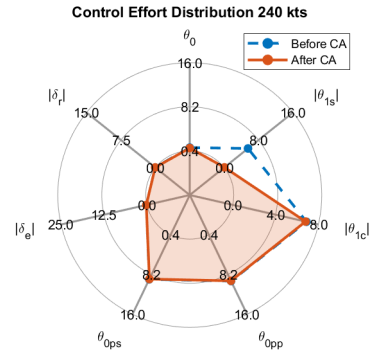
Figure V.69: u = 250kts
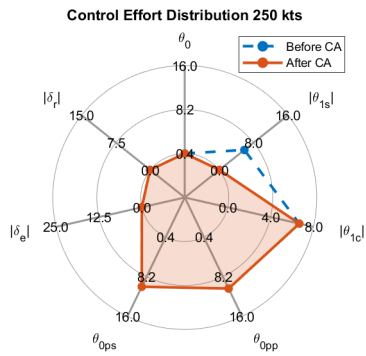
Figure V.70: u = 250kts
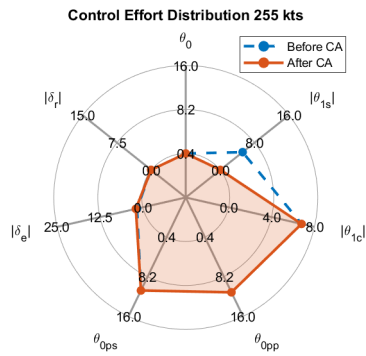
Figure V.71: u = 255kts

Bibliography

[1]   R. B. Lightfoot, "The helicopter as a competitive transport vehicle," *Journal of the American Helicopter Society*, vol. 5, no. 3, pp. 3–11, Jul. 1, 1960, ISSN: 2161-6027. (visited on 06/06/2022).

[2]   J. Thiemeier, C. Öhrle, F. Frey, M. Keßler, and E. Krämer, "Aerodynamics and flight mechanics analysis of airbus helicopters' compound helicopter RACER in hover under crosswind conditions," *CEAS Aeronautical Journal*, vol. 11, no. 1, pp. 49–66, Jan. 2020, ISSN: 1869-5582, 1869-5590. (visited on 07/07/2022).

[3]   D. N. Meyers, L. Tompkins, and J. H. Goldberg, "16h-1a flight test research program," 1968.

[4]   D. SEGNER, "Xh-51a compound helicopter design and development. xh-51a compound helicopter design and development," in *Aircraft Design and Technology Meeting*. DOI: `10.2514/6.1965-757`. eprint: `https://arc.aiaa.org/doi/pdf/10.2514/6.1965-757`. [Online]. Available: `https://arc.aiaa.org/doi/abs/10.2514/6.1965-757`.

[5]   J. N. Johnson, G. L. Bender, R. D. McClellan, J. R. Burden, and M. E. Larsen, "Attack Helicopter Evaluation AH-56A Cheyenne Compound Helicopter:" en, Defense Technical Information Center, Fort Belvoir, VA, Tech. Rep., Jun. 1972. DOI: `10.21236/AD0771914`. [Online]. Available: `http://www.dtic.mil/docs/citations/AD0771914` (visited on 07/06/2022).

[6]   M. Orchard and S. Newman, "The fundamental configuration and design of the compound helicopter," *Proceedings of the Institution of Mechanical Engineers, Part G: Journal of Aerospace Engineering*, vol. 217, no. 6, pp. 297–315, Jun. 1, 2003, ISSN: 0954-4100, 2041-3025. DOI: `10.1243/095441003772538570`. [Online]. Available: `http://journals.sagepub.com/doi/10.1243/095441003772538570` (visited on 06/16/2022).

[7]   G. T. Ozdemir, J. F. Horn, and A. T. Thorsen, "In-flight multi-variable optimization of redundant controls on a compound rotorcraft," in *AIAA Guidance, Navigation, and Control (GNC) Conference*, Boston, MA: American Institute of Aeronautics and Astronautics, Aug. 19, 2013, ISBN: 978-1-62410-224-0. DOI: `10.2514/6.2013-5165`. [Online]. Available: `https://arc.aiaa.org/doi/10.2514/6.2013-5165` (visited on 08/03/2022).

[8]   T. Berger, M. B. Tischler, and J. F. Horn, "Outer-loop control design and simulation handling qualities assessment for a coaxial-compound helicopter and tiltrotor," p. 33,

[9]   E. Solis, T. A. Bass, M. D. Keith, R. T. Oppenheim, B. T. Runyon, and B. Veras-Alba, "Rotcfd analysis of the ah-56 cheyenne hub drag," Tech. Rep., 2016.

[10] A. T. Thorsen, "A unified flight control methodology for a compound rotorcraft in fundamental and aerobatic maneuvering flight," 2016.

[11] A. T. Thorsen, "Assessment of control allocation optimization on performance and dynamic response enhancement of a compound rotorcraft," 2014.

[12] H. Yeo, "Design and aeromechanics investigation of compound helicopters," *Aerospace Science and Technology*, vol. 88, pp. 158–173, 2019, ISSN: 1270-9638. DOI: `https://doi.org/10.1016/j.ast.2019.03.010`. [Online]. Available: `https://www.sciencedirect.com/science/article/pii/S1270963818326579`.

[13] M. Scully, "Adventures in low disc loading vtol design," Tech. Rep., 2018.

[14] M. Şenipek, "Development of an object-oriented design, analysis and simulation software for a generic air vehicle," Ph.D. dissertation, Sep. 2017. DOI: `10.13140/RG.2.2.24882.15042`.

[15] K. Ferguson and D. Thomson, "Performance comparison between a conventional helicopter and compound helicopter configurations," *Proceedings of the Institution of Mechanical Engineers, Part G: Journal of Aerospace Engineering*, vol. 229, no. 13, pp. 2441–2456, Nov. 2015, ISSN: 0954-4100, 2041-3025. DOI: `10.1177/0954410015577997`. [Online]. Available: `http://journals.sagepub.com/doi/10.1177/0954410015577997` (visited on 09/11/2022).

[16] Y. Kelong, H. Dong, and S. Qipeng, "Study on the lift and propulsive force shares to improve the flight performance of a compound helicopter," *Chinese Journal of Aeronautics*, vol. 35, no. 1, pp. 365–375, 2022.

[17] P. V. M. Simplıcio, "Helicopter nonlinear flight control," 2011.

[18] K. H. Hohenemser, "Hingeless rotorcraft flight dynamics," 1974.

[19] A. R. S. Bramwell, D. Balmford, and G. Done, *Bramwell's helicopter dynamics*. Elsevier, 2001.

[20] R. W. Prouty and H. Curtiss Jr, "Helicopter control systems: A history," *Journal of Guidance, Control, and Dynamics*, vol. 26, no. 1, pp. 12–18, 2003.

[21] E. H. Dowell and D. Tang, "Nonlinear aeroelasticity and unsteady aerodynamics," *AIAA journal*, vol. 40, no. 9, pp. 1697–1707, 2002.

[22] W. Johnson, "Assessment of aerodynamic and dynamic models in a comprehensive analysis for rotorcraft," *Computers & mathematics with applications*, vol. 12, no. 1, pp. 11–28, 1986.

[23] K. B. Hilbert, "A mathematical model of the uh-60 helicopter," Tech. Rep., 1984.

[24] J. D. Phillips, "Mathematical model of the sh-3g helicopter," Tech. Rep., 1982.

[25] J. M. Weber, T. Y. Liu, and W. Chung, "A mathematical simulation model of the ch-47b helicopter, volume 2," Tech. Rep., 1984.

[26] R. T. Chen, "Effects of primary rotor parameters on flapping dynamics," Tech. Rep., 1980.

[27] J. J. Howlett, "Uh-60a black hawk engineering simulation program. volume 1: Mathematical model," Tech. Rep., 1981.

[28] B. Lee and M. Benedict, "Development and validation of a comprehensive helicopter flight dynamics code," in *AIAA Scitech 2020 Forum*, 2020, p. 1644.

[29] P. F. Sheridan, C. Robinson, J. Shaw, and F. White, "Math modeling for helicopter simulation of low speed, low altitude and steeply descending flight," NASA. Ames Research Center, Tech. Rep., 1982.

[30] W. Johnson, "Camrad ii, comprehensive analytical model of rotorcraft aerodynamics and dynamics," *Johnson Aeronautics, Palo Alto, California*, vol. 1999, 1992.

[31] R. K. Heffley and M. A. Mnich, "Minimum-complexity helicopter simulation math model," Tech. Rep., 1988.

[32] J. E. Bailey, R. K. Prasanth, and K. Krishnakumar, *ARMCOP Helicopter Flight and Engine Model for the UH-1 TRS Simulator*. University of Alabama, College of Engineering, Bureau of Engineering Research, 1991.

[33] M. G. Ballin, "Validation of a real-time engineering simulation of the uh-60a helicopter," Tech. Rep., 1987.

[34] S. Sarathy and V. Murthy, "An advanced rotorcraft flight simulation model-parallel implementation and performance analysis," in *Flight Simulation and Technologies*, 1993, p. 3550.

[35] F. D. Kim, R. Celi, and M. B. Tischler, "High-order state space simulation models of helicopter flight mechanics," *Journal of the American Helicopter Society*, vol. 38, no. 4, pp. 16–27, 1993.

[36] R. T. Chen, J. V. Lebacqz, E. W. Aiken, and M. B. Tischler, "Helicopter mathematical models and control law development for handling qualities research," *NASA, Washington, NASA (Army Rotorcraft Technology. Volume 2: Material and Structures, Propulsion and Drive Systems, Flight Dynamics and Control, and Acoustics*, 1988.

[37] M. S. Lewis, "A piloted simulation of one-on-one helicopter air combat in low level flight," *Journal of the American Helicopter Society*, vol. 31, no. 2, pp. 19–26, 1986.

[38] C. He and W. LEWIS, "A parametric study of real time mathematical modeling incorporating dynamic wake and elastic blades," in *AHS, Annual Forum, 48 th, Washington*, 1992, pp. 1181–1196.

[39] P. D. Talbot, *A mathematical force and moment model of a uh-1h helicopter for flight dynamics simulations*. National Aeronautics and Space Administration, 1977, vol. 73.

[40] M. WHORTON, "Uh-60 flight data replay and refly system state estimator analysis," in *AIAA, Aerospace Sciences Meeting, 28 th, Reno, NV*, 1990, p. 1990.

[41] R. Chen, Y. Yuan, and D. Thomson, "A review of mathematical modelling techniques for advanced rotorcraft configurations," *Progress in Aerospace Sciences*, vol. 120, p. 100 681, Jan. 2021, ISSN: 03760421. DOI: `10.1016/j.paerosci.2020.100681`. [Online]. Available: `https://linkinghub.elsevier.com/retrieve/pii/S0376042120300932` (visited on 08/06/2022).

[42] C. Fegely, O. Juhasz, H. Xin, and M. B. Tischler, "Flight dynamics and control modeling with system identification validation of the sikorsky x2 technology demonstrator," p. 14, 2016.

[43] D. Sagan, P. Krishnamurthy, M. Lau, J. Augustine, and B. German, "Trim of over-actuator VTOL aircraft in transition," in *AIAA AVIATION 2021 FORUM*, VIRTUAL EVENT: American Institute of Aeronautics and Astronautics, Aug. 2, 2021, ISBN: 978-1-62410-610-1. DOI: `10.2514/6.2021-3216`. [Online]. Available: `https://arc.aiaa.org/doi/10.2514/6.2021-3216` (visited on 09/16/2022).

[44] L. Lin, X. Liu, M. Peng, and J. Li, "Research on Flight Dynamic Modeling and Interference of Components for Rotor/Wing Compound Helicopter," in *The Proceedings of the 2018 Asia-Pacific International Symposium on Aerospace Technology (APISAT 2018)*, X. Zhang, Ed., Series Title: Lecture Notes in Electrical Engineering, Singapore: Springer Singapore, 2019, pp. 1202–1221. DOI: `10.1007/978-981-13-3305-7_95`. (visited on 09/15/2022).

[45] Y. Cao, M. Wang, and G. Li, "Flight dynamics modeling, trim, stability, and controllability of coaxial compound helicopters," *Journal of Aerospace Engineering*, vol. 34, no. 6, p. 04 021 084, Nov. 2021, ISSN: 0893-1321, 1943-5525. DOI: `10.1061/(ASCE)AS.1943-5525.0001342`. [Online]. Available: `https://ascelibrary.org/doi/10.1061/%28ASCE%29AS.1943-5525.0001342` (visited on 09/12/2022).

[46] K. Ferguson and D. Thomson, "Maneuverability assessment of a compound helicopter configuration," *Journal of the American Helicopter Society*, vol. 61, no. 1, pp. 1–15, Jan. 1, 2016, ISSN: 21616027. DOI: `10.4050/JAHS.61.012008`. [Online]. Available: `http://openurl.ingenta.com/content/xref?genre=article&issn=2161-6027&volume=61&issue=1&spage=1&lpage=15&aulast=Ferguson` (visited on 06/18/2022).

[47] K. Ferguson and D. Thomson, "Examining the stability derivatives of a compound helicopter," *The Aeronautical Journal*, vol. 121, no. 1235, pp. 1–20, Jan. 2017, ISSN: 0001-9240, 2059-6464. DOI: `10.1017/aer.2016.101`. [Online]. Available: `https://www.cambridge.org/core/product/identifier/S0001924016001019/type/journal_article` (visited on 08/06/2022).

[48] G. de Matteis, L. M. de Socio, and A. Leonessa, "Solution of aircraft inverse problems by local optimization," *Journal of Guidance, Control, and Dynamics*, vol. 18, no. 3, pp. 567–571, May 1995, ISSN: 0731-5090, 1533-3884. DOI: `10.2514/3.21424`. [Online]. Available: `https://arc.aiaa.org/doi/10.2514/3.21424` (visited on 08/11/2022).

[49] T. A. Johansen and T. I. Fossen, "Control allocation—a survey," *Automatica*, vol. 49, no. 5, pp. 1087–1103, 2013.

[50] W. C. Durham, J. G. Bolling, and K. A. Bordignon, "Minimum drag control allocation," *Journal of Guidance, Control, and Dynamics*, vol. 20, no. 1, pp. 190–193, 1997.

[51] A. Stolk and C. de Visser, "Minimum drag control allocation for the innovative control effector aircraft," Ph.D. dissertation, Delft University of Technology Delft, The Netherlands, 2017.

[52] S. A. Frost, M. Bodson, J. J. Burken, C. V. Jutte, B. R. Taylor, and K. V. Trinh, "Flight control with optimal control allocation incorporating structural load feedback," *Journal of Aerospace Information Systems*, vol. 12, no. 12, pp. 825–834, 2015.

[53] T. Berger, M. B. Tischler, and J. F. Horn, "Outer-Loop Control Design and Simulation Handling Qualities Assessment for a Coaxial-Compound Helicopter and Tiltrotor," en, p. 33,

[54] M. Pavel, "SIX DEGREES OF FREEDOM L1NEAR MODEL FOR HELICOPTER TRIM AND STABILITY CALCULATION," en, p. 81,

[55] T. van Holten, J. Melkert, and F. o. A. E. Delft University of Technology, *Helicopter Performance Stability and Control: Ae4-213*. TU Delft, 2002. [Online]. Available: `https://books.google.nl/books?id=kl9dnQEACAAJ`.

[56] W. Wang, D. Li, and C. Liu, "Helicopter flight simulation trim in the coordinated turn with the hybrid genetic algorithm," *Proceedings of the Institution of Mechanical Engineers, Part G: Journal of Aerospace Engineering*, vol. 233, no. 3, pp. 1159–1168, Mar. 2019, ISSN: 0954-4100, 2041-3025. DOI: 10.1177/0954410017745899. [Online]. Available: http://journals.sagepub.com/doi/10.1177/0954410017745899 (visited on 08/11/2022).

[57] K. H. Hohenemser and S.-K. Yin, "Some applications of the method of multiblade coordinates," *Journal of the American Helicopter Society*, vol. 17, no. 3, pp. 3–12, 1972.

[58] R. van Aalst and M. D. Pavel, "On the question of adequate modelling of steady-state rotor disc-tilt for helicopter manoeuvring flight," *European Journal of Operational Research*, pp. 1–8, 2002.

[59] W. Johnson, *Helicopter theory, 1980*.

[60] J.-P. Reddinger and F. Gandhi, "Physics-based trim optimization of an articulated slowed-rotor compound helicopter in high-speed flight," *Journal of Aircraft*, vol. 52, no. 6, pp. 1756–1766, Nov. 2015, ISSN: 0021-8669, 1533-3868. DOI: 10.2514/1.C032939. [Online]. Available: https://arc.aiaa.org/doi/10.2514/1.C032939 (visited on 07/06/2022).

[61] M. W. Oppenheimer, D. B. Doman, and M. A. Bolender, "Control allocation for over-actuated systems," in *2006 14th Mediterranean Conference on Control and Automation*, Ancona, Italy: IEEE, Jun. 2006, pp. 1–6, ISBN: 978-0-9786720-1-0 978-0-9786720-0-3. DOI: 10.1109/MED.2006.328750. [Online]. Available: http://ieeexplore.ieee.org/document/4124855/ (visited on 08/07/2022).

[62] K. A. Bordignon, *Constrained control allocation for systems with redundant control effectors*. Virginia Polytechnic Institute and State University, 1996.

[63] W. Durham, K. A. Bordignon, and R. Beck, *Aircraft control allocation*. John Wiley & Sons, 2017.

[64] L. Lefevre, J. Delva, and V. Nowinski, "Experimental evaluation of the aerodynamic rotor/propeller interactions in hybrid compound helicopters," p. 10, 2021.

[65] L. Lefevre, V. Nowinski, J. Delva, and A. Dazin, "Experimental velocity fields evaluation under the rotor/propeller interactions for high speed helicopters for different propeller positions," In Review, preprint, Jun. 22, 2022. DOI: 10.21203/rs.3.rs-1753067/v1. [Online]. Available: https://www.researchsquare.com/article/rs-1753067/v1 (visited on 03/21/2023).

[66] S. Sieberling, "Design of a robust generic flight control system using incremental nonlinear dynamic inversion," *Unpublished M. Sc. Thesis, Faculty of Aerospace Engineering, In Delft: Delft University of Technology*, 2009.

[67] K. M. dos Santos, A. L. da Silva, and F. d. S. N. Coelho, "Cobem-2017-2752 attitude determination for a brazilian cubesat mission using the kalman filter,"